Scanning Electron Microscopy

Reference Studies

Contents

23-Feb-18

A comparative SEM study on the micromorphology of glacial and nonglacial clasts with varying age and lithology

John G. Van Hoesen and Richard L. Orndorff

Abstract: Preliminary research on striated clasts from a variety of depositional environments suggests that scanning electron microscopy (SEM) of striated clasts of varying lithology in diamictons may prove useful in interpreting a glacial origin. Evaluating whether SEM analysis of clasts from diamictons is an applicable technique to define a glacial origin requires a better understanding of the microfeatures occurring on glacial and nonglacial clasts. We describe microtextures and surface characteristics for samples of quartzite, granite, limestone, basalt, chert, pillow basalt, and quartz pebbles collected from a variety of depositional environments. Our study suggests that it is possible to differentiate between glacial and nonglacial deposits based on frequency and morphology of diagnostic surface microfeatures observed on entrained clasts. These microfeatures are best preserved and identified on competent and monomineralic samples (e.g., quartzite, chert, limestone) and poorly preserved on less resistant and polymineralic samples (e.g., basalt and granite).

Résumé : Une recherche préliminaire sur des clastes striés provenant de divers environnements de déposition démontre que la microscopie électronique à balayage (MEB) de clastes striés provenant de diverses lithologies de diamictons peut être utile pour interpréter une origine glaciaire. L'évaluation de l'analyse par MEB de clastes provenant de diamictons, afin de savoir si cette technique est applicable pour définir une origine glaciaire, exige une meilleure compréhension des micro-caractéristiques qui se trouvent sur les clastes glaciaires et non glaciaires. Nous décrivons les micro-textures et les caractéristiques de surface d'échantillons de quartzite, de granite, de calcaire, de basalte, de chert, de laves à coussinets et de cailloux prélevés dans divers environnements sédimentaires. Selon notre étude, il est possible de différencier les dépôts glaciaires et non glaciaires d'après la fréquence et la morphologie des micro-caractéristiques diagnostiques observées à la surface de clastes entraînés. Ces micro-caractéristiques sont les mieux préservées et identifiées sur des échantillons compétents et monominéraliques (p. ex. quartzite, chert, calcaire) et moins bien préservées sur les échantillons moins résistants et polyminéraliques (p. ex. basalte et granite).

[Traduit par la Rédaction]

Introduction

There are limited data published on the analysis of microfeatures and characteristics of striated clasts thought to have a glacial origin (Agassiz 1840; Wentworth 1928; Judson and Barks 1961; Bjørlykke 1974; Hicock and Dreimanis 1989; Helland and Diffendal 1993). The majority of previous research concerning microtextures associated with tills has primarily focused on individual quartz grains (Brown 1973; Krinsley and Doornkamp 1973; Folk 1975; Mahaney et al. 1988, 1991, 1996, 2004; Mazzullo and Ritter 1991; Campbell and Thompson 1991; Mahaney and Kalm 1995, 2000; Mahaney 1995; 2002; Strand et al. 2003). Surface textures of quartz grains have been used to determine local ice transport vectors (albeit problematic), ice thickness, and depositional environment. Scanning electron microscopy (SEM) results from these studies have established that sediment affected by glacial transport and deposition exhibits distinct microtextural characteristics (Table 1). However, we suggest these characteristics are not isolated to glacially derived quartz grains. While previous research has established the merits of SEM analysis of quartz grains in glacial research, our study suggests that SEM analysis of larger clasts (pebbles and cobbles) in diamictons may also prove useful in defining a glacial origin. We hypothesize that although we are investigating clasts larger and commonly softer than quartz grains, these clasts will exhibit some of the features listed in Table 1 if the deposits from which they were collected have a glacial origin.

The thesis of this project is that it is possible to identify and relate specific microtextures that have been observed on quartz grains, with similar microtextures on larger clasts. We evaluate this hypothesis by documenting various microscale textures and surface features exhibited by clasts of differing lithologies from glacial environments and comparing and contrasting these observed textures with features identified

Received 10 December 2003. Accepted 24 June 2004. Published on the NRC Research Press Web site at http://cjes.nrc.ca on 27 September 2004.

Paper handled by Associated Editor R. Gilbert.

J.G. Van Hoesen.[1] Green Mountain College, Department of Environmental Studies, One College Circle, Poultney, VT 05764, USA.
R.L. Orndorff. Eastern Washington University, Department of Geology, Cheney, WA 99004, USA.

[1] Corresponding author (e-mail: vanhoesenj@greenmtn.edu).

Can. J. Earth Sci. **41**: 1123–1139 (2004) doi: 10.1139/E04-056

Table 1. Summary of previously described surface textures and features identified on quartz grains and bedrock using a scanning electron microscope.

Feature	References
Adhering particles	Helland et al. 1997; Mahaney et al. 1986, 1991, 1996, 2001; Mahaney and Kalm 2000; Mahaney 1995; Mazzullo and Ritter 1991; Smalley 1966; Watts 1985
Abrasion features	Helland et al. 1997; Mahaney 2002; Mahaney et al. 1996, 2001; Mahaney and Kalm 2000; Mahaney 1995; Mazzullo and Ritter 1991; Strand et al. 2003
Arc-shaped steps	Campbell and Thompson 1991; Helland and Diffendal 1993; Helland et al. 1997; Mahaney et al. 1996, 2001; Mahaney and Kalm 2000; Mahaney 1995; Strand et al. 1993
Breakage blocks	Campbell and Thompson 1991; Helland and Diffendal 1993; Helland et al. 1997
Chattermarks	Campbell and Thompson 1991; Folk 1975; Mahaney et al. 2004
Conchoidal fractures	Abd-Alla 1991;Campbell and Thompson 1991; Helland and Diffendal 1993; Helland et al. 1997; Krinsley and Marshall 1987; Mahaney et al. 1988*a*, 1988*b*, 1991, 1996, 2001; Mahaney and Kalm 2000; Mahaney 1995; Mazzullo and Ritter 1991; Strand et al. 2003
Curved grooves	Campbell and Thompson 1991; Helland and Diffendal 1993; Helland et al. 1997; Mahaney et al. 1988*a*, 1988*b*, 1996, 2001, 2004; Mahaney 1995, 1990*b*
Cresentic gouges	Campbell and Thompson 1991; Mahaney et al. 1988*a*, 1988*b*, 1996, 2004; Mahaney 1995; Watts 1985
Crushing features	Mahaney 1990*a*, 1990*b*; Mahaney et al. 1988*a*, 1988*b*
Deep troughs	Mahaney et al. 1996, 2001; Mahaney and Kalm 2000
Dissolution etching	Campbell and Thompson 1991; Mahaney et al. 1988*a*, 1988*b*, 1991, 1996, 2001; Mahaney and Kalm 2000; Mahaney 1995
Edge rounding	Campbell and Thompson 1991; Mahaney et al. 2001; Mahaney and Kalm 2000; Mahaney et al. 1996, 1991, 1988*a*, 1988*b*
Fracture faces	Mahaney et al. 1996, 2001; Mahaney and Kalm 2000
High relief	Campbell and Thompson 1991; Helland et al. 1997; Mahaney et al. 1988*a*, 1988*b*, 1991, 1996, 2001; Mahaney and Kalm 2000; Mahaney 1990, 1995
Lattice shattering	Mahaney et al. 1996, 2001; Mahaney and Kalm 2000; Mahaney 1995
Linear steps	Mahaney et al. 1996, 2001; Mahaney and Kalm 2000
Low relief	Campbell and Thompson 1991; Helland et al. 1997; Mahaney et al. 1991, 1996, 2001; Mahaney and Kalm 2000; Mahaney 1995
Mechanically upturned plates	Abd-Alla 1991; Campbell and Thompson 1991; Helland and Diffendal 1993; Helland et al. 1997; Mahaney et al.1996, 2001; Mahaney and Kalm 2000; Mahaney 1995
Medium relief	Campbell and Thompson 1991; Helland et al. 1997; Mahaney et al. 1988*a*, 1988*b*, 1991, 1996, 2001; Mahaney and Kalm 2000; Mahaney 1995
Overprinted grains	Mahaney et al. 1991, 1996, 2001; Mahaney and Kalm 2000
Precipitation features	Campbell and Thompson 1991; Helland et al. 1997; Mahaney et al. 1988*a*, 1988*b*, 1991, 1996, 2001; Mahaney and Kalm 2000; Mahaney 1995; Mazzullo and Ritter 1991; Watts 1985
Preweathered surfaces	Mahaney et al. 1988*a*, 1988*b*, 1991, 1996, 2001; Mahaney and Kalm 2000; Mahaney 1995; Watts 1985
Sharp angular features	Mahaney et al. 1988*a*, 1988*b*, 1991, 1996, 2001; Mahaney and Kalm 2000; Mahaney 1995
Star-cracking	Campbell and Thompson 1991
Straight grooves	Campbell and Thompson 1991; Helland and Diffendal 1993; Helland et al. 1997; Mahaney et al. 1988, 1996, 2001, 2004; Mahaney and Kalm 2000; Mahaney 1995
Subparallel linear fractures	Mahaney et al. 1991, 1996, 2001, 2004; Mahaney and Kalm 2000; Mahaney 1990*b*, 1995
Subparallel crushing planes	Mahaney 1995; Mahaney et al. 1988*a*, 1988*b*,
V-shaped percussion cracks	Abd-Alla 1991;Campbell and Thompson 1991; Helland and Diffendal 1993; Helland et al. 1997; Mahaney et al.1991, 1996, 2001; Mahaney and Kalm 2000; Krinsley and Donahue 1968; Krinsley and Doornkamp 1973; Krinsley and Marshall 1987
Weathered surfaces	Mahaney et al. 1988*a*, 1988*b*, 1991, 1996, 2001; Mahaney and Kalm 2000; Mahaney 1995; Mahaney 1990*a*; Mazzullo and Ritter 1991; Watts 1985

on clasts from nonglacial environments. The ultimate goal of this study is to evaluate whether SEM analysis of striated clasts in diamictons is an applicable tool to infer a glacial origin.

Origin of microfeatures

Krinsley and Doornkamp (1973), Marshall (1987), and Mahaney (2002) provide a comprehensive summary of and definitions for various microfeatures resulting from glacial, eolian, fluvial, mass wasting, volcanic, and cosmic processes. Terminology used in this study is based on descriptions and terms established by previous authors investigating quartz grains (Table 1; Mahaney 2002), which we apply to larger pebble–cobble sized clasts. However, we identify a number of microfeatures that are not exclusive to glacial environments, and therefore wish to clarify the origin of the most diagnostic features we observed. A cursory understanding of how these features are formed will also be useful when identifying these features using SEM techniques.

Many of the clasts we analyzed exhibited features that can develop through fluvial, eolian, tectonic, and mass wasting processes. Fluvial environments experience continuous turbulent abrasion via grain-to-grain contact in aqueous suspension, where vibrational energy is transferred to grains during impact, producing characteristic fluvial microfeatures (Krinsley and Doornkamp 1973; Manker and Ponder 1978; Krinsley et al. 1979; Manickam and Barbaroux 1987; Krinsley and Marshall 1987; Mahaney 2002). These include V-shaped percussion features, radial fractures, edge rounding, and evidence of abrasion or scouring. Scouring is used to describe the process through which surfaces of clasts being transported are abraded by smaller sand-sized particles, oftentimes producing a smooth, polish-like surface. V-shaped percussion features and radial fractures develop in response to direct high-speed impacts that are chaotic in nature, while edge rounding and abrasion fatigue result from less chaotic and low-velocity collisions (Pascoe 1961; Krinsley and Doornkamp 1973; Margolis and Krinsley 1974; Marshall 1987; Mahaney 2002). V-shaped percussion marks are usually randomly oriented, however chemically derived, oriented V-shaped percussion marks are described by Campbell and Thompson (1991). Radial fractures are less commonly observed than V-shaped percussion features and are similar in appearance to star cracking (Campbell and Thompson 1991; Mahaney 2002). Clasts that have experienced abrasion fatigue are characterized by cracked, dislocated and broken surfaces (Pascoe 1961; Mahaney 2002).

Many clasts also exhibit microfeatures that develop through eolian processes. Sand grains transported by wind can experience high-velocity grain-to-grain and grain-to-surface impacts during saltation and creep (Bagnold 1941; Glennie 1970; Mahaney and Andes 1996). These collisions produce linear and conchoidal fractures, parallel ridges, elongate depressions, rolling topography, polygonal cracks, mechanically upturned plates, V-shaped percussion features, and abrasion fatigue (Pascoe 1961; Abd-Alla 1991; Mahaney 2002). However, V-shaped percussion features described by Abd-Alla (1991) and linear and conchoidal fractures described by Mahaney and Andes (1996) are smaller and less deeply entrenched than those resulting from stream transport and lack evidence for a preferred orientation.

Mahaney (2002) describes microfeatures produced under mass wasting conditions. These features include en echelon fractures, straight and curved deep grooves, and a lack of abrasion features. Straight grooves can also develop under high-stress neotectonic conditions (Mahaney 2002).

Although many microfeatures we observed can develop under varying environmental conditions, there are a number of features that are diagnostic of glacial transport. Quartz grains — and therefore, we suggest, larger clasts — entombed in glacial ice develop microfeatures in response to vibrational energy released during stick-slip processes and basal sliding and abrasion (Atkins et al. 2002; Benn and Evans 1998; Cuffey et al. 1999; Echelmeyer and Wang 1987; Mahaney 2002). The critical shear stress, dependent on lithology and grain size, must be surpassed prior to the release of this vibrational energy (Boulton and Hindmarsh 1987; Clarke 1987; Alley 1989; Kamb 1991). Microfeatures also develop during grain-to-grain, and therefore grain-to-clast and clast-to-clast, interactions in the subglacial environment (Barcilon and MacAyeal 1993; Benn and Evans 1998; Mahaney 1995, 2002). These diagnostic microfeature include (1) directional curved troughs or grooves in multiple pairs, (2) cresentic gouges, (3) conchoidal and linear crushing features, (4) arc-shaped steps, and (5) conchoidal fractures (Mahaney 1995, 2002; Mahaney and Kalm 2000; Mahaney et al. 1996, 2001). It is important to clarify the distinction between troughs, which are deeply embedded features exceeding a depth of 5 μm or more, and grooves, which are weakly embedded features (Mahaney 2002). Many features indicative of a glacial environment develop under direct abrasion and grinding (crushing features, grooves, and troughs), while others develop in response to vibrational energy caused by stick-slip motion (Barcilon and MacAyeal 1993; Mahaney 2002).

It should be clear that not all microfeatures described in this study are used to indicate a glacial origin, nor do we attempt to evaluate the origin of individual clasts. Many of the features we describe could have developed under preexisting conditions or through processes prior to glacial transport. For example, the presence of deep grooves is not diagnostic of a glacial origin, but could indicate mass wasting or neotectonic activity prior to incorporation into a glacial system (Mahaney 2002). Similarly, arc-shaped steps, conchoidal fractures, and parallel steps can develop under non-glacial conditions (Higgs 1969; Culver et al. 1983; Mahaney and Sjöberg 1993). Thus, we present a comparison of microfeatures observed on large-scale pebbles and cobbles with microfeatures described in previous studies on smaller scale quartz grains. However, we do attempt to discriminate between microfeatures that are unequivocally glacial in origin and microfeatures derived from fluvial and glaciofluvial processes.

Methods

More than 50 striated samples, ranging in size from 5.0 cm to 0.75 m, were collected from known glacial, eolian, fluvial, and lacustrine environments throughout the southwestern United States and Canada during 2000 to 2002 (Figs. 1–2). Till samples from Allan Hills, Antarctica were provided by Phil Holme. Of these 50 samples, 36 were analyzed using the SEM. Two clasts from each sampling location were chosen for analysis, one that displayed visible surface striations or markings, and a second that lacked visible surface features. A more descriptive summary of the sampling sites, lithology, relative age and characteristic environments is provided in Table 2.

This study focused on the southwest and high-latitude regions because we reason that preservation of surface features will increase with decreased physical and chemical weathering typical of these regions. We analyzed clasts that appeared to have been most strongly affected during transport and clasts that lacked evidence of surface abrasion so we could evaluate whether these microfeatures were preserved independent of the presence of macrofeatures. We wanted to ensure that we analyzed samples that we knew were affected

Fig. 1. Location of study sites in the Yukon, Antarctica, and the southwestern United States.

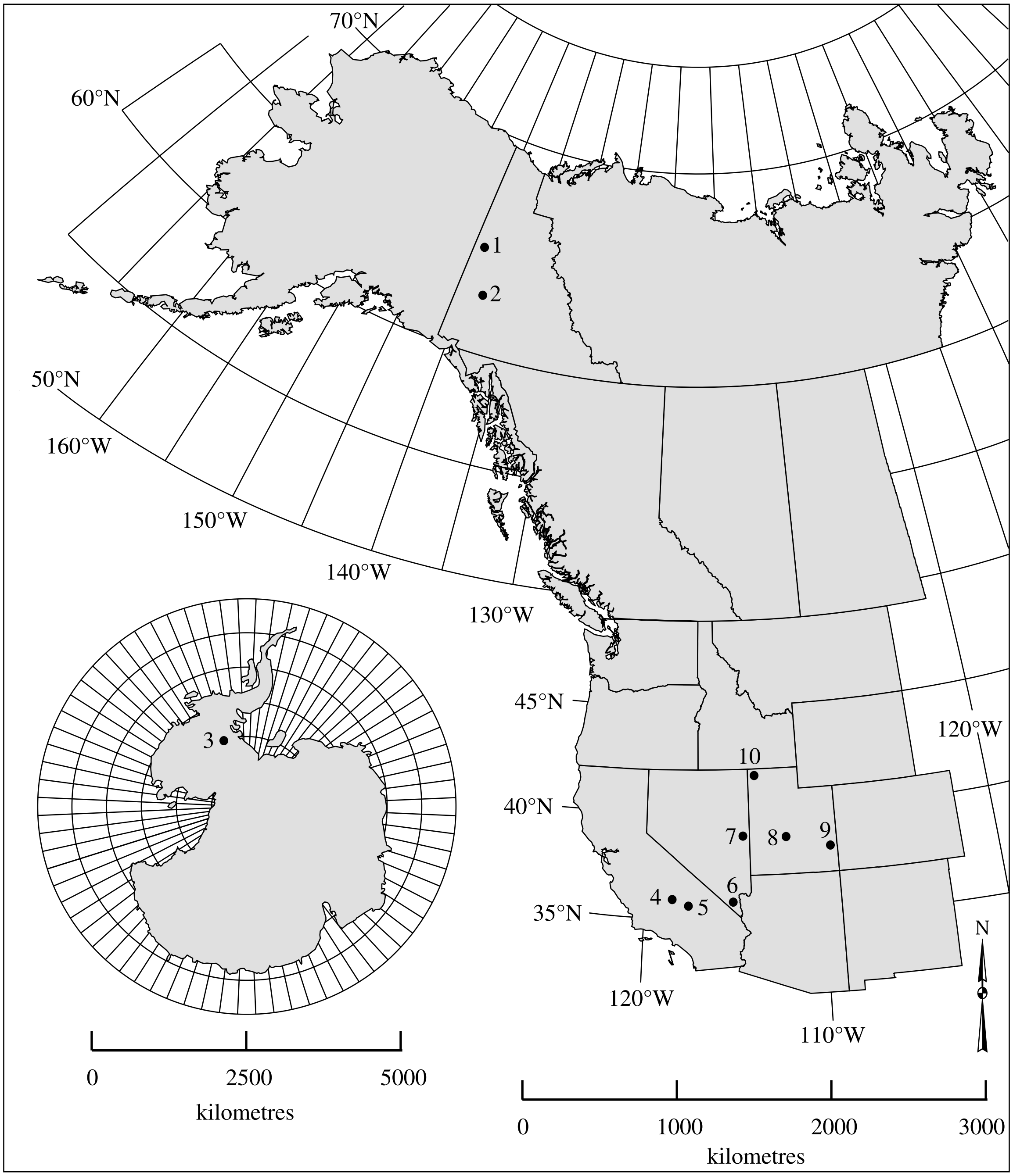

1. Klondike Gravel, Yukon
2. Yukon River, Yukon
3. Allan Hills, Antarctica
4. Yosemite National Park, CA
5. Devils Postpile National Monument, CA
6. Spring Moutains, NV
7. Snake Range, NV
8. Fish Lake Plateau, UT
9. La Sal Mountains, UT
10. Lake Bonneville Shoreline, UT

by glaciation as well as those affected by other processes to compare and contrast observed microfeatures with those found on quartz grains from glacial and nonglacial environments. More samples were collected in glacial environments because one of the goals of this study was to characterize microfeatures specific to glaciation. Samples collected from other environments are included for comparison, not as a comprehensive analysis of features developed in eolian, fluvial, or lacustrine settings.

Laboratory analysis involved selecting 16 glacial samples and eight nonglacial samples, from an overall sample population of > 50 clasts, cutting these 24 samples into small (0.5–1.5 cm) billets with a rock saw and cleaning them with petroleum ether to remove oils and impurities. The samples were mounted on glass plates using charcoal tape and sputtered with a gold coating for 60 s using a Cressington 108auto sputter coater. Finally, texture and surface features of each sample were identified and documented using a JEOL 5600 SEM.

Results

Previous studies have focused on SEM analysis of quartz grains from known glacial deposits or active glacial environments (Table 1; Mahaney 2002). These studies document and describe distinctive microscale features that are characteristic of glacial environments. The samples in this study exhibit many of these glacially derived features depending on lithology, age, and source of the clast. Of particular interest is the presence of arc-shaped and linear steps, and conchoidal and subparallel crushing features assumed to develop through stick-slip processes, and compression and grinding during glacial transport (Barcilon and MacAyeal 1993; Mahaney 1995). Specific SEM-observed microfeatures for each lithology and depositional environment are summarized in Table 3.

Spring Mountains

The Spring Mountains are located in southern Nevada and border the western margin of the Las Vegas Valley. The Big Falls till (informal name) is situated at ~2590 m above sea level (masl; Fig. 2*a*). This solitary glacial deposit contains numerous striated limestone clasts ranging in size from 0.5 cm to 0.75 m likely derived from the Bonanza King and Bird Spring formations (Burchfiel 1974; Van Hoesen and Orndorff 2000, 2003; Orndorff and Van Hoesen, 2003). The age of this deposit is probably correlative to Mono Basin age deposits in the Sierra Nevada based on clast preservation and post-depositional modification of the landform (Russell 1884; Sharp and Birman 1963; Yount and LaPointe 1997). However, the lack of suitable organic material for radiocarbon analysis precludes accurate age determination.

Approximately 30 limestone clasts were collected from the till and four limestone clasts were collected from a fluvial deposit upvalley from the till during the summer of 2000.

Limestone clasts from the till display both macroscale features and microscale features characteristic of a glacial origin. Most clast surfaces are strongly polished and contain striations (1.0–4.0 mm wide), chattermarks (3.0–5.0 mm), crescentic gouges (1.0–3.0 cm), and rare small-scale flute topography (1.0–3.0 cm amplitude) that are all visible to the unaided eye. Chattermarks most commonly occur individually on the surface of the clast, but are observed within the striations, and commonly occur in small lenses of micrite within the limestone. Scanning electron microscopy of 14 striated limestone clasts (with *c*-axes that varied from about 10 to 30 cm) reveals distinctive microscale features attributed to the effects of glaciation, including straight grooves (Fig. 3*a*), crescentic gouges, arc-shaped steps, curved grooves, conchoidal and subparallel crushing features, and linear steps. Straight grooves range in width from 2.0 to 10 μm, crescentic gouges range in size from 75 to 100 μm wide with variable length, arc-shaped steps are 20–100 μm wide, and crushing features are 5.0–20 μm wide. None of the samples exhibit scouring features or V-shaped percussion features, and very few contain features that appear to have been rounded since formation. However, many show evidence of dissolution etching, and some have weathered surfaces.

In contrast, limestone clasts sampled from fluvial deposits exhibit rounding, visible abrasion (scouring), and lack striations with a preferred orientation. SEM analyses indicate the presence of well-developed V-shaped percussion features that are ~100–175 μm wide at their apex, prominent scouring features, and edge rounding (Fig. 6).

Devils Postpile

Devils Postpile National Monument is located in southern California east of Yosemite National Park and southwest of Mammoth Lakes. This lava flow is composed of Pliocene columnar trachybasalt–trachyandesite whose upper surface was well polished during the last glaciation (Fig. 2*e*; Bailey 1987; Bailey and Hill 1987). Four samples of basalt were collected from the polished upper surface of the flow during the summer of 2001.

The upper surface of the Devils Postpile basalt flow is striated as well as polished. Striations ranging in width from ~1 to 3 mm and crescentic gouges (~1–1.5 cm wide) are visible with the unaided eye. Under SEM magnification, these samples exhibit subparallel linear fractures, straight grooves that are 1–2 μm wide, linear steps that are 25–75 μm wide, deep troughs that are 5–15 μm wide, conchoidal crushing features that are 10–90 μm wide, and arc-shaped steps ~50–100 μm wide (Figs. 3*g*–3*h*). The glacial polish that is so obvious in the field is easily identified in the SEM as relict polish, although this surface does exhibit evidence of dissolution etching.

Fish Lake

The Fish Lake Plateau is located southeast of Salt Lake City, Utah. The plateau is composed of Tertiary volcanics, primarily red to purple trachyte and light gray sanidine trachyte (Hardy and Muessig 1952). Tertiary sedimentary rocks underlie the volcanic successions and these in turn are thought to overly the Green River formation (Hardy and Muessig 1952). Two episodes of glaciation are described as Wisconsin I and Wisconsin II but more than likely represent Tioga–Tahoe and (or) Angel Lake – Lamoille glacial stages. Samples were collected from a younger Wisconsin II terminal moraine at the mouth of Pelican Canyon and an older Wisconsin I terminal moraine north of Pelican (Widgeon) Bay.

Two ages of sanidine trachyte were collected from the Fish Lake region representing the older Early Pleistocene and younger Late Pleistocene glacial advances. The surface of the older sample is more strongly weathered and lacks visible striations, while the younger sample is moderately weathered but retains visible striations ranging in width from 1 to 4 mm (Fig. 4). Viewed with the SEM, the older sample exhibits arcuate grooves that range in size from 75 to 125 μm wide, arc-shaped steps ranging from 50 to 80 μm wide, and conchoidal crushing features. Relict polish occurs as preweathered surfaces that are weathered and eroded. Arcuate grooves and arc-shaped steps are weakly preserved in some instances but are difficult to recognize. The younger sample exhibits arcuate grooves that range in size from 50 to

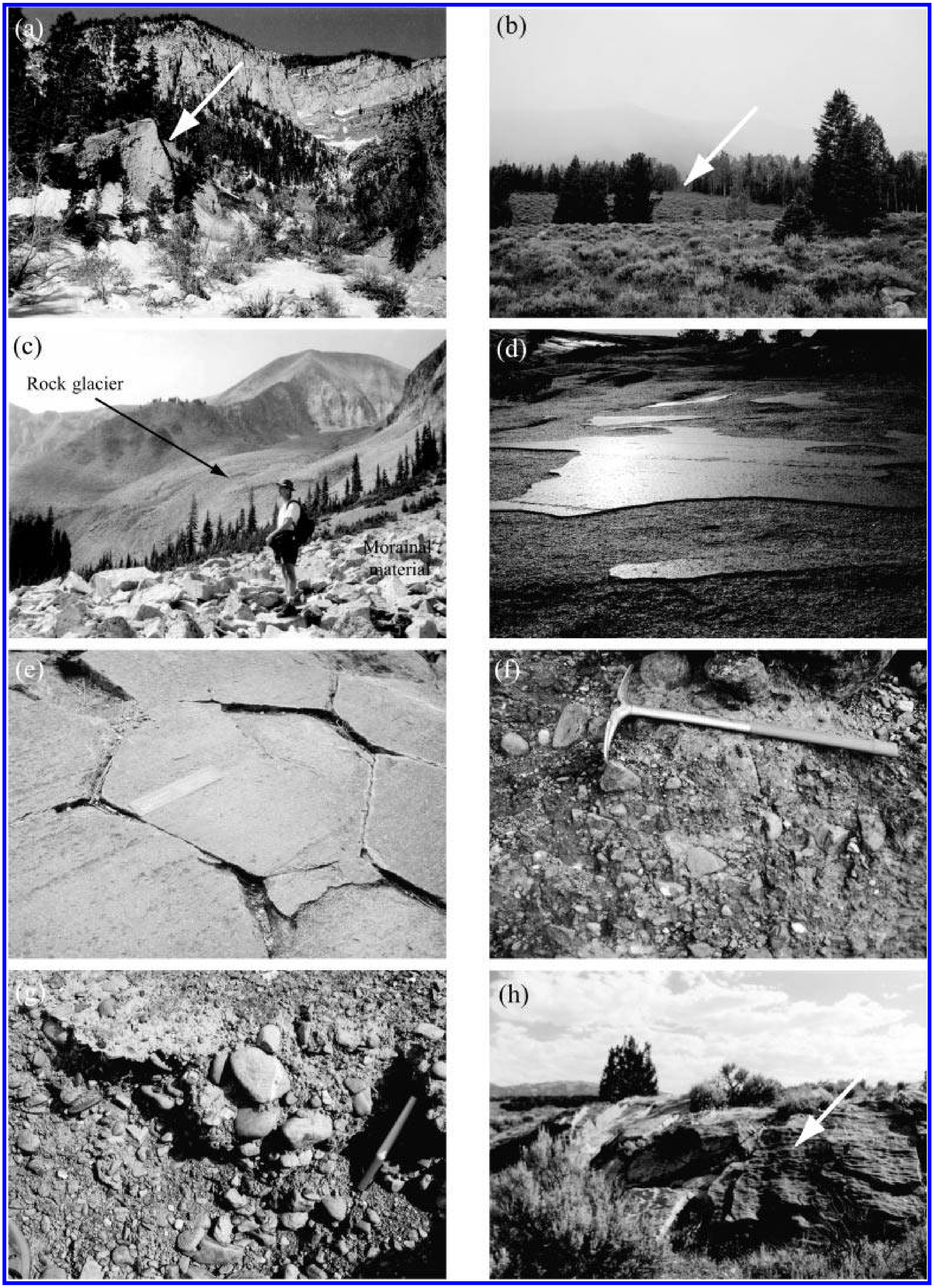
(a)
(b)
(c)
Rock glacier
Morainal material
(d)
(e)
(f)
(g)
(h)

Fig. 2. Field photos illustrating typical environment of selected samples. (*a*) Big Falls Till in the Spring Mountains, NV, (*b*) Lamoille (Tahoe) age moraine in Southern Snake Range, (*c*) view of rock glacier on Mt Tukuhnikivatz from a lateral moraine, (*d*) polished surface of granite in Yosemite National Park, (*e*) Upper surface of polished basalt columns in Devils Postpile National Monument, (*f*) moderately consolidated diamicton along Yukon River, (*g*) upper surface of Klondike Gravel southwest of Dawson City, Yukon Territory, and (*h*) wave polished quartzite shoreline in northwest Utah.

Table 2. Summary of sample sites and their characteristics (sample ID designation, geographic coordinates, lithology, relative age, and depositional environment).

Name	Latitude	Longitude	Lithology	Relative age	Environment
Glacial	37°50′39.7″	119°27′31.3″	Granite	MP	Bedrock
Yosemite NP, CA	37°37′32.6″	119°05′02.3″	Basalt	MP	Bedrock
Devils Postpile NM, CA	64°01′37.7″	139°21′45.2″	Chert	~1.5 Ma	Till
Fort Selkirk, YT	36°16′13.6″	115°40′25.6″	Limestone	EP	Till
Spring Mountain's, NV	38°15′53.8″	114°15′51.8″	Quartzite	EP	Moraine crest
Snake Creek, NV	62°48″	137°20″	Quartz	LP	Till
Allan Hills, Antarctica	62°48″	137°20″	Pillow basalt	LP	Till
Fish Lake, UT	38°35′27.4″	111°40′33.9″	Trachyte	EP	Moraine crest
Fish Lake, UT	38°34′15.5″	111°41′55.5″	Trachyte	LP	Moraine crest
La Sal Mountains, UT	38°26′55.1″	109°15′26.9″	Trachyte	LP	Rock glacier lobe
Non-glacial					
Bonneville Shoreline, UT	41°36′34″	113°37′02″	Quartzite	MP	Wave cut shoreline
Klondike Gravel, YT	64°01′37.7″	139°21′45.2″	Chert	LP	Glacial outwash
North Fork Baker Creek, NV	38°43′05″	114°23′31″	Quartzite	H	Fluvial
Spring Mountain's, NV	36°27′20″	115°67′04″	Limestone	H	Fluvial

Note: EP, Early Pleistocene; MP, Middle Pleistocene; LP, Late Pleistocene; H, Holocene. NP, National Park; Ca, California; NM, New Mexico; NV, Nevada; UT, Utah; YT, Yukon Territory.

100 μm wide, arc-shaped steps ranging from 30 to 70 μm wide, subparallel crushing planes that are 10–20 μm wide, fracture faces, relict polish, and crushing features (Fig. 4).

Snake Range

The Snake Range is located in east-central Nevada within the boundaries of the Basin and Range physiographic province. It has long been recognized that the Snake Range was glaciated during the late Quaternary (Gilbert 1875; Russell 1884; Heald 1956; Kramer 1962; Whitebread 1969; Osborn 1990; Piegat 1980; Osborn and Bevis 2001). Two discrete intervals of glaciation in the Snake Range are correlative with Lamoille and Angel Lake advances (Sharp 1938; Wayne 1984; Osborn and Bevis 2001). The Angel Lake advance is approximately correlative with the Tioga stage, and the Lamoille advance with the Tahoe stage, as described in the Sierra Nevada. Glaciated portions of the Snake Range are primarily early Paleozoic Prospect Mountain Quartzite, Pioche Shale, and Pole Canyon Limestone intruded by the Jurassic-age Snake Creek – Williams Canyon Pluton (Drewes 1958; Whitebread 1969; Lee et al. 1970, 1986; Lee and Van Loenen 1971; Lee and Christiansen 1983*a*, 1983*b*; Lee 1968; McGrew and Miller 1995; Miller et al. 1999). Two clasts of Prospect Mountain Quartzite were collected from the crest of a dissected Lamoille moraine (Fig. 2*b*) in Snake Creek at ~2587 masl and two quartzite clasts were collected from Holocene fluvial deposits in North Fork Baker Creek at ~3038 masl during the summer of 2001.

The quartzite samples collected from Snake Creek exhibit well-preserved striations ~2–4 mm wide visible with the unaided eye. Under magnification, these samples contain numerous well-preserved features, including subparallel crushing features that are 10–20 μm wide, conchoidal fractures 2–5 μm wide, subparallel linear fractures, straight grooves that are 5–10 μm wide, linear steps that are 5–30 μm wide, fracture faces, curved grooves that are 20–30 μm wide, arc-shaped steps that are 10–20 wide, chattermarks, and star cracking (Fig. 4). In contrast, the quartzite samples collected from North Fork Baker Creek are sub-rounded to rounded and are heavily scoured. Viewed under SEM, they exhibit well-developed V-shaped percussion features that are ~150–180 μm wide at their apex, moderately developed scouring features, and minor edge rounding.

La Sal Mountains

The La Sal Mountains are located in east-central Utah ~35 km east of Moab, Utah. Evidence for Pleistocene glaciation includes characteristic U-shaped valleys, moraines, and striated and polished bedrock (Richmond 1962; Nicholas 1994). There is also evidence of Holocene glaciation in at least one locality in the range (Nicholas 1991; Nicholas and Butler 1996). The range is composed of Late Cretaceous to early Tertiary hypabyssal intrusions of trachyte and ryholite porphyries overlain by a thick Quaternary mantle (Hunt 1958; Richmond 1962; Ross 1998). Two samples were collected from a Late Pleistocene moraine dissected by Brumley Creek, a tributary to Pack Creek, on the southwest flank of Mount Tukuhnikivatz (3805 masl; Fig. 2*c*).

Trachyte clasts collected from the surface of the moraine exhibit well-developed striations. These samples display

Table 3. Summary of microfeatures observed on collected striated samples from various depositional environments and lithologies.

	Adhering particles	Abrasion features	Arc shaped steps	Breakage blocks	Chattermarks	Conchoidal fractures	Curved grooves	Crushing features	Deep troughs	Dissolution etching	Edge rounding	Fracture faces	High relief	Lattice shattering	Linear steps	Low relief	Mechanically upturned plates	Medium relief	Overprinted grains	Precipitation features	Preweathered surfaces	Relict polish	Scouring features	Sharp angular features	Star cracking	Straight grooves	Subparallel linear fractures	Subparallel crushing planes	V-shaped percussion features	Weathered surfaces
Alan Hills, Antarctica	X	X	X		X		X									X													X	X
Alan Hills, Antarctica	X	X								X	X		X																X	X
Devils Postpile, California		X	X				X	X	X						X	X						X				X	X			X
Fish Lake, Utah (old)	X	X	X				X	X		X						X	X			X	X	X								X
Fish Lake, Utah (young)		X	X		X	X		X										X			X			X			X	X		X
Lake Bonnevile, Utah	X	X	X								X					X						X	X						X	X
Baker Creek, Nevada		X		X							X					X							X						X	X
Snake Creek, Nevada	X	X	X		X	X	X	X				X	X	X	X									X	X		X	X		X
Spring Mtns, Nevada (g)	X	X	X		X	X	X	X	X	X	X	X		X	X			X			X	X	X			X	X	X		X
Spring Mtns, Nevada (f)	X	X																			X								X	X
Mt Tukuhnikivatz, Utah	X	X	X				X	X		X	X						X	X			X	X								X
Klondike Gravel, Yukon	X	X	X													X					X								X	X
Yukon River, Yukon	X	X	X					X	X	X								X			X					X			X	X
Yosemitie NP, California	X	X	X				X	X	X	X		X	X								X	X		X		X	X			X

Note: Nevada (g), sampled from a till; Nevada (f), sampled from a fluvial deposit.

crushing features 15–30 µm wide, curved grooves that are 10–20 µm wide, and arc-shaped steps that are 15–40 µm wide (Fig. 5). They also show evidence of mechanically upturned plates, dissolution etching, and relict polish preserved as preweathered surfaces.

Allan Hills

In the Allan Hills region, extensive peperites, hyaloclastites, and irregular intrusive masses are intermixed with tuffs and tuff-breccias of the Mawson Formation (Ballance and Watters 1971). These rocks and correlatives, 1500 km along strike in the Transantarctic Mountains, form regional pyroclastic deposits transitional between Beacon Supergroup terrestrial sedimentation and Ferrar Supergroup flood basalt volcanism (Ballance et al. 1971; Denton and Hughes 2002; Atkins et al. 2002). The Sirius Group most likely developed during the Oligocene to Miocene, although the age of this deposit has been controversial (Bruno et al. 1997; Stroeven and Klehman 1999; Holme 2001; Denton and Hughes 2002).

Two lithologies were identified in the Allan Hills till sample. Five quartz pebbles ranging in size from 1 to 3 cm and two pebbles of pillow basalt ranging in size from 0.5 to 1.0 cm were analyzed. The quartz pebbles are well rounded and finely polished, and the pillow basalt is sub-rounded and heavily weathered. The quartz pebbles exhibit a combination of glacial and nonglacial characteristics, including V-shaped percussion, scouring features, and arc-shaped steps. V-shaped percussion and scouring features are the most common, but well-developed arc-shaped steps and rare lunate fractures are present (Fig. 5). The V-shaped percussion features range in size from 10 to 100 µm, arc-shaped steps range in size from 50 to 100 µm, and lunate fractures are 80–125 µm wide. The pillow basalt pebbles lack diagnostic microfeatures that could be used to identify an erosional origin. They are strongly weathered and exhibit high relief and abundant abrasion features.

Yosemite

Yosemite National Park is located in the west-central portion of the Sierra Nevada batholith. The eastern section of Yosemite Valley is composed of granites intruded by the Late Cretaceous Tuolumne Intrusive Suite (Bateman 1992; Ratajeski et al. 2001). The development and preservation of two ages of polished surfaces indicative of older and younger glacial advances in Yosemite Valley is discussed by Matthes (1930). Four samples were collected from strongly polished surfaces of Late Cretaceous granite on the southeast-facing slope of Polly Dome near Tenaya Lake during summer 2001 (Fig. 2*d*). This slope is located at an elevation of 2750 masl and covered with numerous erratics.

Samples are moderately weathered, have high mineral relief and exhibit small (0.5–1.0 mm) striations visible with the unaided eye. SEM analysis reveals the presence of 2–5 µm-wide subparallel linear crushing features, straight grooves that are 2–8 µm wide, curved grooves that are 50–150 µm wide, arc-shaped steps that are 30–60 µm wide, deep troughs that are 25–75 µm wide, breakage blocks, and fracture faces (Fig. 5). The polished surfaces visible in the field are well preserved at the micron scale as preweathered relict surfaces with little evidence of dissolution etching. These samples are characterized by high relief and sharp angular features with no evidence of V-shaped percussion cracks or scouring features.

Yukon Territory

A chert pebble was collected from a 1.5 Ma old diamicton along the Yukon River downstream from Fort Selkirk during summer 2001 (Fig. 2*f*; Jackson et al. 2001). During the

Fig. 3. SEM photomicrographs of representative glacial features from Spring Mountain and Devils Postpile samples. (*a*) Polished limestone surface showing numerous deep troughs (arrows) and arcuate grooves–striations (ag), (*b*) deep arcuate groove surrounded by surface with some evidence of dissolution etching, (*c*) lunate fracture containing conchoidal crushing features (ccf), (*d*) close-up of crushing features, (*e*) subparallel crushing features (*f*) crushing features (crf) and breakage blocks (bb), (*g*) relict polished surface on basalt, (*h*) close-up of polished basalt showing numerous arcuate grooves.

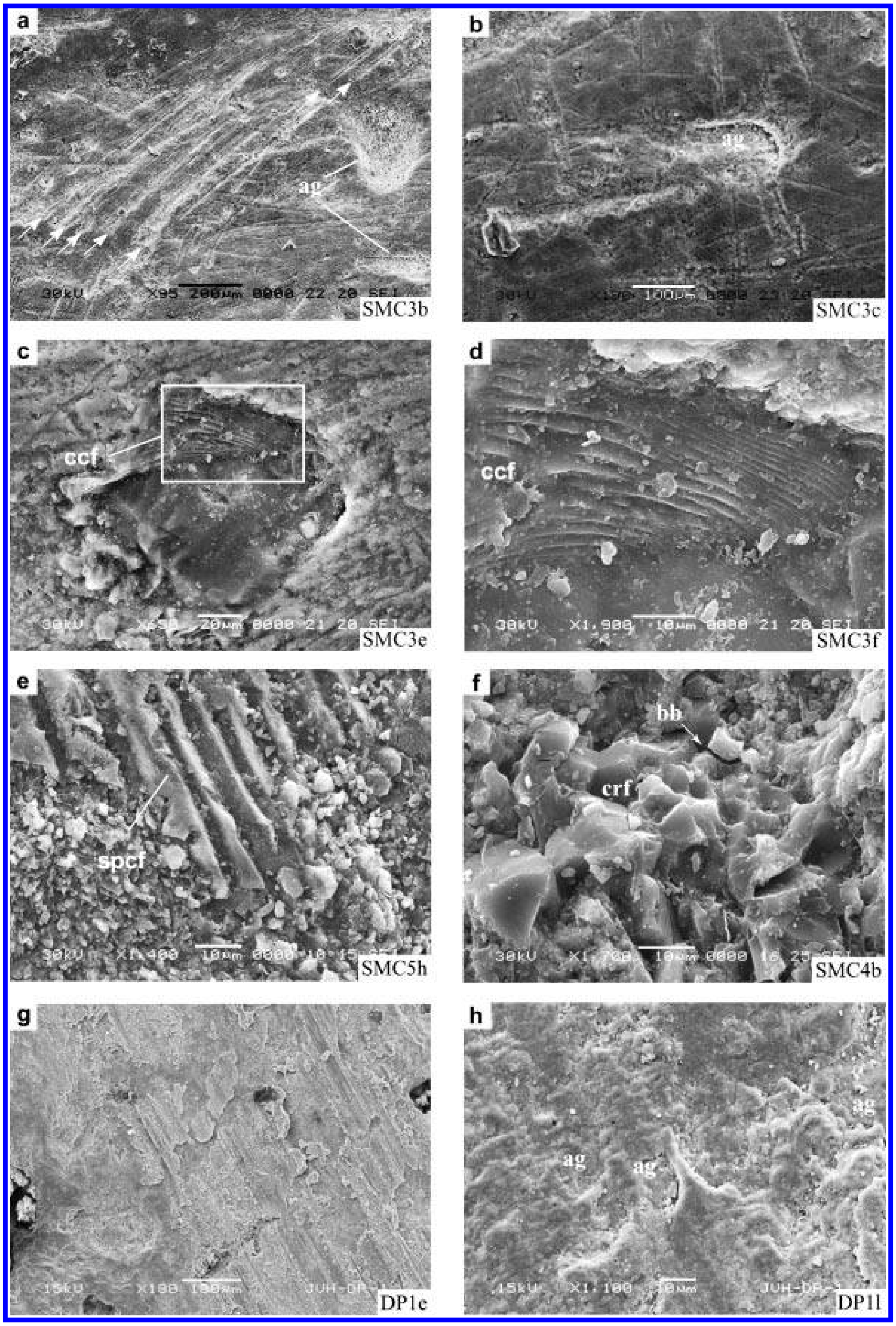

summer of 2002, six chert pebbles were collected from the upper unit of the Klondike Gravel–Conglomerate southwest of Dawson City (Fig. 2*g*) and two chert pebbles were collected from Pleistocene-age glaciofluvial gravel at the head of Dominion Creek (Froese et al. 2000, 2001; Froese 1997).

The chert sample collected along the Yukon River is well polished and well rounded and exhibits small (0.5–1 mm wide)

Fig. 4. SEM photomicrographs illustrating typical features and textures on Fish Lake (old and young) and Snake Creek samples. (*a*) relict polished surface (pws) with deep arcuate grooves, (*b*) close-up of deep arcuate groove containing crushing features (box in *a*), (*c*) quartz crystal showing fracture faces (ff) and subparallel crushing features (spcf), and (*d*) another quartz crystal exhibiting fracture faces, subparallel crushing features, and conchoidal crushing features (ccf), (*e*) subparallel conchoidal fractures, conchoidal fractures, and crushing features, (*f*) close-up of conchoidal fractures and crushing features (box in *e*), (*g*) conchoidal fractures and subparallel crushing features, and (*h*) fracture faces with subparallel conchoidal fractures and conchoidal crushing features.

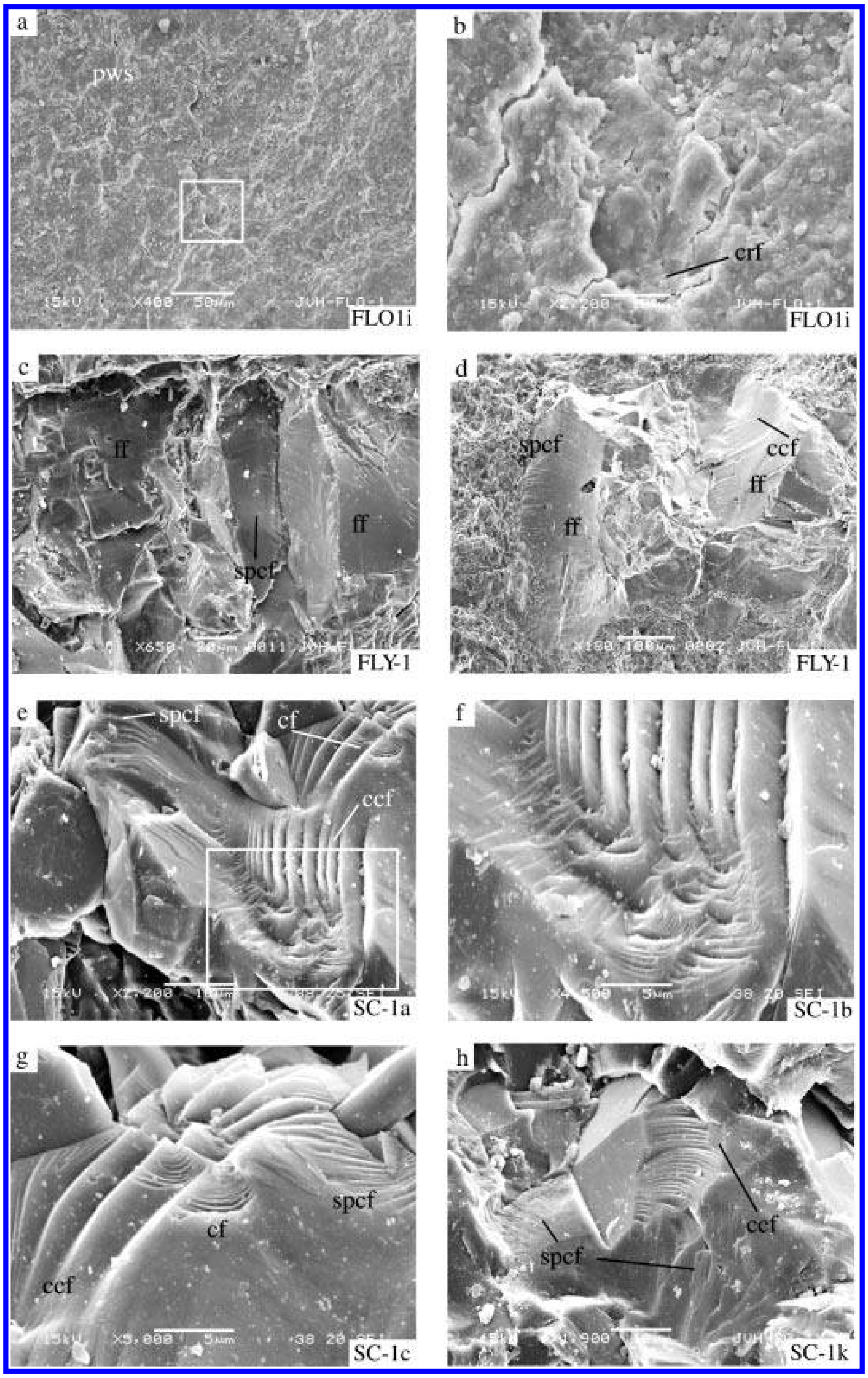

visible striations and chatter marks. SEM analysis of the clast shows the presence of straight grooves that are 5–15 µm wide, deep troughs that are 10–15 µm wide, arc-shaped steps that are 10–20 µm wide, rare V-shaped percussion features, evidence of dissolution etching, and some scouring features (Fig. 5).

Chert samples from the Klondike Gravel are well polished and round to sub-rounded. Small striations and abrasion

Fig. 5. SEM photomicrographs of representative glacial features on clasts from the La Sal Mountains, Antarctica, Yosemite, and Yukon River. (*a*) Comparison of surface morphology of weathered surface (ws) versus pre-weathered surface (pws), (*b*) close-up of pre-weathered surface exhibiting crushing features (crf), (*c*) close-up of lunate fracture (lf) surrounded by smaller V-shaped percussion features (arrows), (*d*) surface of Alan Hills pillow basalt showing no evidence of preserving microfeatures (vpf, V-shaped percussion feature; sc, scouring features), (*e*) quartz crystal exhibiting deep arcuate groove (ag) on a relict polished surface (pws), (*f*) close-up of arcuate groove and relict polish (box in *e*), (*g*) subparallel straight grooves (arrows), (*h*) subparallel linear grooves and arcuate lunate fracture or gouge (fine dashed line).

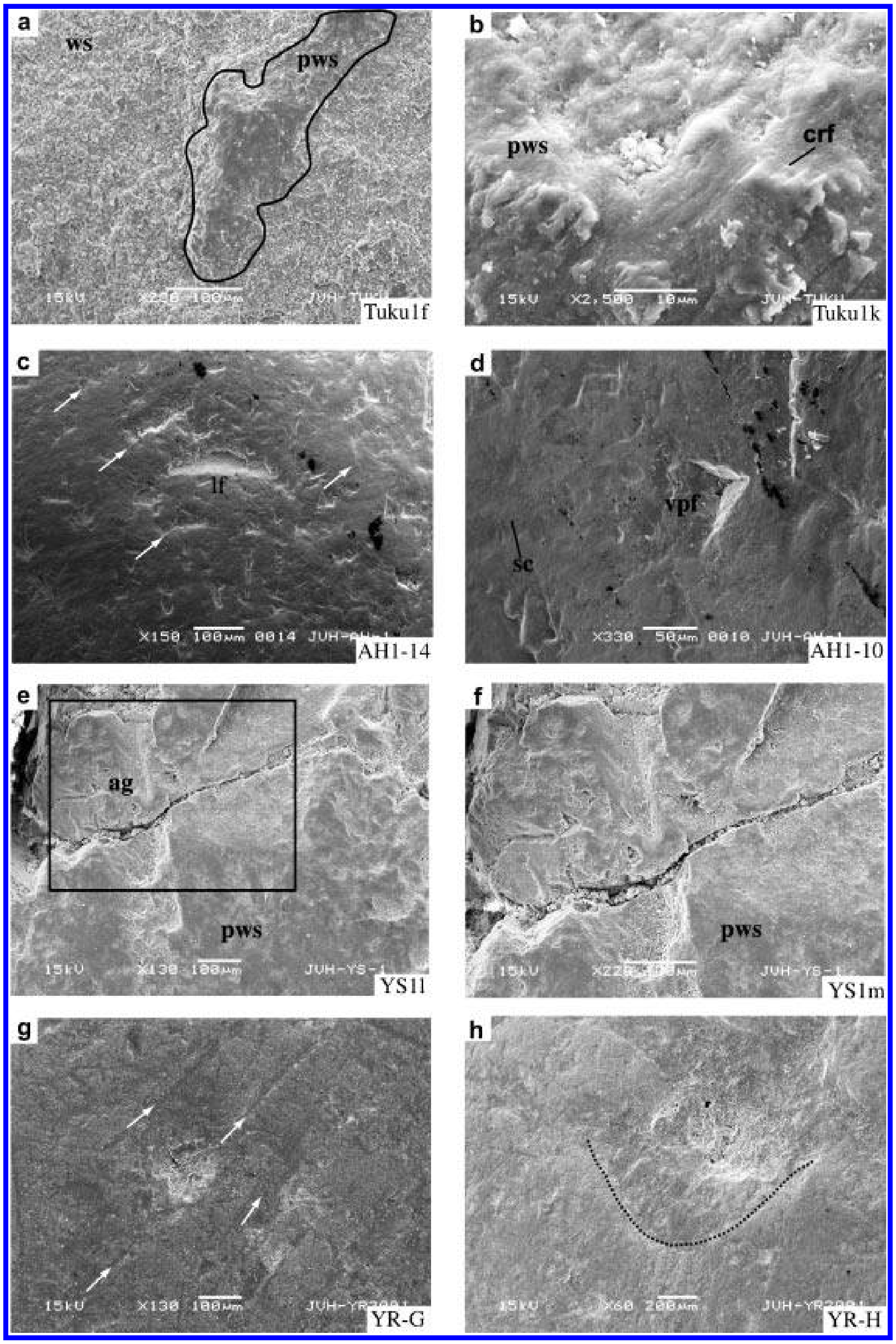

Fig. 6. SEM photomicrographs of representative nonglacial features on fluvial and lacustrine samples from the Spring Mountains, Klondike Gravel, and Lake Bonneville shoreline. (*a*) Surface of limestone showing numerous V-shaped percussion features (vpf), (*b*) close-up of scouring features (sc) and relict surface, (*c*) numerous V-shaped percussion features and rare arcuate gouges (arrows), (*d*) close-up of vpf outlined in *c*, (*e*) surface of shoreline exhibiting scouring features and arcuate gouges (ag) but predominantly V-shaped percussion features (arrows), and (*f*) shoreline exhibiting numerous V-shaped percussion features (arrows).

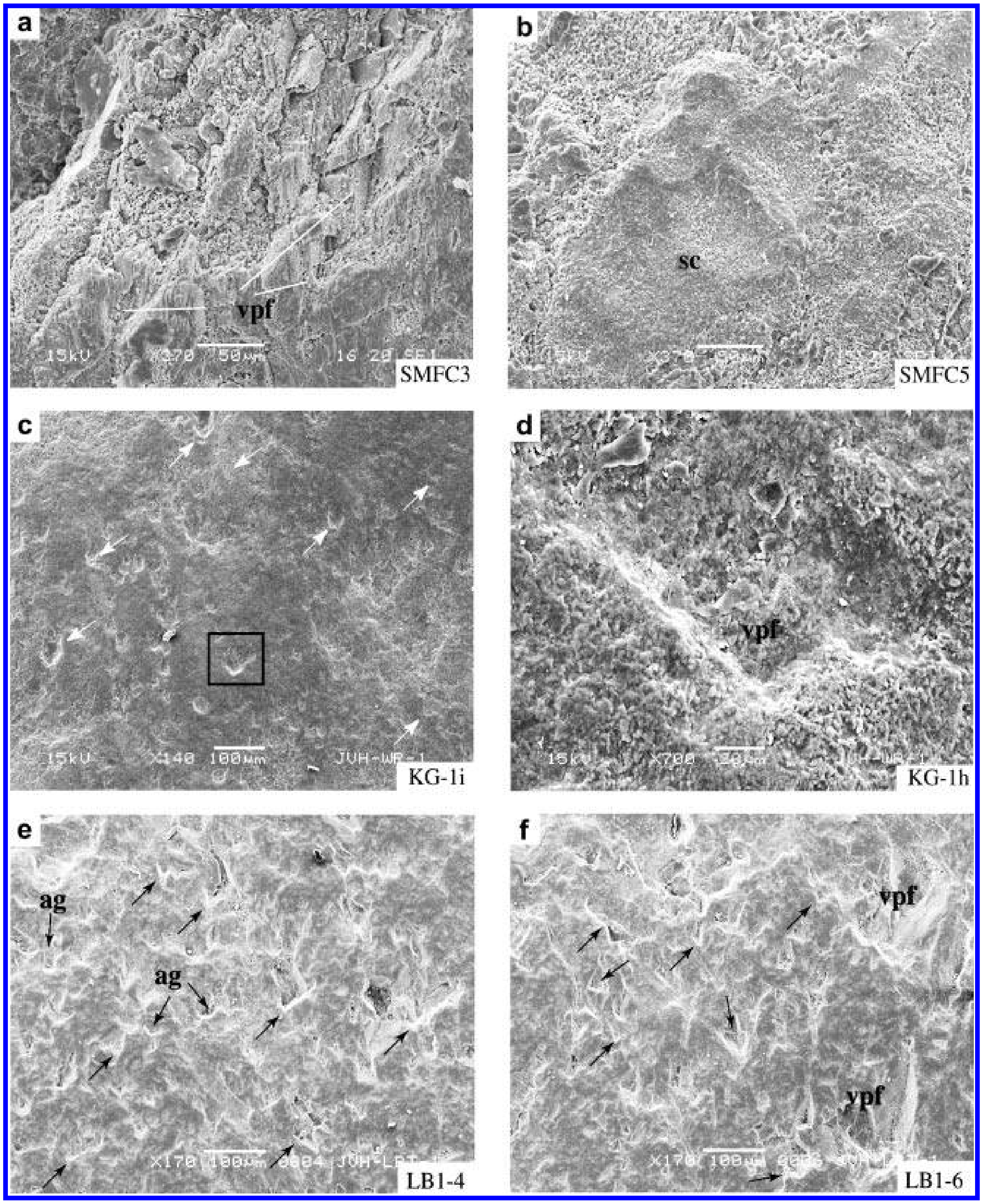

features are visible in the field using a hand lens. SEM analyses indicate the presence of well-developed V-shaped percussion features that are ~25–100 µm wide at their widest point, prominent scouring features, and edge rounding (Fig. 6).

Lake Bonneville

Lake Bonneville occupied closed depressions in the eastern Great Basin and covered ~20 000 mi^2 (1 mi^2 = 2.59 km^2) at its greatest extent. Lake Bonneville created three major shorelines, the Provo, Bonneville, and Stansbury shorelines, that can be identified as terraces on many mountains throughout western Utah, eastern Nevada, and southern Idaho (Oviatt et al. 1992). Four samples of Quartzite of Clarks Basin were collected from a Bonneville-age terrace in northeastern Utah at ~1553 masl (Fig. 2*h*).

Samples from the wave-cut terrace are well polished and show visible signs of scouring and abrasion. Striations,

Fig. 7. Frequency of observed microfeatures differentiated by glacial, nonglacial, and mixed formational environments.

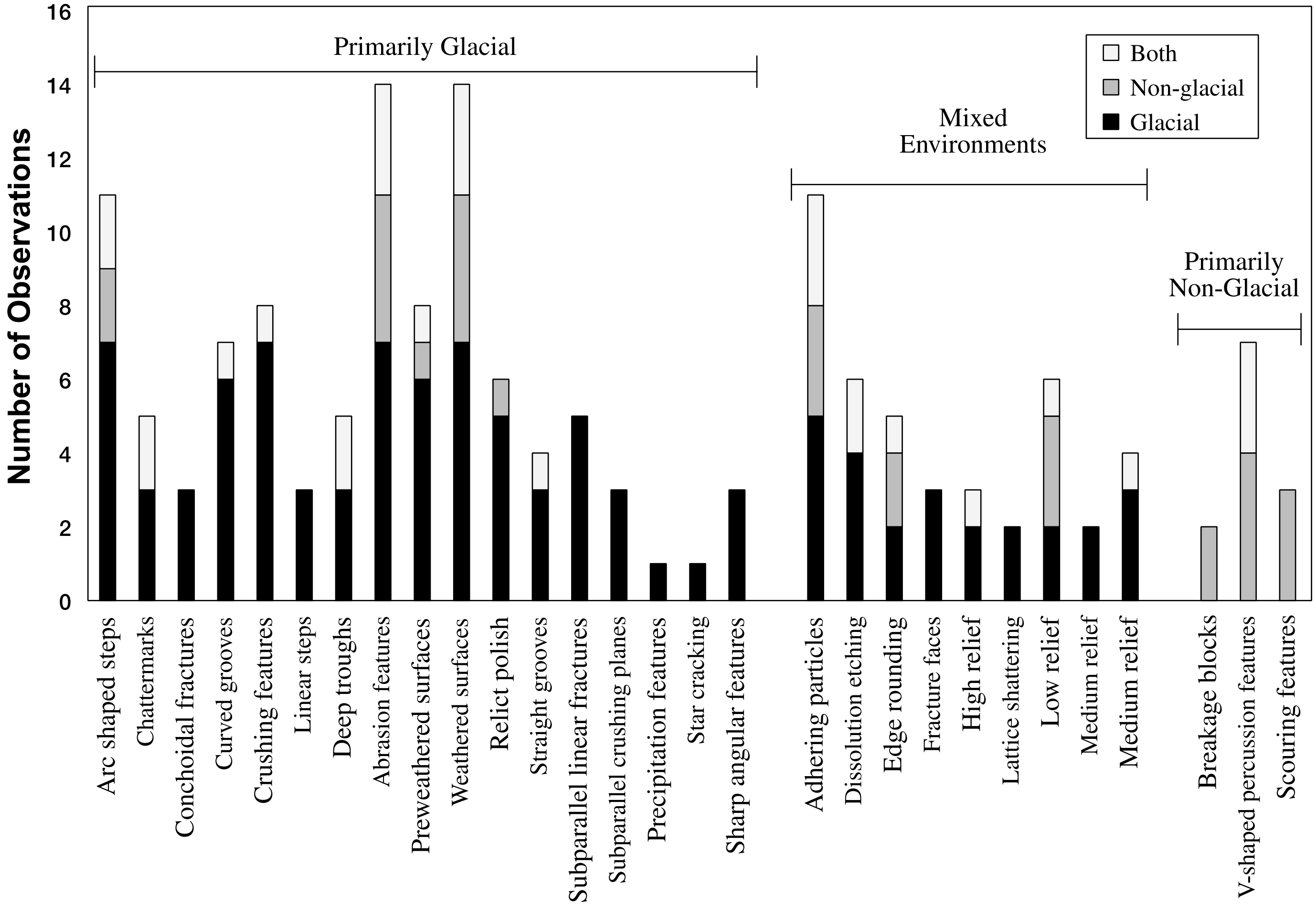

chattermarks, and crescentic gouges are not visible in the field with a hand lens. These samples exhibit V-shaped percussion features that are ~25–75 µm wide, arcuate grooves that are ~5–20 µm wide, scouring features, and relict polish preserved as preweathered surfaces (Fig. 6).

Discussion

Previous workers identified subparallel conchoidal and linear fractures, directional curved troughs in multiple sets, cresentic gouges, crushing features, and arc-shaped steps on quartz grains from glacial environments (Krinsley and Doornkamp 1973; Mahaney 1995, 2002; Mahaney and Kalm 2000; Mahaney et al. 1996, 2001). They note the depth and preferred orientation of fractures and striations on grains affected by glacial processes. The consistency of a preferred orientation and well-developed, deeply entrenched morphology of such features suggest they are diagnostic of a glacial origin and are not derived from eolian, fluvial, or other processes. However, this does not mean these features can not develop through processes other than glacial transport. The development of microscale striations, grooves, and troughs has also been attributed to dissolution etching in weak hydrochloric acid and the affects of river ice (Wentworth 1928; Dunn 1933). The morphology of the striations and polish, and abundance of clasts from the same environment exhibiting similar characteristics in this study, suggest they are not dissolution features. It is also unlikely they reflect an environment that could sustain river ice since almost all of these samples are collected from arid regions or alpine localities. However, in this study we differentiate among three groups of samples: (1) those that were only affected by glacial activity, (2) those only affected by nonglacial processes, and (3) samples that were transported or modified by both glacial and nonglacial processes (e.g., glaciofluvial, eolian, and lacustrine). Each group of samples exhibits distinct microfeatures indicative of the specific environment from which they were derived. Figure 7 illustrates the frequency of microfeature versus the environmental conditions where the samples were collected. Although this is primarily a qualitative assessment of the data, this chart mirrors the findings of previous workers who have related certain microfeatures to specific environments and processes (Table 1).

Microfeatures are most readily preserved in samples with a homogeneous mineralogy. Samples of polymineralic granite, trachyte, and pillow basalt display the most evidence for post-depositional weathering and weakly preserved microfeatures compared with more homogeneous samples of chert, quartzite, and limestone. Samples from Snake Creek and Spring Mountains exhibit the best-preserved features but are thought to be older than many of the other samples. It is likely the Snake Creek samples retain their features because quartz is so resistant to erosion and weathering, although the Spring Mountain samples are anomalously pristine given their

Fig. 8. Schematic diagram illustrating the most likely relationship between the preservation of microfeatures in relation to lithology and age of the samples. With increasing age and decreasing lithologic competence, microfeatures should be less common; however, the samples in this study with the best-preserved microfeatures are assumed to be older than many of the other samples.

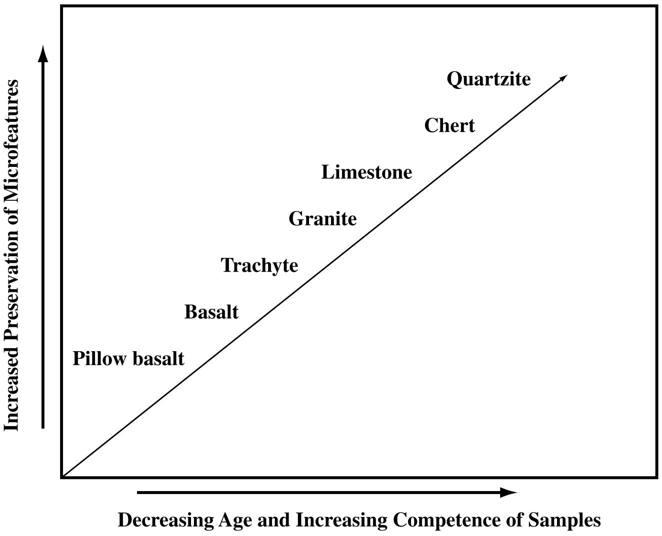

presumed age. Limestone is highly susceptible to dissolution etching and weathering, so the excellent preservation of microfeatures on samples from the Big Falls till is thought to reflect their burial through mass wasting events and subsequent isolation from most physical and chemical weathering processes (Orndorff and Van Hoesen 2003). However, both the older and younger Fish Lake samples illustrate expected effects of weathering on preservation of microfeatures through time. Features observed on the older Fish Lake samples are not only more subdued and less well preserved than those on younger Fish Lake samples, but many of the characteristic features attributed to glacial action are lacking. The preservation of these features is directly affected by the amount of time spent on the surface of a landform or contained in a glacial–nonglacial deposit. The samples from Devils Postpile National Monument, Yosemite National Park, Snake Creek, La Sal Mountains, and Fish Lake region were collected at sites with direct exposure to the elements. Increased surface area and exposure to physical and chemical weathering processes most certainly causes a higher rate of microfeature degradation than typically observed on quartz grains. The likelihood of preservation for microfeatures as a function of relative age and lithology is illustrated in Fig. 8. Additionally, samples from Devils Postpile National Monument and Yosemite National Park are thought to have experienced greater basal shear stress and were affected more by basal grinding and abrasion than the rest of the sample population, which were collected from till. The combination of higher shear stress, which is more damaging to the crystalline structure of the bedrock, and the lack of environmental protection provided by the matrix of glacial till (Yount and LaPointe 1997; Orndorff et al. 2003), certainly contributes to the decay of many microfeatures.

The presence of cresentic gouges, arcuate steps, conchoidal fractures, subparallel linear fractures, and chattermarks are diagnostic indicators of glacial transport. Samples collected from the Snake Range, Spring Mountains, Devils Postpile, Yosemite, Fish Lake, and the La Sal Mountains exhibit these diagnostic microfeatures. All these features developed in response to vibrational energy released during stick-slip processes and (or) subglacial grinding (Boulton and Hindmarsh 1987; Barcilon and MacAyeal 1993; Boulton 1996; Mahaney 2002). However, similar to Mahaney et al. (1988*a*, 1988*b*), microfeatures observed on chert samples from the Yukon River and Allan Hills are more frequent and deeply engrained than in samples collected from areas affected by alpine glaciation.

V-shaped percussion features were only identified on clasts affected by glaciofluvial activity, with the exception of the Alan Hills and Yukon River samples. Previous studies have documented the prevalence of V-shaped percussion features on quartz grains from tills deposited by alpine glaciers compared with quartz grains deposited by continental glaciers (Mahaney et al. 1988*b*; Mahaney 1995). These samples (Alan Hills and Yukon River) were collected from tills deposited by continental glaciers and record a complex history resulting from the interaction of fluvial and (or) glaciofluvial processes prior to incorporation into glacial ice. The lack of V-shaped percussion features on samples collected from bedrock surfaces (Yosemite and Devils Postpile) is consistent with our expectations that they develop in fluvial environments; however, the absence of such features on samples from alpine moraines and rock glaciers suggests a short non-aqueous transport distance. Field relationships indicate sources for these samples are primarily frost-riven talus from local cirques (e.g., samples were collected from lateral moraine crest and the terminus of a rock glacier breaching a cirque bedrock sill). We infer that talus is transported into the cirque basin through mass wasting and rockfall events and that transport downvalley is primarily achieved through glacial advance rather than fluvial or glaciofluvial processes, and so the lack of V-shaped percussion features is not surprising.

Many of the microfeatures (arc-shaped steps, crescentic gouges, deep grooves, etc.) described in this study are thought to have developed during transport by glaciers > 500 m thick in response to glacial abrasion and high basal shear stress (Mahaney et al. 1988*b*, 1991; Mahaney 1990*b*). This relationship is not reflected in our study because many of the samples are less competent lithologies than quartzite and therefore should require less basal shear stress to produce similar features. They may also be produced in alpine environments that are characterized by glacial ice containing abundant coarse material and steep bed gradients, which can affect the average shear stress at the base of the glacier (Benn and Evans 1998). We believe the most important factor is the competence and homogeneity of bedrock and availability of material being transported by the glacier (Iverson 1990, 1995; Shoemaker 1988). The homogeneity of samples is not thought to affect the frequency of occurrence of microfeatures as much as the preservation of these features.

Conclusions

This study suggests that distinct microfeatures are present on striated clasts with a glacial origin and that they can be used to differentiate between diamictons of a glacial versus nonglacial origin (Fig. 7). Samples from seven glacial environments are dominated by arc-shaped steps, chattermarks, curved grooves, deep troughs, fracture faces, linear steps, relict polish, subparallel linear fractures, and subparallel crushing planes. These features were primarily observed on samples with a known glacial origin. Characteristic microfeatures for samples with a nonglacial origin are breakage blocks, scouring features, and V-shaped percussion features. Samples that were affected by both glacial and nonglacial processes exhibit a combination of these microfeatures including arc-shaped steps, chattermarks, and V-shaped percussion features. As with previous studies addressing the microtextures of quartz grains, we conclude that the presence of arc-shaped steps, chattermarks, deep grooves, and arcuate and conchoidal crushing features are diagnostic indicators of a glacial origin, and V-shaped percussion marks and abrasion scouring features are characteristic of fluvial and glaciofluvial environments. Further study on additional depositional environments and lithologies is necessary to evaluate the consistency of microfeatures. Furthermore, additional work should address the correlation between specific features documented on striated clasts and estimated ice thickness.

Acknowledgments

We would like to thank the Arizona–Nevada Academy of Science, Colorado Scientific Society, Sigma Xi Scientific Society, University of Nevada Los Vegas Graduate College, and The American Alpine Club for financial support of this project. We appreciate the cooperation of Great Basin National Park, Yosemite National Park, and Devils Postpile National Monument. We also thank Vic Levson and Phil Holme for supplying samples. We graciously thank Steve Hicock, Lionel Jackson, Fred Bachhuber, Steve Rowland, William Mahaney, John Shaw, and Robert Gilbert for their many comments and suggestions, which improved the quality of this manuscript.

References

Abd-Alla, M.A.A. 1991. Surface textures of quartz grains from recent sedimentary environments along the Mediterranean Coast, Egypt. Journal of African Earth Sciences, **13**: 367–375.

Agassiz, L. 1840. Etudes sur les glaciers. H. Nicolet, Aneuchatel, Suisse.

Alley, R.B. 1989. Water-pressure coupling of sliding and bed deformation. Journal of Glaciology, **35**: 108–139.

Atkins, C.B., Barrett, P.J., and Hicock, S.R. 2002. Cold glaciers erode and deposit: Evidence from Allan Hills, Antarctica. Geology, **30**: 659–662.

Bagnold, R.A. 1941. The physics of windblown sand and desert dunes. Methuen, London, UK.

Bailey, R.A. 1987. Long Valley caldera, eastern California. *In* The Long Valley Caldera Mammoth Lakes & Owens Valley region, Mono County, California. South Coast Geological Society, Santa Ana, Calif., Annual Field Trip Guidebook, pp. 54–59.

Bailey, R.A., and Hill, D.P. 1987. Magmatic unrest at Long Valley Caldera, California. *In* The Long Valley Caldera Mammoth Lakes & Owens Valley region, Mono County, California. South Coast Geological Society, Santa Ana, Calif., Annual Field Trip Guidebook, pp. 54–59.

Ballance, P.F., and Watters, W.A., 1971, The Mawson Diamictite and the Carapace Sandstone Formations of the Ferrar Group at Allan Hills and Carapace Nunatak, Victoria Land, Antarctica. New Zealand Journal of Geology and Geophysics, **14**: 512–527.

Barcilon, V., and MacAyeal, D.R. 1993. Steady flow of a viscous ice stream across a no slip/free transition at the bed. Journal of Glaciology, **39**: 167–185.

Bateman, P.C. 1992. Plutonism in the central part of the Sierra Nevada batholith, California. United States Geological Survey, Professional Paper 1483.

Benn, D.I., and Evans, D.J.A. 1998. Glaciers and Glaciation. Arnold, London, UK.

Boulton, G.S. 1968. Flow tills and related deposits on some Vestspitsbergen glaciers. Journal of Glaciology, **7**: 391–412.

Boulton, G.S. 1996. Theory of glacial erosion, transport, and deposition as a consequence of subglacial sediment deformation. Journal of Glaciology, **42**: 43–62.

Boulton, G.S., and Hindmarsh, R.C.A. 1987. Sediment deformation beneath glaciers: rheology and sedimentological consequences. Journal of Geophysical Research, **92**: 9059–9082.

Bjørlykke, K. 1974. Glacial striations on clasts from the Moelv Tillite of Late Precambrian of Southern Norway. American Journal of Science, **274**: 443–448.

Brown, J.E. 1973. Depositional histories of sand grains from surface textures. Nature, **242**: 396–398.

Bruno, L.A., Baur, H., Graft, T., Schluechter, C., Signer, P., and Wieler, R. 1997. Dating of Sirius Group tillites in the Antarctic dry valleys with cosmogenic (super 3) He and (super 21) Ne. Earth and Planetary Science Letters, **147**: 37–54.

Burchfiel, B.C. 1974. Geology of the Spring Mountains, Nevada. Geological Society of America Bulletin, **85**: 1013–1022.

Campbell, S., and Thompson, I.C. 1991. Palaeoenvironmental history of Late Pleistocene deposits at Moel Tryfan, North Wales: evidence from scanning electron microscopy. Proceedings of the Geological Association, **102**: 123–134.

Clarke, G.K.C. 1987. Subglacial till, a physical framework for its properties and processes. Journal of Geophysical Research, **92**: 9023–9036.

Cuffey, K.M., Conway, H., Hallet, B., Grades, A.M., and Raymond, C.F. 1999. Interfacial water in polar glaciers and glacier sliding at –17 °C. Geophysical Research Letters, **26**: 751–752.

Culver, S.J., Bull, P.A., Campbell, S., Shakesby, R.A., and Whalley, W.B. 1983. Environmental discrimination based on quartz grain surface textures: a statistical investigation. Sedimentology, **30**: 129–136.

Denton, G.H., and Hughes, T.J. 2002. Reconstructing the Antarctic Ice Sheet at the Last Glacial Maximum. Quaternary Science Reviews, **21**: 193–202.

Drewes, H. 1958. Structural geology of the southern Snake Range, Nevada. Geological Society of America Bulletin, **69**: 221–240.

Dunn, P.H. 1933. Parallel striations on etched limestone surfaces. American Journal of Science, **26**: 442–446.

Echelmeyer, K., and Wang, Z. 1987. Direct observations of basal sliding and deformatin of basal-drift at sub-freezing temperatures. Journal of Glaciology, **33**: 83–98.

Folk, R.L. 1975. Glacial deposits identified by chattermark tracks in detrital garnets. Geology, **8**: 473–475.

Froese, D.G. 1997. Sedimentology and paleomagnetism of Plio-Pleistocene lower Klondike valley terraces, Yukon. M.Sc. thesis, University of Calgary, Calgary, Alta.

Froese, D.G., Barendregt, R.W., Enkin, R.J., and Baker, J. 2000. Paleomagnetic evidence for multiple late Pliocene – early Pleistocene glaciations in the Klondike area, Yukon Territory. Canadian Journal of Earth Science, **37**: 833–877.

Froese, D.G., Enkin, R.J., and Smith, D.G. 2001. Placer depositional settings and their ages along Dominion Creek, Klondike area, Yukon. *In* Yukon exploration and geology 2000. *Edited by* D.S. Edmond and L.H. Weston. Exploration and Geological Services Division, Yukon, Indian and Northern Affairs Canada, pp. 159–169.

Glennie, K. 1970. Desert sedimentary environments. Developments in Sedimentology 14, Elsevier, Amsterdam, The Netherlands.

Hardy, C.T., and Muessig, S. 1952. Glaciation and drainage changes in the Fish Lake Plateau, Utah. Geological Society of America Bulletin, **63**: 1109–1116.

Heald, W.F. 1956. An active glacier in Nevada. The American Alpine Journal, **10**: 164–167.

Helland, P.E., and Diffendal, R.F., Jr. 1993. Probably glacial climate conditions in source areas during deposition of parts of the Ash Hollow Formation, Ogallala Group (Late Tertiary) of western Nebraska. American Journal of Science, **293**: 744–757.

Helland, P.E., Huang, Pei-Hua, and Diffendal, R.F., Jr. 1997, SEM analysis of quartz sand grain surface textures indicates alluvial/colluvial origin of the Quaternary “glacial” boulder clays at Huangshan (Yellow Mountain), East-Central China. Quaternary Research, **48**: 177–186.

Hicock, S.R., and Dreimanis, A. 1989. Sunnybrook drift indicates a grounded early Wisconsin glacier in the Lake Ontario basin. Geology, **17**: 169–172.

Higgs, R. 1969. Quartz grain surface features of Mesozoic-Cenozoic sands from the Labrador and western Greenland continental margins. Journal of Sedimentary Petrology, **39**: 599–610.

Holme, P. 2001. Field and scientific data report; Sirius Group study, Allan Hills, South Victoria Land, Antarctica, Nov. 1999 – Jan. 2000. Antarctic Data Series, 23.

Hunt, C.B. 1958. Structural and igneous geology of the La Sal Mountains, Utah. United States Geological Survey, Professional Paper 294-I, pp. 305–364.

Iverson, N.R. 1990. Laboratory simulations of glacial abrasion: comparison with theory. Journal of Glaciology, **36**: 304–314.

Iverson, N.R. 1995. Processes of erosion. *In* Modern glacial environments: processes, dynamics and sediments. *Edited by* J. Menzies. Butterworth-Heinemann, Oxford, UK.

Jackson, L.E., Huscroft, C.A., Gotthardt, R., Storer, J.E., and Barendregt, R.W. 2001. Field Guide: Quaternary Volcanism, Stratigraphy, Vertebrate Paleontology, Archaeology, and Scenic Yukon River Tour, Fort Selkirk Area (NTS 115 I), Yukon Territory, August 18–19. Yukon Heritage Brank Occasional Papers in Earth Sciences No.3, Geological Survey of Candada, 36 p.

Judson, S., and Barks, R.E. 1961. Microstriations on polished pebbles. American Journal of Science, **259**: 371–381.

Kamb, B. 1991. Rheological nonlinearity and flow instability in the deforming bed mechanism of ice stream motion. Journal of Geophysical Research, **96**: 585–595.

Krinsley, D.H., and Donahue, J. 1968. Environmental interpretation of sand grain surface textures by electron microscopy. Geological Society of America Bulletin, **79**: 743–748.

Krinsley, D.H., and Doornkamp, J.C. 1973. Atlas of quartz sand surface textures. Cambridge University Press, Cambridge, UK.

Krinsley, D.H., and Marshall, J.R. 1987. Sand grain textural analysis: An assessment. *In* Clastic particles: scanning electron microscopy and shape analysis of sedimentary and volcanic clasts. *Edited by* John R. Marshall. Van Nostand Reinhold Company, New York, New York.

Krinsley, D.H., Greeley, R., and Pollack, J. 1979. Abrasion of wind blown particles on Mars– erosion of quartz and basaltic sand under simulated Martian conditions. Icarus, **39**: 364–384.

Lee, D.E., and Christiansen, E.H. 1983*a*. The mineralogy of the Snake Creek – Williams Canyon pluton, southern Snake Range, Nevada. United States Geological Survey, Open File Report 83-337.

Lee, D.E., and Christiansen, E.H. 1983*b*. The granite problem in the southern Snake Range, Nevada. Contributions to Mineralogy and Petrology, **83**: 99–116.

Lee, D.E., and Van Loenen, R.E. 1971. Hybrid granitoid rocks of the southern Snake Range, Nevada. United States Geological Survey, Professional Paper 68, pp.1–46.

Lee, D.E., Stern, T.W., Mays, R.W., and Van Loenen, R.E. 1968. Accessory zircon from granitioid rocks of the Mt Wheeler Mine area, Nevada. United States Geological Survey, Professional Paper 600-D, pp. 197–203.

Lee, D.E., Marvin, R.F., Stern, T.W., and Peterman, Z.E. 1970. Modification of K–Ar ages by Tertiary thrusting in the Snake Range, White Pine County, Nevada. United States Geological Survey Professional Paper, 700-D, pp. 92–102.

Lee, D.E., Kistler, R.W., and Robinson, A.C. 1986. Muscovite phenocrystic two mica granites of northeastern Nevada are Late Cretaceous in age. *In* Shorter contributions to isotope research, *Edited by* Z.E. Peterman and D.C. Schanabel. United States Geological Survey, Bulletin B1622, pp. 31–39.

Mahaney, W.C. 1990*a*. Glacially-crushed quartz grains in late Quaternary deposits in the Virunga Mountains, Rwanda — indicators of wind transport from the north? Boreas, **19**: 81–89.

Mahaney, W.C. 1990*b*. Macrofabrics and quartz microstructures confirm glacial origin of Sunnybrook drift in the Lake Ontario basin. Geology, **18**: 145–148.

Mahaney, W.C. 1995. Pleistocene and Holocene glacier thicknesses, transport histories and dynamics inferred from SEM microtextures on quartz particles. Boreas **24**: 293–304.

Mahaney, W.C. 2002. Atlas of sand grain surface textures and applications. Oxford University Press, New York, N.Y.

Mahaney, W.C., and Andres, W. 1996. Scanning electron microscopy of quartz sand from the North-Central Saharan desert of Algeria. Zeitschrift fur Geomorphologie, **103**: 179–192.

Mahaney, W.C., and Kalm V. 1995. Scanning electron microscopy of Pleistocene tills in Estonia. Boreas, **24**: 13–29.

Mahaney, W.C., and Kalm, V. 2000. Comparative SEM study of oriented till blocks, glacial grains and Devonian sands in Estonia and Latvia. Boreas, **29**: 35–51.

Mahaney, W.C., and Sjöberg, R. 1993. Scanning electron microscopy of quartz grains from two granite caves and a gorge system in Bohuslan, southwestern Sweden. Zeitschfrift fur Geomorphologie, **37**: 337–348.

Mahaney, W.C., Vortisch, W., and Fecher, K. 1988*a*. Sedimentary petrographic study of tephra, glacial and aeolian grains in a Quaternary paleosol sequence on Mount Kenya, East Africa. Géographie physique et Quaternaire, **42**: 137–146.

Mahaney, W.C., Vortisch, W., and Julig, P. 1988*b*. Relative differences between glacially crushed quartz transported by mountain and continental ice — some examples from North America and East Africa. American Journal of Science, **288**: 810–826.

Mahaney, W.C., Vaikmae, R., and Vares, K. 1991. Scanning electron microscopy of quartz grains in supraglacial debris, Adishy Glacier, Caucasus Mountains, USSR. Boreas, **20**: 395–404.

Mahaney, W.C., Claridge, G., and Campbell, I. 1996. Microtextures on quartz grains in tills from Antarctica. Palaeogeography, Palaeoclimatology, Palaeoecology, **121**: 89–103.

Mahaney, W.C., Stewart, A., and Kalm, V. 2001. Quantification of SEM microtextures useful in sedimentary environmental discrimination. Boreas, **30**:165–171.

Mahaney, W.C., Dirszowsky, R.W., Milner, M.W., Menzies, J., Stewart, A., Kalm, V., and Bezada, M. 2004. Quartz microtextures and microstructures owing to deformation of glaciolacustrine sediments in the northern Venezuelan Andes. Journal of Quaternary Science, **19**: 23–33.

Manickam, S., and Barbaroux, L. 1987. Variations in the surface texture of suspended quartz grains in the Loire River: An SEM study. Sedimentology, **34**: 495–510.

Manker, J.P., and Ponder, R.D. 1978. Quartz grain surface features from fluvial environments in northeastern Georgia. Journal of Sedimentary Petrology, **48**: 1227–1232.

Margolis, S.V., and Krinsley, D.H. 1974. Processes of formation and environmental occurrence of microfeatures on detrital quartz grains. American Journal of Science, **274**: 449–464.

Marshall, J.R. 1987. Clastic Particles. Van Nostrand Reinhold, New York, N.Y.

Matthes, F.E. 1930. Geologic history of the Yosemite Valley. United States Geological Survey, Professional Paper 160.

Matthews, John A., Shakesby, Richard A., McEwen, Lindsey J., Berrisford, Mark S., Owen, Geraint, and Bevan, Philip. 1999. Alpine debris-flows in Leirdalen, Jotunhemen, Norway, with particular reference to distal fans, intermediate-type deposits, and flow types. Arctic, Antarctic, and Alpine Research, **31**: 421–435.

Mazzullo, J., and Ritter, C. 1991. Influence of sediment source on the shapes and surface textures of glacial quartz sand grains. Geology, **19**: 384–388.

McGrew, A.J., and Miller, E.L. 1995. Geologic map of Kious Springs and Garrison 7.5′ Quadrangles, White Pine County, Nevada and Millard County, Utah. United States Geological Survey, Open File Report 95-10, 20 p.

Miller, E.L., Dumitru, T., Brown, R.W., and Gans, P.B. 1999. Rapid Miocene slip on the Snake Range-Deep Creek Range fault system, east-central Nevada. Geological Society of America Bulletin, **111**: 886–905.

Nicholas, J.W. 1991. Rock glaciers and the Holocene paleoclimatic record of the La Sal Mountains, Utah. Unpublished Ph.D. dissertation. University of Georgia, Athens, Ga.

Nicholas, J.W. 1994. Fabric analysis of rock glacier debris mantles, La Sal Mountains, Utah. Permafrost and Periglacial Processes, **5**: 63–66.

Nicholas, J.W., and Butler, D.R. 1996. Applications of relative age dating techniques on rock glaciers of the La Sal Mountains, Utah: An interpretation of Holocene paleoclimates. Geografiska Annaler, **78A**: 1–18.

Orndorff, R.L., Van Hoesen, J.G., and Saines, M. 2003. Implications of new evidence for Late Quaternary Glaciation in the Spring Mountains, Southern Nevada. Journal of the Arizona–Nevada Academy of Science, **36**(1): 37–45.

Osborn, G. 1990. The Wheeler Peak Cirque and Glacier/Rock Glacier. Report for the Great Basin Natural History Association.

Osborn, G., and Bevis, K. 2001. Glaciation in the Great Basin of the Western United States. Quaternary Science Reviews, **20**: 1377–1410.

Oviatt, C.G. Currey, D.R., and Sack, D. 1992. Radiocarbon chronology of Lake Bonneville, eastern Great Basin, USA. Palaeogeography, Palaeoclimatology, Palaeoecology, **99**: 225–241.

Pascoe, K.J. 1961. An introduction to the properties of engineering materials. Blackie, London, UK.

Piegat, J.J. 1980. Glacial Geology of Central Nevada. M.S. thesis, Purdue University, West Lafayette, Ind., 124 p.

Ratajeski, K., Glazner, A.F., and Miller, B.V. 2001. Geology and geochemistry of mafic to felsic plutonic rocks in the Cretaceous intrusive suite of Yosemite Valley, California. Geological Society of America Bulletin, **113**: 1486–1502.

Richmond, G.M. 1962. Quaternary stratigraphy of the La Sal Mountains, Utah. United States Geological Survey, Professional Paper 324.

Ross, M.L. 1998. Geology of the Tertiary intrusive complex centers of the La Sal Mountains, Utah: influence of preexisting structural features on emplacement and morphology. United States Geological Survey, Report B2158, pp. 61–83.

Russell, I.C. 1884. Quaternary history of the Mono Valley, California. 8th Annual report of the United States Geological Survey, pp. 267–394.

Sharp, R.P. 1938. Pleistocene glaciation in the Ruby–East Humbolt Range, northeastern Nevada. Journal of Geomorphology, **1**: 296–323.

Sharp, R.P., and Birman, J.H. 1963. Additions to classical sequence of Pleistocene glaciations, Sierra Nevada, California. Geological Society of America Bulletin, **74**: 1079–1086.

Shoemaker, E.M. 1988. On the formulation of basal debris drag for the case of sparse debris. Journal of Glaciology, **34**: 259–264.

Smalley, I.J. 1966. The properties of glacial loess and the formation of loess deposits. Journal of Sedimentary Petrology, **36**: 669–676.

Strand, K., Passchier, S., and Näsi, J. 2003. Implications of quartz grain microtextures for onset Eocene/Oligocene glaciation in Prydz Bay, ODP Site 1166, Antarctica. Palaeogeography, Palaeoclimatology, Palaeoecology, **198**: 101–111.

Stroeven, A., and Klehman, J. 1999. Age of Sirius Group on Mount Feather, McMurdo dry valleys, Antarctica, based on glaciological inferences from the overridden mountain range of Scandinavia. Global and Planetary Change, **23**: 231–247.

Van Hoesen, J.G., and Orndorff, R.L. 2000. Evidence for Pleistocene Glaciation in the Spring Mountains, Nevada. Geological Society of America, Abstracts with Programs, **32**(7).

Van Hoesen, J.G., and Orndorff, R.L. 2003. Using GIS to evaluate an enigmatic diamicton in the Spring Mountains, Southern Nevada. Professional Geographer, **55**: 207–217.

Watts. S.H. 1985. A scanning electron microscope study of bedrock microfractures in granites under high arctic conditions. Earth Surface Processes and Landforms, **10**: 161–172.

Yount, J., and LaPointe, D.D. 1997. Glaciation, faulting, and volcanism in the southern Lake Tahoe Basin. *In* Where the Sierra Nevada meets The Basin and Range. *Edited by* B. Dillet, L. Ames, L. Gaskin, and W. Kortemeier. The National Association of Geoscience Teachers, Far Western Section, 1997 Fall Field Conference, Field Trip Guidebook, pp. 34–56.

Wayne, W.J. 1984. Glacial chronology of the Ruby Mountains–East Humbolt Range, Nevada. Quaternary Research, **21**: 286–303.

Wentworth, C.K. 1928. Striated cobbles in southern states. Bulletin of the Geological Society of America, **39**: 941-954.

Whitebread, D.H. 1969. Geologic map of the Wheeler Peak and Garrison quadrangles, Nevada and Utah. United States Geologic Survey, Miscellaneous Survey Map I-578, scale 1 : 48 000.

This article has been cited by:

1. Barbara Woronko. 2016. Frost weathering versus glacial grinding in the micromorphology of quartz sand grains: Processes and geological implications. *Sedimentary Geology* **335**, 103-119. [Crossref]
2. Alexandre Nieuwendam, Jesús Ruiz-Fernández, Marc Oliva, Vera Lopes, Anabela Cruces, Maria da Conceição Freitas. 2016. Postglacial Landscape Changes and Cryogenic Processes in the Picos de Europa (Northern Spain) Reconstructed from Geomorphological Mapping and Microstructures on Quartz Grains. *Permafrost and Periglacial Processes* **27**:1, 96-108. [Crossref]
3. Sheida Makvandi, Georges Beaudoin, Beth M. McClenaghan, Daniel Layton-Matthews. 2015. The surface texture and morphology of magnetite from the Izok Lake volcanogenic massive sulfide deposit and local glacial sediments, Nunavut, Canada: Application to mineral exploration. *Journal of Geochemical Exploration* **150**, 84-103. [Crossref]
4. Mats O. Molén. 2014. A simple method to classify diamicts by scanning electron microscope from surface microtextures. *Sedimentology* **61**:7, 2020-2041. [Crossref]
5. Ellen A. Cowan, Poul Christoffersen, Ross D. Powell, Franco M. Talarico. 2014. Dynamics of the late Plio–Pleistocene West Antarctic Ice Sheet documented in subglacial diamictites, AND-1B drill core. *Global and Planetary Change* **119**, 56-70. [Crossref]
6. Ninna Immonen, Kari Strand, Antti Huusko, Juha Pekka Lunkka. 2014. Imprint of late Pleistocene continental processes visible in ice-rafted grains from the central Arctic Ocean. *Quaternary Science Reviews* **92**, 133-139. [Crossref]
7. Gerilyn S. Soreghan, Dustin E. Sweet, Nicholas G. Heavens. 2014. Upland Glaciation in Tropical Pangaea: Geologic Evidence and Implications for Late Paleozoic Climate Modeling. *The Journal of Geology* **122**:2, 137-163. [Crossref]
8. Ninna Immonen. 2013. Surface microtextures of ice-rafted quartz grains revealing glacial ice in the Cenozoic Arctic. *Palaeogeography, Palaeoclimatology, Palaeoecology* **374**, 293-302. [Crossref]
9. J.K. Hart. 8.10 Depositional Processes 113-126. [Crossref]
10. Georg Schwamborn, Lutz Schirrmeister, Franziska Frütsch, Bernhard Diekmann. 2012. Quartz weathering in freeze–thaw cycles: experiment and application to the el'gygytgyn crater lake record for tracing siberian permafrost history. *Geografiska Annaler: Series A, Physical Geography* **94**:4, 481-499. [Crossref]
11. Jane K. Hart, Kathryn C. Rose, Kirk Martinez. 2011. Subglacial till behaviour derived from in situ wireless multi-sensor subglacial probes: Rheology, hydro-mechanical interactions and till formation. *Quaternary Science Reviews* **30**:1-2, 234-247. [Crossref]
12. Ellen A. Cowan, Claus-Dieter Hillenbrand, Lauren E. Hassler, Matthew T. Ake. 2008. Coarse-grained terrigenous sediment deposition on continental rise drifts: A record of Plio-Pleistocene glaciation on the Antarctic Peninsula. *Palaeogeography, Palaeoclimatology, Palaeoecology* **265**:3-4, 275-291. [Crossref]
13. Georg Schwamborn, Hanno Meyer, Grigory Fedorov, Lutz Schirrmeister, Hans-W. Hubberten. 2006. Ground ice and slope sediments archiving late Quaternary paleoenvironment and paleoclimate signals at the margins of El'gygytgyn Impact Crater, NE Siberia. *Quaternary Research* **66**:02, 259-272. [Crossref]
14. M. Al-Suwaidi, B.C. Ward, M.C. Wilson, R.J. Hebda, D.W. Nagorsen, D. Marshall, B. Ghaleb, R.J. Wigen, R.J. Enkin. 2006. Late Wisconsinan Port Eliza Cave deposits and their implications for human coastal migration, Vancouver Island, Canada. *Geoarchaeology* **21**:4, 307-332. [Crossref]
15. JANE K. HART. 2006. An investigation of subglacial processes at the microscale from Briksdalsbreen, Norway. *Sedimentology* **53**:1, 125-146. [Crossref]

Proceedings World Geothermal Congress 2015
Melbourne, Australia, 19-25 April 2015

A Closer Look At Hydrothermal Alteration and Fluid-Rock Interaction Using Scanning Electron Microscopy

Bridget Y. Lynne

University of Auckland, Department of Engineering Science, 70 Symonds St, Auckland, New Zealand

b.lynne@auckland.ac.nz

Keywords: scanning electron microscopy, hydrothermal alteration, tracking reservoir conditions

ABSTRACT

Traditional techniques routinely used for hydrothermal alteration studies are X-ray diffraction (XRD) and petrographic microscopy. The addition of scanning electron microscopy (SEM) to these standard mineralogical analyses greatly enhances our knowledge and understanding of fluid-rock interactions in our geothermal systems. SEM observations on core from geothermal fields in New Zealand and USA show the advantages of adopting SEM to better understand subsurface processes. SEM imagery reveals detailed nano to micron scale information on crystal-crystal relationships. For example significant changes in subsurface environmental conditions such as cooling after boiling, or an increase in acidity at depth over time, can be tracked using SEM. The advantage of SEM is that it examines intact rock samples while XRD requires samples to be crushed and samples for petrographic thin sections are ground down to produce smooth surfaces. These crushing and grinding processes remove much of the mineralogical detail. SEM imagery also reveals crystal-clay relationships which are important, as in some settings clays attach to and alter crystal surfaces which influence porosity, permeability and rock strength. In other cases the clays do not alter crystal surfaces. Furthermore, SEM findings in this study include detail on clay-clay relationships, such as clay inter-bedding, differences in clay maturity, crystallinity and/or quantity. SEM observations allow fundamental questions to be addressed such as: (1) What influence do crystal and clay morphologies have on permeability? (2) How do crystal and clay inter-relationships affect permeability and/or rock strength? (3) How are the rocks reacting to ongoing changes in subsurface environmental conditions? (4) Are certain lithologies better suited for production or injection? (5) Which stratigraphic units are more likely to compress resulting in subsidence at the surface? SEM is a useful technique to examine fine-scale, fluid-rock interactions on core from production or injection wells.

1. INTRODUCTION

Traditional techniques used for mineralogical studies such as petrographic microscopy and X-ray Diffraction (XRD) require rock samples to be prepared in such a manner that often much of the information about fluid-rock interaction is lost. In the case of petrographic microscopy, thin sections of rock samples are ground down to create a flat surfaced, thin veneer of rock. XRD requires rock samples to be ground into a powder prior to analysis, losing all record of visual mineralogical relationships between individual crystals and their matrix. While both techniques provide useful information about the mineralogy of rock samples and fluid-rock interactions, Scanning Electron Microscopy (SEM) extends and enhances these traditional techniques. The advantage of SEM is that sample preparation enables whole rock samples to be used. This preparation method preserves vital information such as subtle fluid-rock reactions and crystal-clay interactions. Presented within this study are SEM images that show the level of detail that can be obtained from SEM. Examples shown in this paper are from a number of different geothermal reservoirs within New Zealand and the USA. Specific geothermal fields are not stated as it is the technique used to examine the rocks that is of importance in this paper, not the location of the fields.

2. SECTIONS THAT FOLLOW

Fine-scale alteration components such as dissolution textures, water-rock interactions, clay morphologies and crystal-clay relationships were tracked using scanning electron microscopy (SEM) and standard petrographic microscopy. SEM sample preparation consisted of mounting a representative section of core onto an aluminum stub and powder coating it with platinum (10 nm coating thickness) for ~ 7 minutes at 10 mA using a high resolution Polaron SC7640 sputter coater. Samples were examined under the SEM using a Phillips (FEI) XL30S field emission gun. Operating conditions were 5 keV accelerating voltage, a spot size of 3 µm, and a working distance of 5 mm. Electron Dispersive Spectroscopy (EDS) analyses were performed on samples to obtain semi-qualitative compositional data. EDS operating conditions were 20 keV accelerating voltage, with a spot size of 5 µm, and a working distance of 5 mm. EDS shows the elemental composition of the crystal you are analyzing enabling its mineralogy to be determined. Standard petrographic microscopy was used to determine microscale textures, which were compared with the SEM results. X-ray Diffraction (XRD) was used to determine the mineralogy of the samples.

3. RESULTS

3.1 Reservoir Conditions

The examination of cored rocks from geothermal drillholes using SEM can assist in our understanding of reservoir conditions. Often such changes are subtle requiring high resolution, fine-scale imaging of intact samples to appreciate the full extent of the host rock and thermal water interactions. Figures 1 and 2 provide examples of SEM imaging that capture the subtleties of fluid-rock interactions within geothermal reservoirs. Figure 1A displays the relationship between bladed calcite and quartz where at two sites newly-forming quartz crystals can be seen growing from bladed calcite. This relationship occurs when deep, near-neutral alkali chloride fluid flashes and boils as it ascends through volcanic host rocks, causing the fluid to lose steam and dissolved gases such as CO_2. The rapid loss of CO_2 near the site of first boiling results in the deposition of bladed calcite (Browne, 1978, Tulloch, 1982, Simmons and Christenson, 1994). Upon cooling after boiling, quartz crystals form. Figure 1B illustrates the relationship between bladed calcite and illite where illite formed after bladed calcite. Illite formation is favoured by the cooling of CO_2-rich fluids. Therefore identifying bladed calcite/quartz/illite sites within a core by SEM imaging enables the tracking of locations and depths of subsurface flashing and the identification of CO_2-poor versus CO_2-rich reservoir fluid.

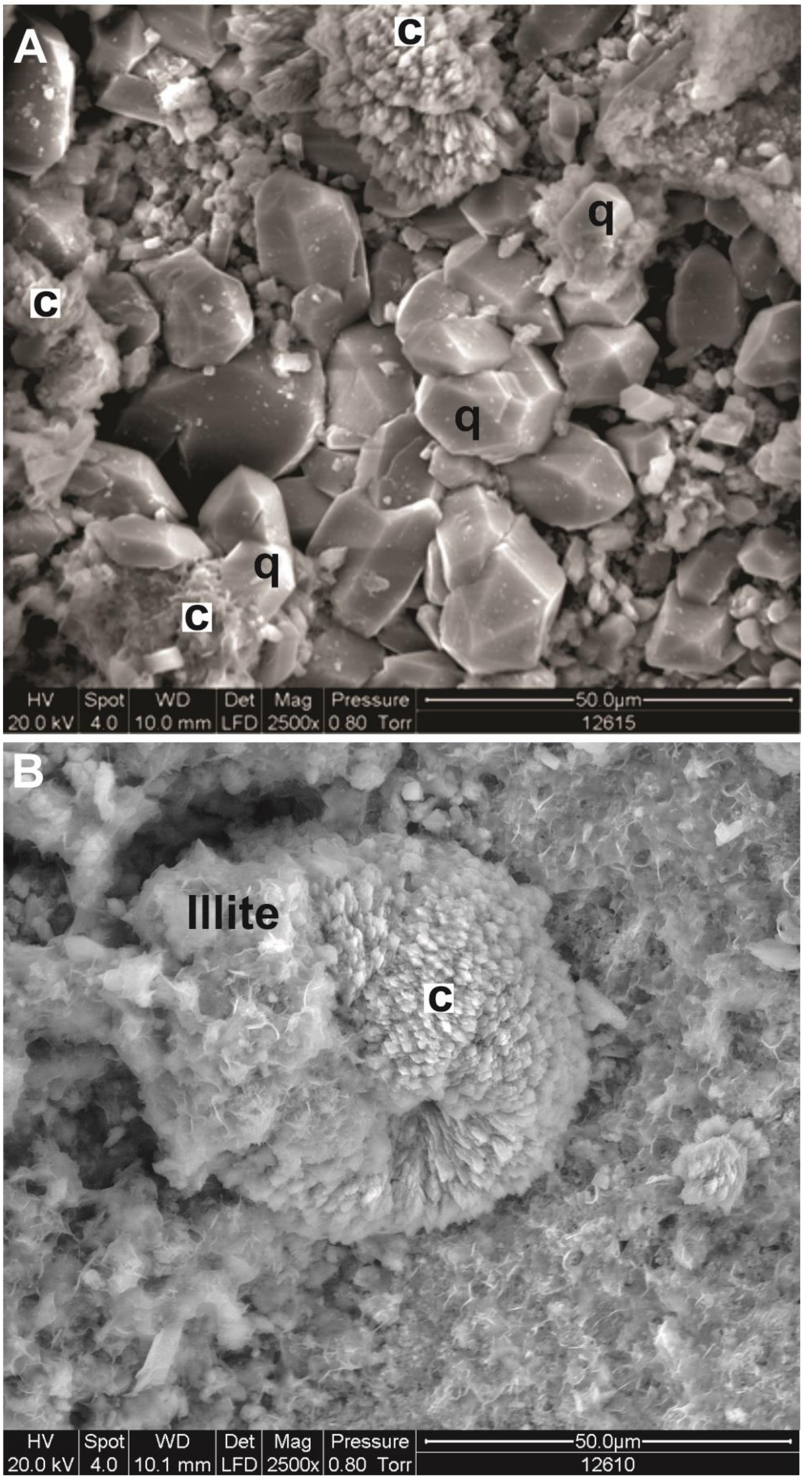

Figure 1: SEM images of core from a geothermal field. (A) The formation of quartz (q), bladed calcite (c), followed by further quartz formation. (B) Illite visible on top of bladed calcite (c) indicating it formed after the calcite.

Tracking changes within the reservoir fluid is important for maximizing the potential of both production and reinjection wells, as well as identifying possible sites of future subsidence. In Figure 2, SEM reveals the occurrence of illite and kaolin, whereby kaolin is observed resting on top of illite (Fig. 2B-C). Micro-environmental conditions for illite and kaolin differ. A pH of approximately 5 favours illite formation and a pH of around 3 favours kaolin formation (Allen et al., 1996). This finer-scale detail is not visible using petrographic microscopy (Fig. 2A). Such information is useful in many ways. For example, (i) it assists with assessment of well conditions with respect to well corrosion and fluid composition, (ii) mapping sections of a geothermal field that may be heating up or cooling down, (iii) identification of potential subsidence sites due to acidic alteration of the host rocks leading to a weakening and subsequent compaction of the rocks (Lynne et al., 2011).

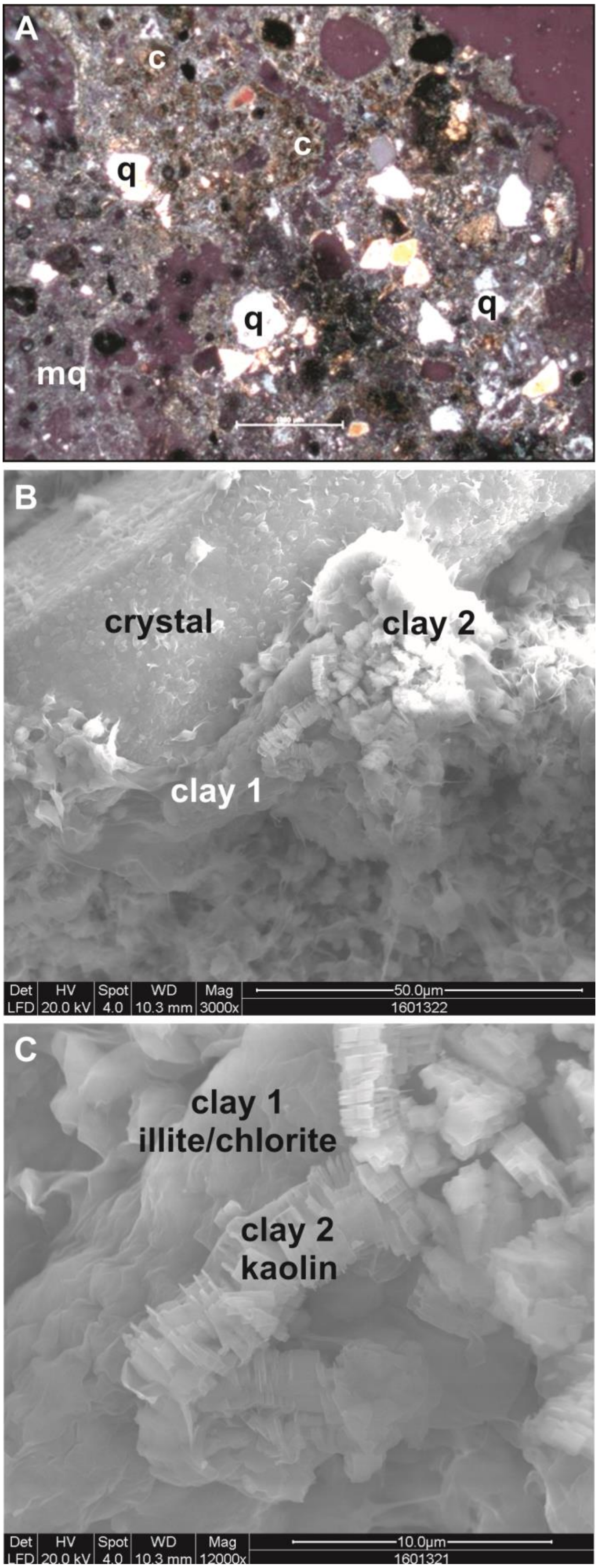

Figure 2: Tracking changes in the geothermal reservoir environmental conditions based on mineralogical observations of cored rock samples. (A) Petrographic microscope image shows quartz crystals (q) in a fine grained micro-crystalline quartz (mq) and clay matrix (c). (B-C) SEM images reveal illite/chlorite underlying kaolin inferring a decrease in temperature and increase in pH of the subsurface environment. Such detail is not evident in (A).

3.2 Clay minerals

Within geothermal systems clay minerals are known to often cause problems, specifically with decreasing permeability of wells. XRD clay mineral analysis provides a quick and easy way to identify which clay minerals are present within rock samples while petrographic examination reveals an overview of clay distribution within a host rock. SEM imaging coupled with EDS analysis offers additional information not retrievable using other techniques. SEM imaging reveals the degree of clay crystallinity (Fig. 3A-C), and shows the variation in morphological characteristics related to the degree of maturation within the same clay type (Fig. 3A-C). This information is not recoverable from petrographic microscopy (Fig. 3D). Also SEM is useful for documenting morphological differences that can be related to subtle variations in the composition of mixed clay assemblages (Fig. 3E-G). Petrographic microscopy cannot offer this fine-scale detail (Fig. 3H). Such morphological and/or compositional differences may affect well permeability therefore it is beneficial to include SEM imaging of clay minerals when studying the mineralogy of core from geothermal systems.

3.3 Crystal degradation and crystal-clay relationships

Fluid-rock interactions often result in hydrothermal alteration of host rocks which affect measurable parameters of the rock such as density, porosity, permeability, clay content and rock strength. For example, precipitation of new minerals decreases the rocks porosity and potentially its permeability. Dissolution however, can increase its porosity and permeability and weaken the formation if sufficient dissolution takes place.

SEM provides insights to the subsurface processes taking place and altering rocks (Fig. 4). The initial formation of open chlorite platelets (Fig. 4A) and illite (Fig. 4B) reveals different clay morphologies and crystal-clay relationships. In Figure 4A, open chlorite platelets protrude from feldspar crystals but the crystals are relatively unaltered. In Figure 4B the initial formation of illite is shown as elongated strips attached to the entire surface of a partially degraded feldspar crystal surface. Figure 4C-D shows clay minerals with a mixed chlorite-illite composition and two distinctly different crystal degradation processes. Figure 4C reveals complete dissolution of half of a feldspar crystal as it transforms into chlorite-illite clay minerals. This process would increase the host rocks porosity and possibly permeability, as well as weaken the formation. Figure 4D shows partial dissolution of the elongated surface of a feldspar crystal and transformation of the crystal surface into clay minerals. Here, porosity, permeability and strength of the host rock would be less compromised than that shown in Figure 4C. Figure 4E-F show crystal-clay inter-relationships where the clay and crystals co-exist with little effect on the overall porosity, permeability or strength of the formation. Figure 4E illustrates how illite clay can be present in abundance within the matrix of a rock but not attach to or erode crystal surfaces. Figure 4F shows chlorite embedding a lithic fragment with no fragment degradation.

3.4 Minor quantities of minerals detectable using SEM

All analytical techniques are limited by their lowest detection limits. However, it may be that a trace element or mineral of significant importance is present in minor quantities and undetectable due to equipment limitations. SEM and EDS can determine subtle changes within a host rock, such as minor elemental changes across micro-fractures, at crystal or formation boundaries and can image crystals or clays even if only present in minor quantities. Often it is these minor elemental changes that provide important information about subsurface environments and are of significance for exploration of hydrothermal systems.

Figure 5A-B shows SEM images of gold within a siliceous sinter deposit (hot spring rock). This sample was recovered from a core taken within a geothermal field. XRD and XRF analyses of this sample only detected the presence of silica, as gold was not present in sufficient quantity to be detected by these methods. Figure 5A-B reveals the bulk of the rock consists of opal-A/CT silica where the opal-A/CT nanospheres are psuedomorphing botryoidal opal-A spheres (Lynne et al., 2005). Using SEM, banded gold was imaged within some of the low areas between silica spheres. The gold strands form long ribbon-like structures. EDS of the banded elongated structures confirmed it to be gold. This sample was collected from a sinter located within a known gold mining area, however, this example shows how useful SEM can be to detect subtle but significant mineralogical information about an area.

4. CONCLUSIONS

SEM is a useful technique for all aspects of mineralogical studies on rocks from geothermal systems and compliments traditional analytical techniques such as petrography and XRD. SEM, petrography and XRD all offer useful data and when combined provide detailed information on fluid-rock interaction. Petrographic analysis documents large-scale, mineralogical relationships while XRD identifies mineralogical composition. The SEM high resolution detailed images taken at the nanoscale provide information about water-rock interactions and subsurface processes that are not obtainable using other techniques. Identifying subtle variations in crystal and clay morphologies, crystallinity, compositions and crystal-clay inter-relationships are important for our understanding of broader issues within our geothermal systems such as: (1) identifying boiling zones; (2) mapping the distribution of CO_2-rich versus CO_2-poor fluid movement in the reservoir rocks; (3) tracking temperature changes within a system, (i.e., is it heating up or cooling down with time); (4) identifying zones of potential weakness due to crystal degradation which may lead to subsidence at the surface; (5) documenting sites where environmental changes are taking place over time such as a pH decrease which may lead to a weakening of the formation; (6) mapping the distribution, composition and morphology of clay minerals as clays often play a significant role in decreasing productivity of both production and reinjection wells; and (7) identification of minor but significant minerals within a host rock.

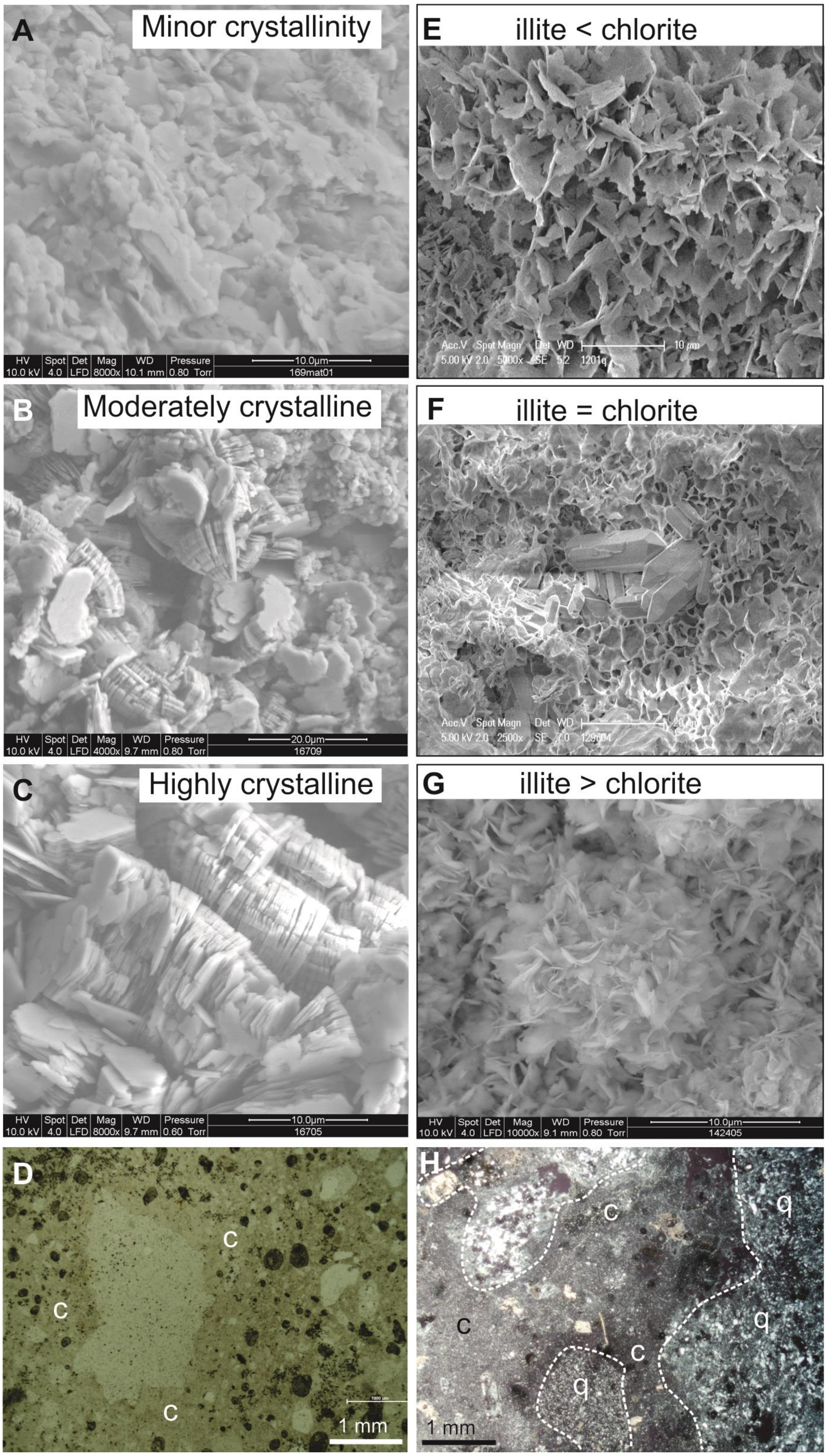

Figure 3: Clay morphologies. (A-C) Kaolin clay in a minor, moderate and highly crystalline form reveals different morphologies for each degree of crystallisation. (D) Clay (c) shown in (C) appears as a tan coloured, fine-grained matrix under petrographic microscopic examination. (E-G) Mixed illite-chlorite clay minerals with different quantities of illite versus chlorite show a range of morphologies. (H) Petrographic microscopy image shows overview of (G) with clay (c) and micro-crystalline quartz (q).

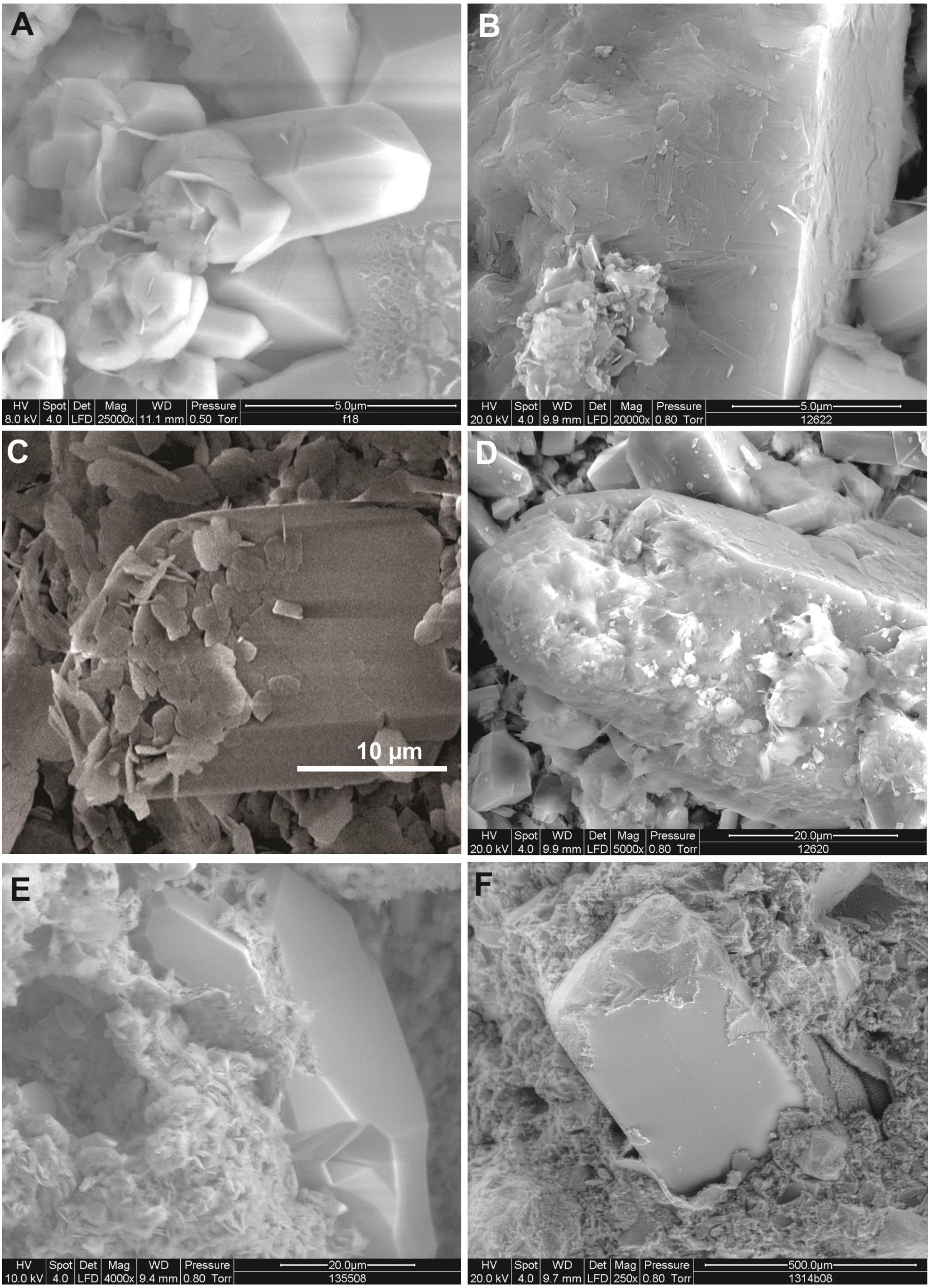

Figure 4: SEM images display various degrees of crystal degradation and clearly reveal the spatial relationships between crystals and clays. (A) Early chlorite formation on some feldspar crystal surfaces. (B) Early illite formation shown as thin strips on uneven, partially degraded, feldspar crystal surface. (C-D) Transformation of feldspar crystals into mixed chlorite-illite clay minerals. (E) Illite clay surrounding and infilling fractures within a feldspar crystal but no illite has attached to the crystal surface. (F) Lithic fragment embedded in chlorite. No degradation of fragment surface.

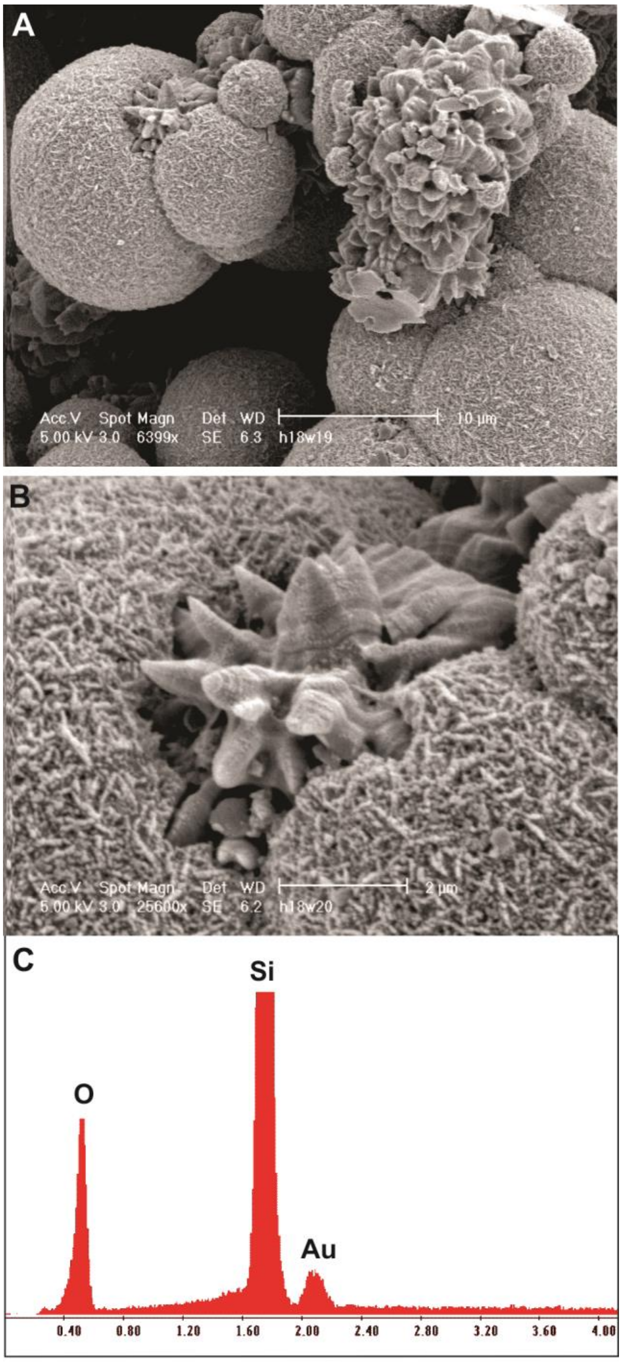

Figure 5: Banded strands of gold within an opal-A/CT siliceous sinter deposit identified in core recovered from a geothermal field. (A) Overview of gold strands within an opal-A/CT siliceous sinter deposit. (B) Elongated strand of banded gold in low area surrounded by aligned rows of opal-A/CT nanospheres. (C) EDS scan of elongated strand of gold shown in (B).

ACKNOWLEDGEMENTS

I would like to acknowledge Contact Energy, the Foundation for Research of Science and Technology and the Federation of Graduate Women who funded this research.

REFERENCES

Allen, R.L., et al.: A field and petrographic guide to hydrothermal alteration minerals. Thompson, A.J.B., and Thompson, J.F.H., (Eds.), Atlas of alteration, *Geological Association of Canada Mineral Deposits Division*, **119**, (1996).

Browne, P.R.L.: Hydrothermal alteration in active geothermal fields, *Annual Reviews Earth Planetary Science*, **6**, (1978), 229-250.

Lynne, B.Y., Campbell, K.A., Moore, J.N. and Browne, P.R.L: Diagenesis of 1900-year-old siliceous sinter (from opal-A to quartz) at Opal Mound, Roosevelt, Utah, U.S.A., *Sedimentary Geology*, **119**, (2005), 249-278.

Lynne, B.Y., Pender, M. and Glynn-Morris, T.: Scanning electron microscopy and compressibility measurements: A dual approach providing insights into hydrothermal alteration and rock strength at Tauhara geothermal field, New Zealand, *New Zealand Geothermal Workshop*, (2011).

Simmons, S.F. and Christenson, B.W.: Origins of calcite in boiling geothermal systems, *American Journal of Science*, **294**, (1994), 361-400.

Tulloch, A.J.: Mineralogical observations on carbonate scaling in geothermal wells at Kawerau and Broadlands, *4th New Zealand Geothermal Workshop*, (1982), 131-134.

Clays and Clay Minerals, 1971, Vol. 19, pp. 49–54. Pergamon Press. Printed in Great Britain

SCANNING ELECTRON MICROSCOPY OF CLAYS AND CLAY MINERALS

B. F. BOHOR and RANDALL E. HUGHES
Illinois State Geological Survey, Natural Resources Building, Urbana, Ill. 61801

(*Received* 30 *April* 1970)

Abstract—The scanning electron microscope (SEM) proves to be ideally suited for studying the configuration, texture, and fabric of clay samples. Growth mechanics of crystalline units—interpenetration and interlocking of crystallites, crystal habits, twinning, helical growth, and topotaxis—also are uniquely revealed by the SEM.

Authigenic kaolins make up the bulk of the examples because their larger crystallite size, better crystallinity, and open texture make them more suited to examination by the SEM than most other clay mineral types.

INTRODUCTION

THE SCANNING electron microscope (SEM) is uniquely suited for studying clays because it affords a magnified, three-dimensional view of the unmodified (natural) clay surface with great depth of focus. The only sample preparation necessary for clays is a thin metallic coating, applied in a vacuum evaporator, which serves to prevent a build-up of electrons on the surfaces by conducting away static electricity. With the conventional transmission electron microscope (TEM), the surfaces of clay particles cannot be directly observed, and only by an involved and time-consuming procedure of replication can they be viewed at all.

A simple description of the principles of operation and performance of the SEM is excerpted below from the sales brochure of the Advanced Metals Research Corporation (1969, p. 2):

> Resolution is of the order of 200Å and the useful magnification, up to about 50,000 ×, is in a convenient range lying between that of the light optical microscope and the transmission electron microscope. Most important, however, the depth of focus one obtains is of the order of tens of microns. This means that a fairly rough surface, such as produced by a metal fracture or exhibited by a small biological specimen, will remain entirely in focus at high magnifications. The micrograph obtained is similar in appearance to that of the reflection light microscope but, again, with much better resolution and depth of focus.
>
> The principle of operation of the SEM is by now quite familiar. An electron optical column, containing electromagnetic lenses, demagnifies an electron source in order to focus a fine beam of electrons on the specimen surface. This beam is scanned across the specimen surface in a rectangular raster in synchronism with the spot of a cathode ray tube. The signal resulting from interaction of the beam with the specimen is collected by a suitable electron detector and used to modulate the CRT brightness. In most applications it is the low-energy secondary electrons which are thus used to form a picture of the specimen on the CRT face.

With the installation 2 years ago of a Stereoscan SEM (Cambridge Electronic Instruments Ltd.,Cambridge, England) in the Central Facility for Electron Microscopes at the University of Illinois, we began a study to see what this new tool would reveal about clays and clay minerals. It immediately became apparent that certain clay minerals were more suited to examination than others because of their greater size, better crystallinity, and distinctive morphology. Some of the best results under the SEM were obtained from authigenic varieties of kaolinite. Because of this, and because of numerous projects at the Illinois State Geological Survey involving kaolinite, the majority of our observations have been on this mineral. However, we have included micrographs of many of the other common clay minerals to demonstrate the observations that can be made on any clay material with the SEM.

Many papers have been published on the applications of the SEM, but only a few are concerned with clay minerals. Borst and Keller (1969) studied many of the API Project 49 reference clays. Gillot (1969) and many other authors have included a few SEM micrographs of clays, but the instrument has not been extensively applied in clay mineralogical research. Perhaps this is because of the legacy of fine micrographs produced from replicas on the

TEM by Bates and Comer (1955), Beutelspacher and Van der Marel (1968), and others too numerous to mention. We hope to show, however, that the SEM, because of its unique operation and performance, can bring new dimensions to our understanding of clay minerals.

TECHNIQUE

Sample preparation is unusually simple for such a sophisticated instrument, and this greatly enhances its usefulness and applicability. Sample size is limited to about one-half cubic inch (1 in. × 1 in. × $\frac{1}{2}$ in.) in the instrument used, but newer models can accommodate specimens more than four times this volume.

Samples can be mounted by a variety of methods. Powders can be sprinkled directly on an adhesive mounting medium, such as Duco cement, double stick tape, or silver or chrome paint, or they can be sprayed on a metallic foil subsequently attached to the specimen stub; rock fragments may be directly mounted on the stub. Our mounting stubs (Engis Equipment Co., Morton Grove, Ill.) are aluminum discs 12 mm in dia. with a shank on the back. If small pieces of material are used, as many as six or eight samples can be accommodated on each stub, thereby avoiding time-consuming changing of specimens.

One of our first studies with the SEM was made during the development of a method of spray-drying clay minerals to reduce their preferred orientation in X-ray powder diffraction analysis (Hughes and Bohor, 1970). The method can be described simply as spraying a dilute clay suspension through a heater to form spherical aggregates of clay minerals. In theory, the clay platelets should be arranged with their basal surfaces tangential to the spherical water droplets formed during spraying and remain oriented in this fashion when the water is driven off in the heater. The resulting powder, composed mainly of spheres, can then be packed in the usual powder diffraction holders and any preferred basal (or other anisotropic) orientation should be eliminated. Clay minerals are thoroughly randomized by spray-drying, and therefore details of individual particle morphologies are more easily seen when some clays are prepared as sprayed powders for SEM examination.

Because clay materials are nonconductors of electrons, the samples must be coated with a thin layer of conductive material to prevent charge build-up. To accomplish this, a gold-palladium coating about 50–100 Angstroms (Å) thick is deposited on the samples by evaporation under high vacuum. This thin coating in no way modifies the surface details or hinders viewing, because the resolution of commercial SEM instruments is not less than 200 Å even under optimum conditions. To get a continuous conductive coating over the usually rough and porous surface of a clay sample, the metallic layer is deposited in two operations and at two different angles on a rotating stage. Thus the effective solid angle of incidence of the applied metallic layer approaches 90°, and it effectively coats all the available surfaces.

Because clay minerals are quite hygroscopic, the stub-mounted samples must be over-dried overnight before the coating is applied, and they should be kept dry after being coated to prevent rupture of the conductive layer and to shorten the microscope's pump-down time. To meet these requirements, the stub shanks are inserted into the base of a cork, which fits into a small glass or plastic vial. A small amount of dessicant is put into the vial, and, when the cork with its attached stub is inserted, an effective portable micro-dessicator results. The sample stubs can then be stored indefinitely in these vials and transported to the microscope in the optimum dry condition.

OBSERVED FEATURES OF CLAYS AND CLAY MINERALS

Certain features of clays and clay minerals are more readily observed on the SEM than by other conventional means. These features include those involving the surface and 3-dimensional aspects of clay minerals, such as the morphology (configuration) of samples, fabric (particle boundary relationships), texture (overall particle arrangements), and growth mechanics of crystals and crystallites. Examples of the latter feature shown here include the variations in layer (packet) thickness, crystal habit, topotaxis (crystallographic control of the development of later diagenetic minerals by preexisting minerals), twinning and spiral growth (helical growth about a central axis).

Configuration

Figures 1(a), 1(b), 2(a), and 2(b) show how the SEM can solve the problem of determining the morphology (configuration) of a spray-dried powder. Figure 1(a) is a highly magnified view of a natural rock sample of kaolinite from Anna, Illinois. White (1958) determined by particle-size and X-ray analyses that this clay was composed of unusually fine particles (more than 85 per cent of them less than 0·5 μ) of rather poorly crystallized kaolinite, and Fig. 1(a) confirms these determinations directly. Even the large plates of the clay appear to be composed of much smaller platelets. Figure 1(b) shows a spray-dried sample of this same Anna kaolinite, illustrating the typical spherical aggregates artificially formed during spraying and the

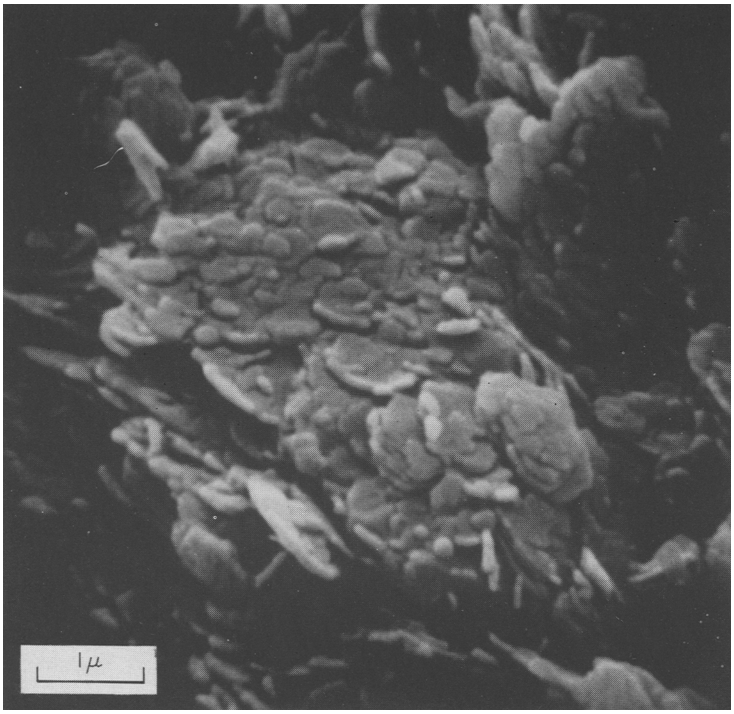

Fig. 1(a). Rock sample of kaolinite from near Anna, Union Co., Illinois (Cretaceous or Tertiary).

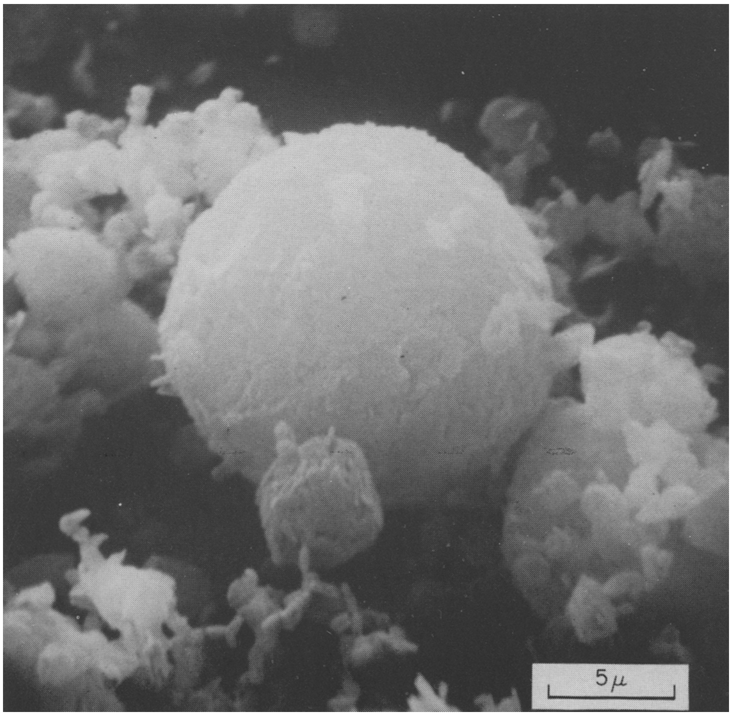

Fig. 1(b). Spray-dried kaolinite from near Anna, Union Co., Illinois.

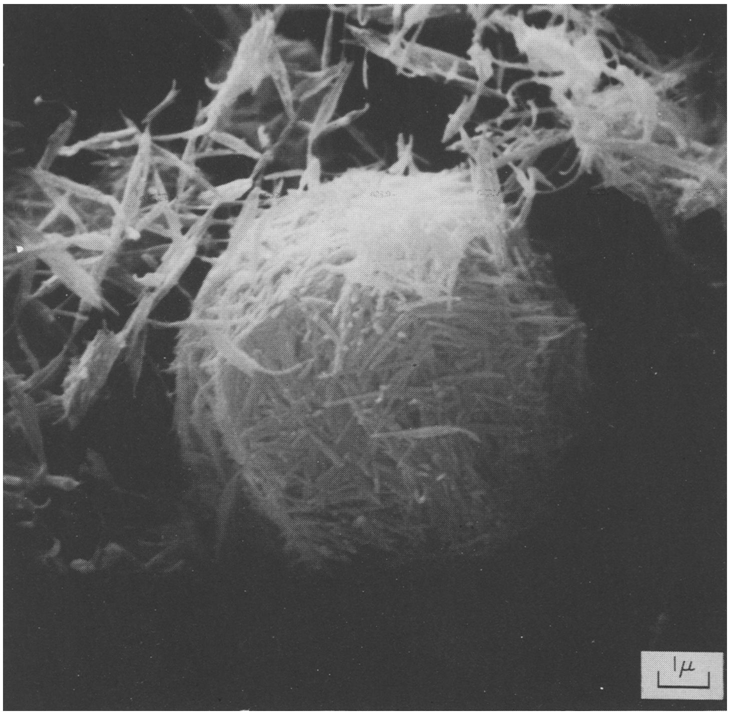

Fig. 2(a). Spray-dried attapulgite from Yucatan, Mexico.

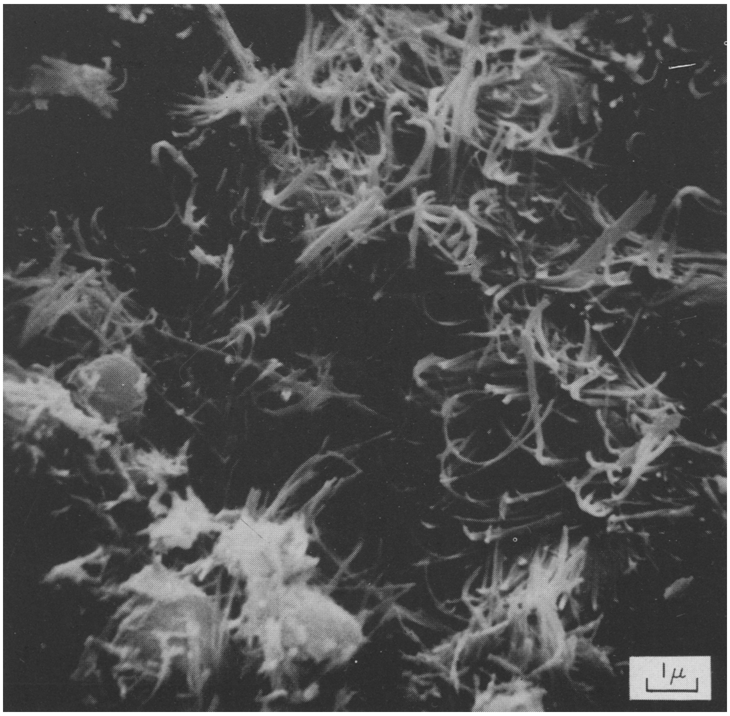

Fig. 2(b). Rock sample of attapulgite from Yucatan, Mexico (Tertiary).

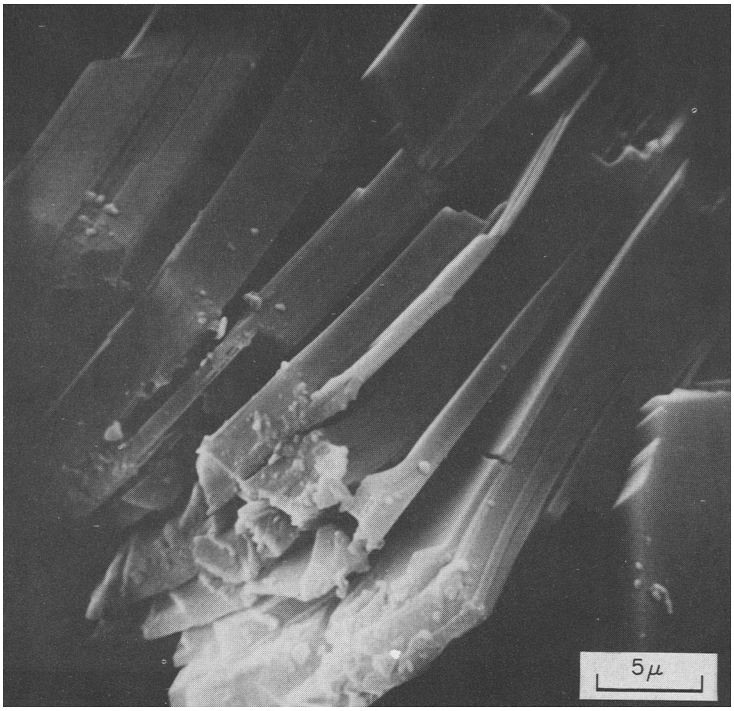

Fig. 3(a). Authigenic kaolinite from the interior of a claystone concretion in the Francis Creek Member (shale) of the Carbondale Formation, Grundy Co., Illinois (Pennsylvanian).

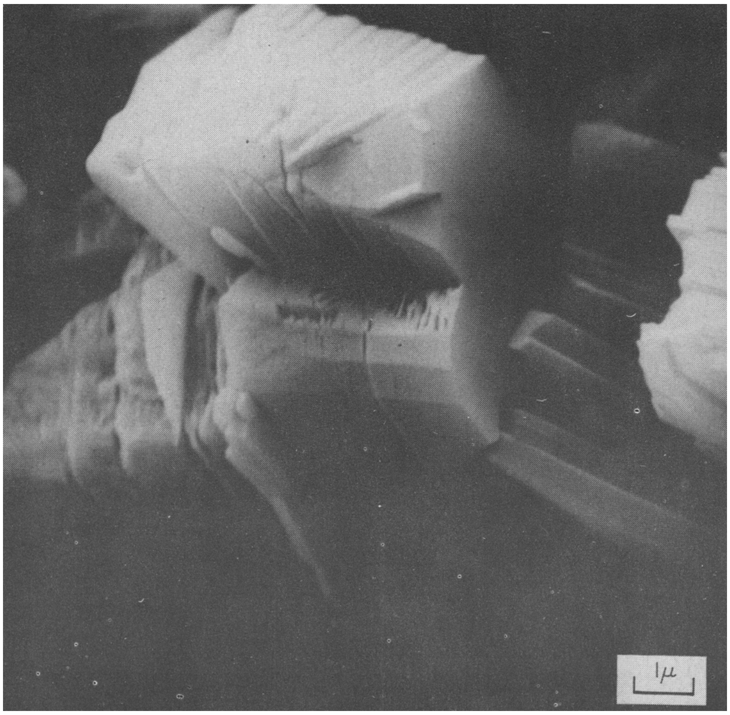

Fig. 3(b). Authigenic cleat kaolinite from the Herrin (No. 6) Coal Member, Carbondale Formation, Sangamon Co., Illinois (Pennsylvanian).

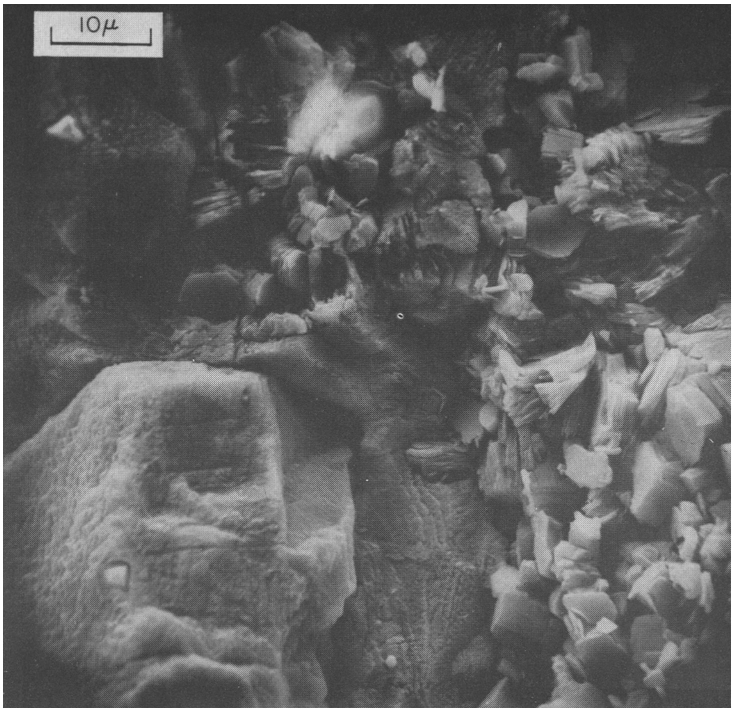

Fig. 4(a). Cross section of cleat containing kaolinite (right) and pyrite (left) from the Herrin (No. 6) Coal Member, Carbondale Formation, Sangamon Co., Illinois (Pennsylvanian).

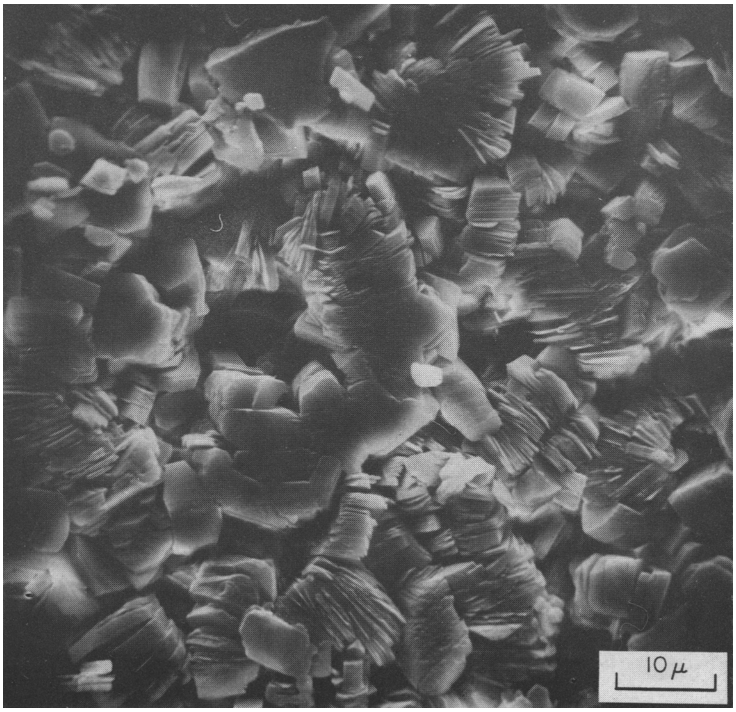

Fig. 4(b). Normal view of kaolinitic cleat surface; Herrin (No. 6) Coal Member, Sangamon Co., Illinois (Pennsylvanian).

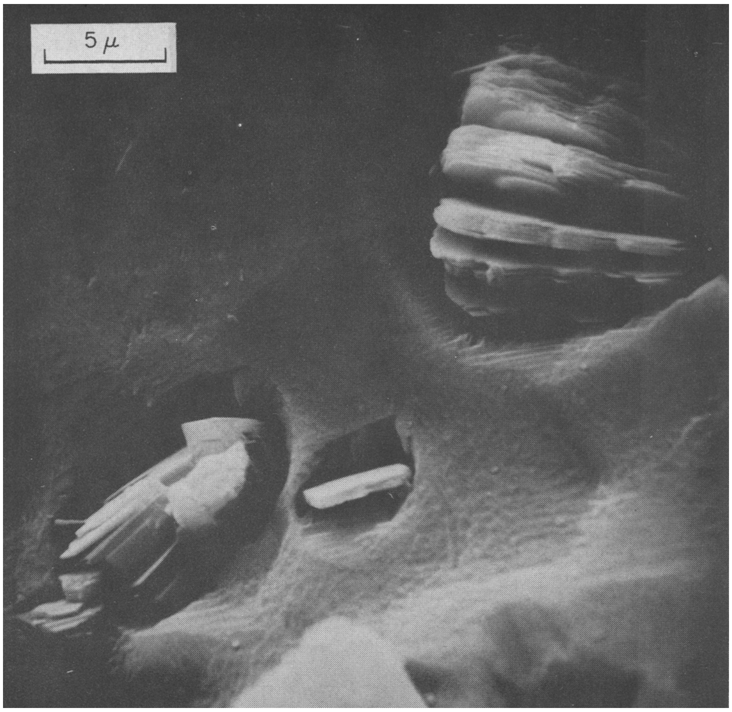

Fig. 5(a). Normal view of pyrite cleat surface with kaolinite packets growing through; Herrin (No. 6) Coal Member, Carbondale Formation, Sangamon Co., Illinois (Pennsylvanian).

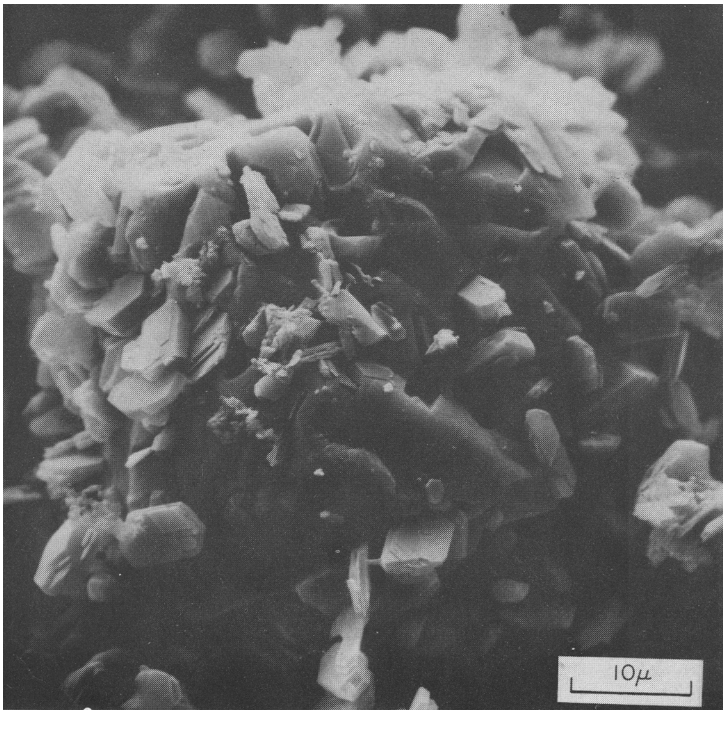

Fig. 5(b). Authigenic kaolinite growing in quartz crystal; geode from the Warsaw Formation, Hamilton Co., Illinois (Mississippian).

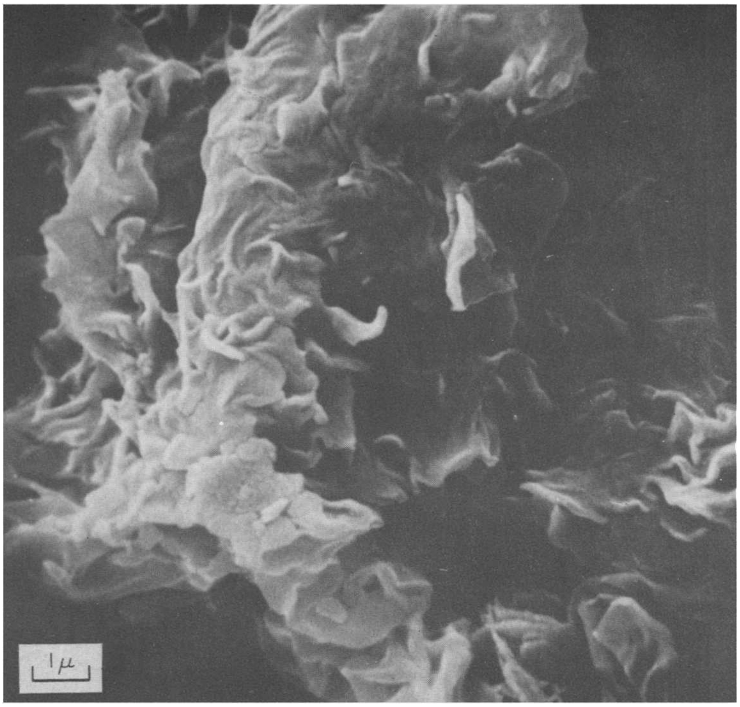

Fig. 6(a). Rock sample of bentonite from Clay Spur, Wyoming (A.P.I. No. 26) (Cretaceous).

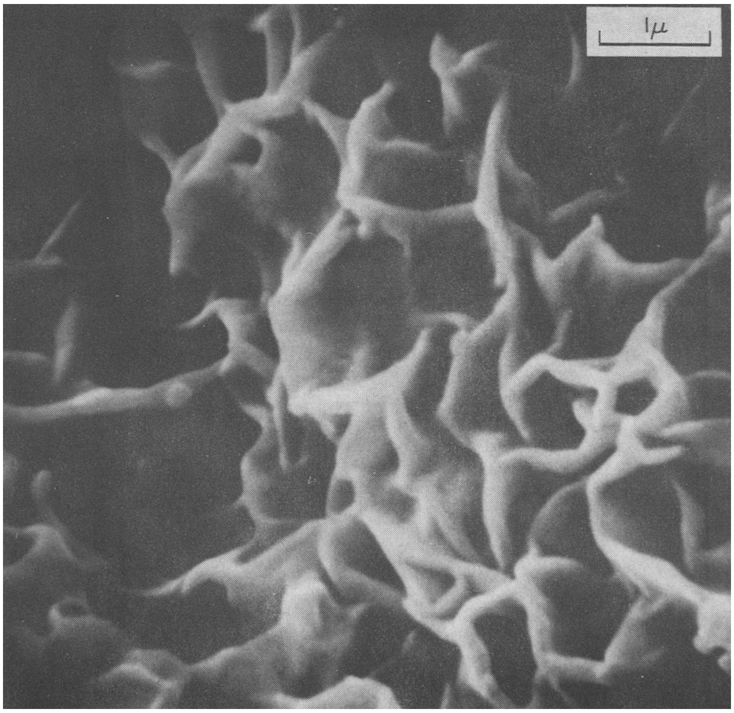

Fig. 6(b). Rock sample of Wyoming bentonite (A.P.I. No. 26).

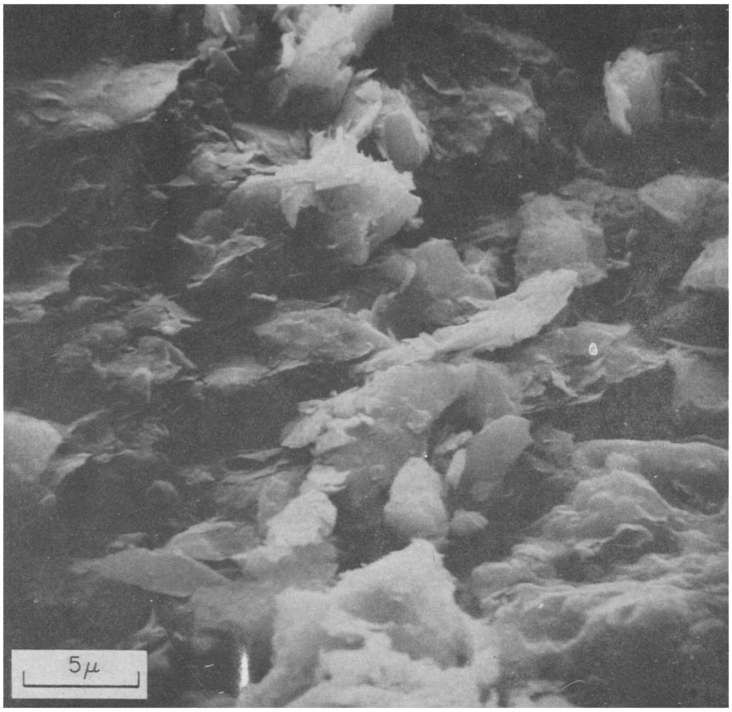

Fig. 7(a). Illitic clay from the "Blue Band," a clay seam (split) in the Herrin (No. 6) Coal Member, Carbondale Formation, Sangamon Co., Illinois (Pennsylvanian).

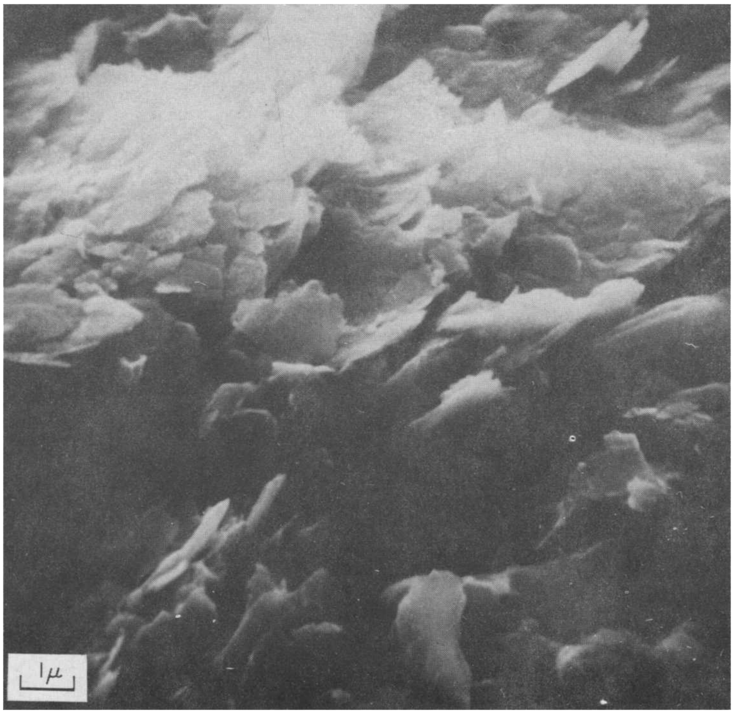

Fig. 7(b). Underclay from beneath the Colchester (No. 2) Coal Member, Carbondale Formation, Mercer Co., Illinois (Pennsylvanian).

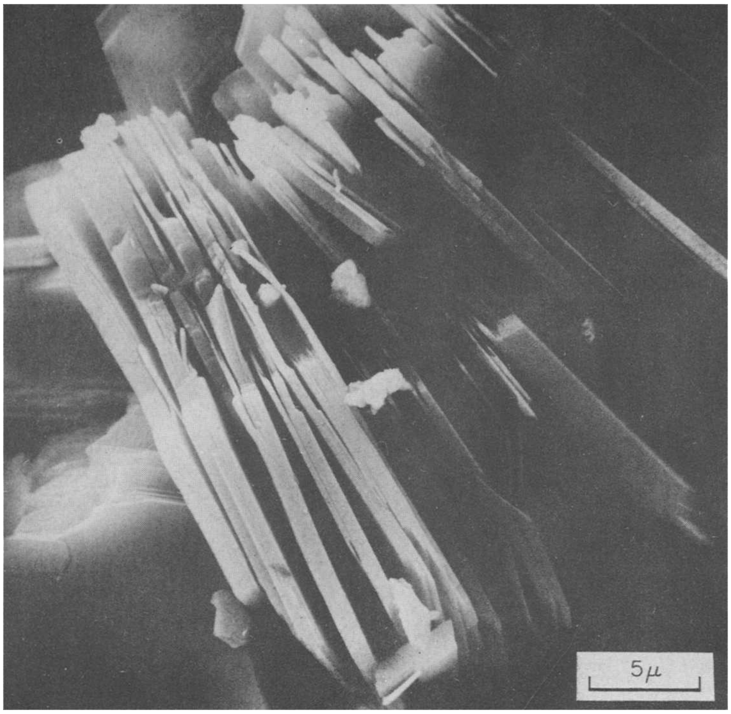

Fig. 8(a). Edge view of authigenic kaolinite packet; from concretion in the Francis Creek Member of the Carbondale Formation, Grundy Co., Illinois (Pennsylvanian).

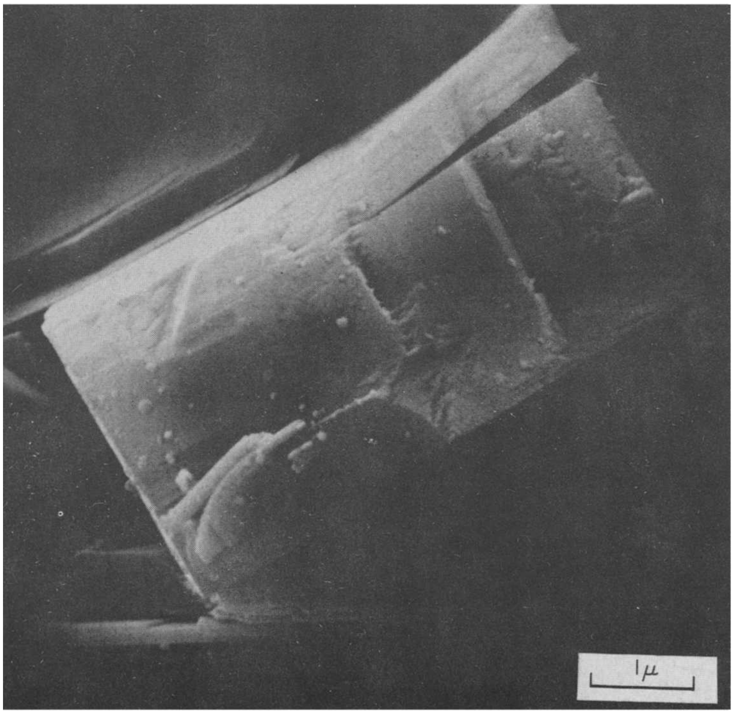

Fig. 8(b). Side view of thick, obscurely laminated packet of authigenic kaolinite from a concretion: Francis Creek Member, Carbondale Formation, Grundy Co., Illinois (Pennsylvanian).

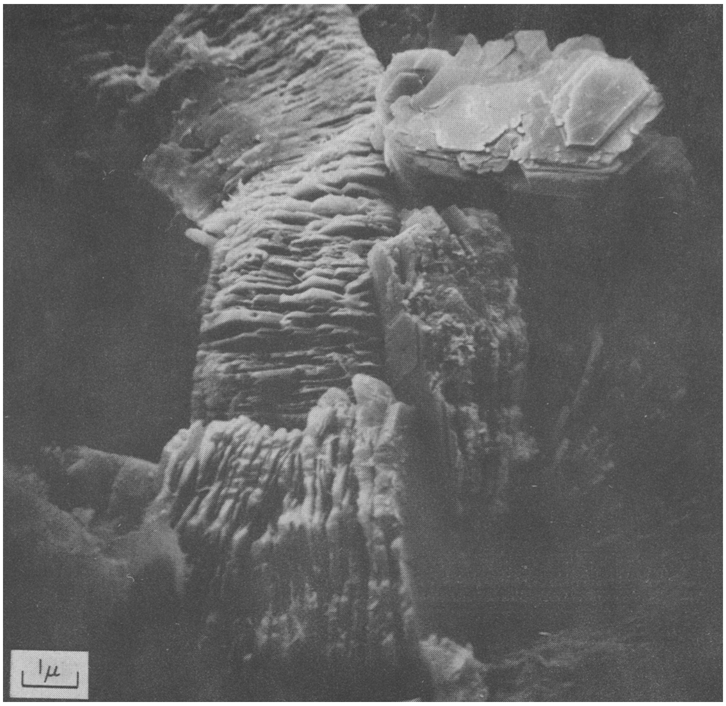

Fig. 9(a). Authigenic kaolinite vermicules in pores of a sandstone; St. Peter Formation, La Salle Co., Illinois (Ordovician).

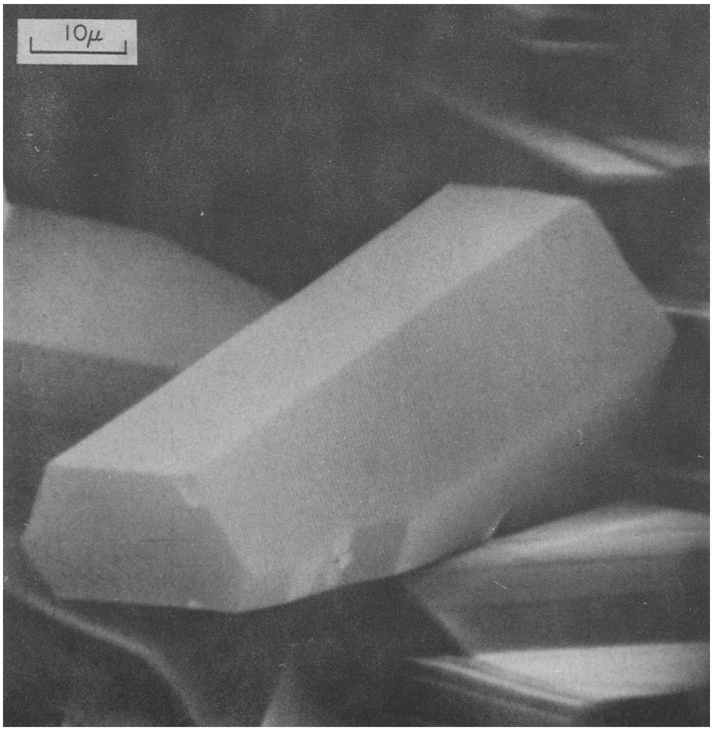

Fig. 9(b). Single crystal of dickite from a limestone in the Lansing-Kansas City Group, Wilson Co., Kansas (Pennsylvanian).

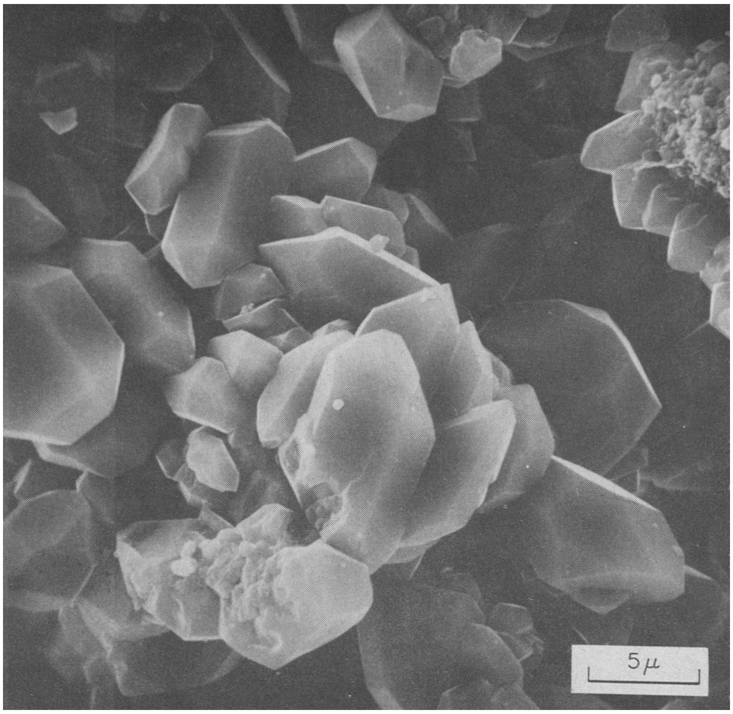

Fig. 10(a). Quartz microcrystals in a replaced fossil; Clear Creek Formation, Union Co., Illinois (Devonian).

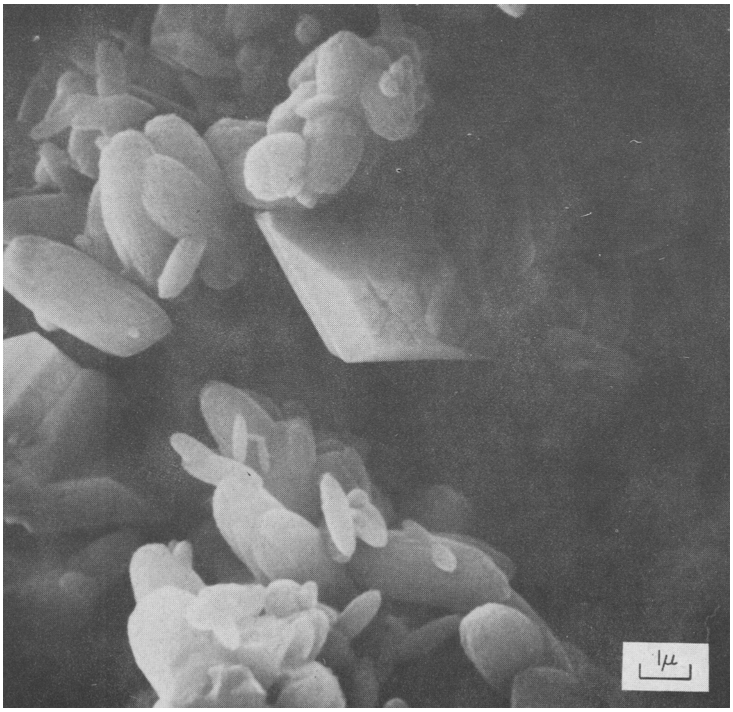

Fig. 10(b). Unusual crystalline phases in white bauxite from Montenegro, Yugoslavia.

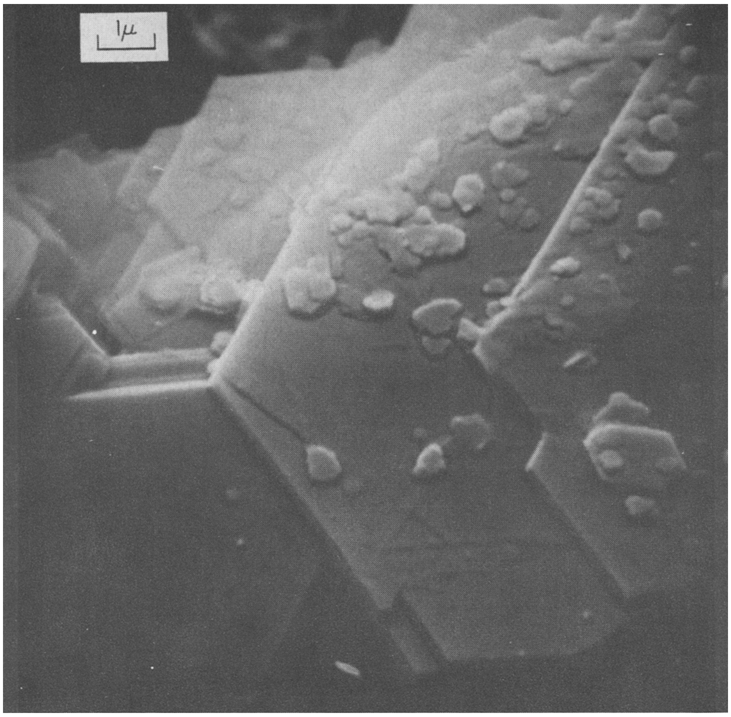

Fig. 11(a). Secondary illite laths on authigenic kaolinite plates: St. Peter Formation, La Salle Co., Illinois (Ordovician).

Fig. 11(b). Laths of kaolin mineral (probably halloysite) developing from weathering of feldspar crystal: Spruce Pine, North Carolina (A.P.I. No. 51).

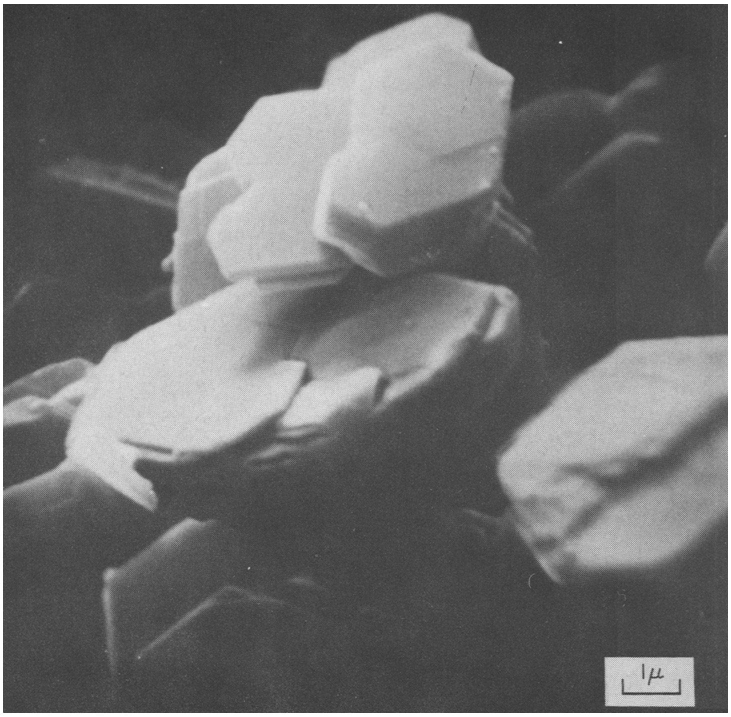

Fig. 12(a). Spiral growth and twinning of authigenic kaolinite from a geode; Warsaw Formation, Hamilton Co., Illinois (Mississippian).

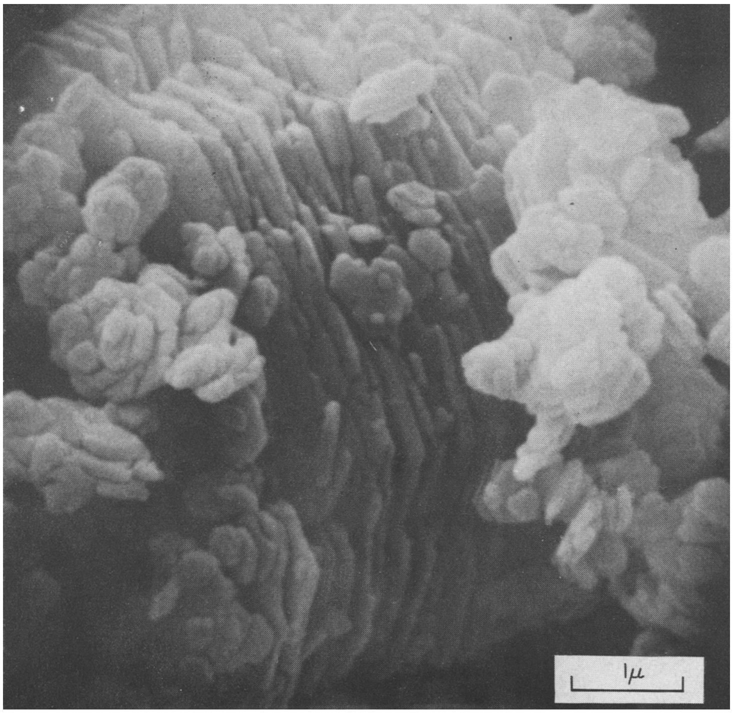

Fig. 12(b). Composite vermicule in kaolinite from Georgia (Eocene).

Fig. 13(a). Uniform vermicular stacks of dickite from Utah.

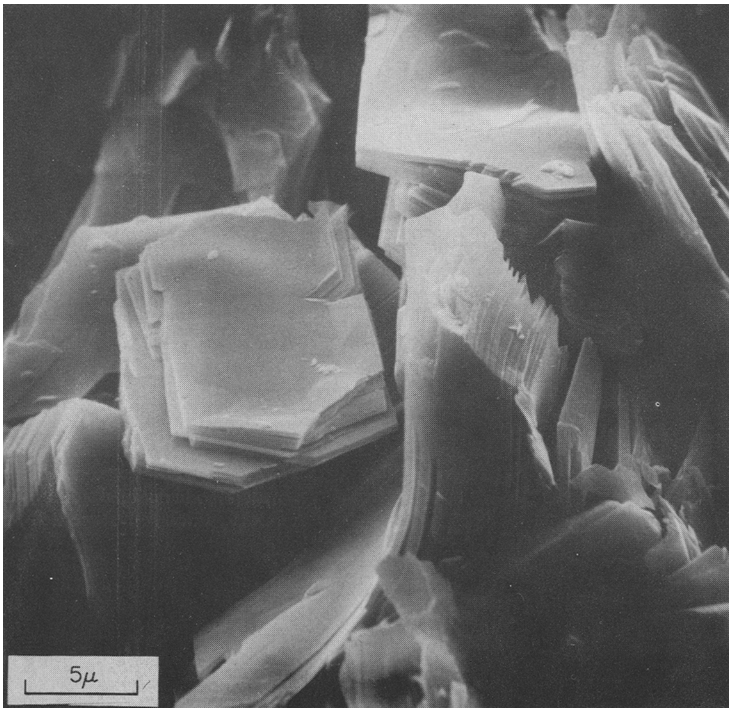

Fig. 13(b). Twinned and bent crystallites of dickite from Utah.

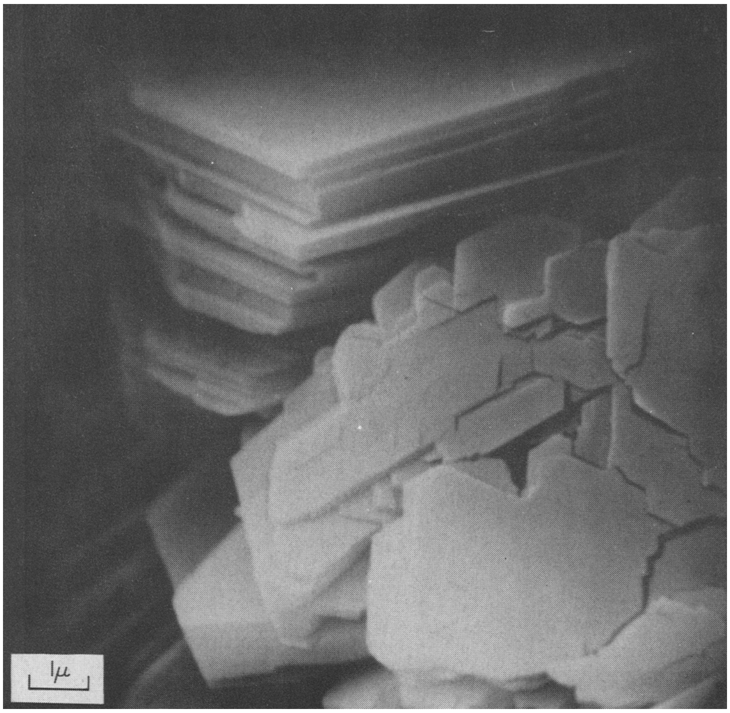

Fig. 14(a). Mosaic of small kaolinite crystals forming larger crystallites in cleat; Herrin (No. 6) Coal Member, Carbondale Formation, Sangamon Co., Illinois (Pennsylvanian).

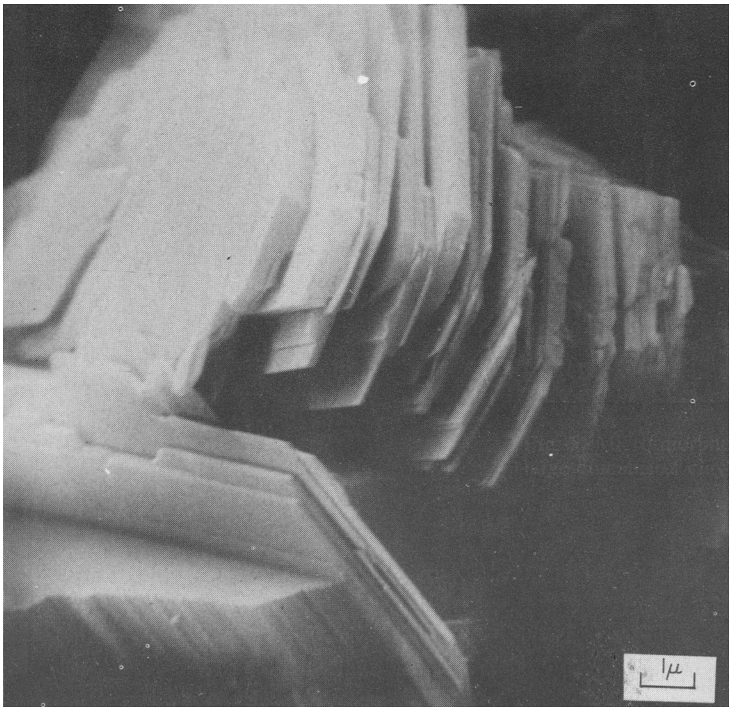

Fig. 14(b). Cantilevered stacking sequence of platelets in kaolinite stack; concretion in Francis Creek Member, Carbondale Formation, Grundy Co., Illinois (Pennsylvanian).

tangential arrangement of the clay mineral platelets around the circumference of the sphere. Obviously, the particles arranged themselves in this fashion because of the surface tension in the original suspension droplet formed by the nebulizer, and they retained this arrangement while the water was being driven off in transit through the drying tube.

Figure 2(a), a view of natural rock attapulgite from Mexico, is atypical in that its needle-like crysallites shown here are usually compacted into massive, featureless blocks. This micrograph does show the morphology of the crystallites quite well, however; notice the longitudinal bending of the thinner crystallites that have at least one free end, and the lath-like aggregate of crystallites extending upward from the surface in the center right portion of the micrograph. Apparently, fracturing during sample preparation disrupted and lifted a small area of the crystallite packets.

Figure 2(b) is the same Mexican attapulgite after ultrasonic dispersion and spray drying. The spherical aggregate with the typical "ball of yarn" appearance results from tangential adhesion of the attapulgite crystallites. The bundles of crystallites in the background are free powder or "dust" generated by aggregates too large to accrete tangentially to water droplets. This "dust" is a typical component of spray-dried powders, and its ratio to the spherical aggregates varies directly with the particle size of the sprayed material for any given range of droplet sizes (sprayer characteristics).

Attapulgite is a difficult mineral to prepare properly and examine in the SEM in its natural (rock) state because it is finely acicular and has a high water sorption capacity. An area such as a broken edge where the individual crystallites are exposed and noncontiguous is usually selected for viewing but, because of the extremely irregular nature of the surface at these points, a continuous metallic coating almost never exists and heavy charging develops. Also, when the electron beam is focused down to the high magnifications required to view these individual crystallites adequately, the concentrated heat of the beam drives some of the channel water out of the mineral, resulting in abrupt sample movements and contamination of the microscope. The magnitude of these problems is greatly reduced, however, when the sample is prepared by spray drying. The surfaces of the spheres are much smoother and more easily coated with the vaporized metal, and the crystallites arranged tangentially on the spherical surface are individually quite well displayed (Fig. 2b). Because much less material is exposed to the electron beam and the mounting foil acts as a heat sink, sample degassing (water expulsion) is almost eliminated and sample movement and microscope contamination are reduced.

Fabric

The SEM is unique in its ability to reveal interparticle relations, such as interlocking and interpenetration features, aggregate arrangement (face-to-face vs. edge-face) and shrinkage (drying) features. Figures 3(a) and (b) illustrate interlocking in authigenic kaolinites. Figure 3(a) shows the typical "stepped" appearance of this fabric feature in the lower right of the micrograph. The sample is kaolinite within a concretion. Figure 3(b) also shows interlocking and interpenetration of kaolinite layer packets at the right of the micrograph. This sample is cleat kaolinite (authigenic kaolinite forming along dessication or shrinkage cracks) from the vitrain layers in coal. The thick packet in the center of the micrograph displays evidence of twinning, as shown by the nonparallelism of the platelet edges along the upper surface of the crystal compared with the edges exposed at the middle of the micrograph. Similar interlocking of crystals and packets occurs in flint clay and partly accounts for its difficulty of dispersion, as well as that of cleat and concretion kaolinites.

Texture

On a larger scale, interlocking can occur where two types of materials grow into contact. Figure 4(a) is a cross section of the contact between pyrite on the left and kaolinite on the right in a cleat (vertical dessication crack or parting) filling in an Illinois coal. Pyrite often occurs between the coal surface and the main vein filling of kaolinite in cleats, and the irregular contact between these two shows the strong penetration of kaolinite into the pyrite. In contrast, Fig. 4(b) shows the surface of a kaolinite-filled cleat that originally was in direct contact with the coal with no intervening pyrite layer. The termination (sealing) of packets against the coal by both basal and prism surfaces is flat. The two micrographs clearly show why cleat kaolinite can be separated easily from coal, but only with difficulty from any associated pyrite.

Further evidence of intergrowth and penetration textures due to corrosion are shown by Figs. 5(a, b). Another instance of the growth of kaolinite packets through a cleat pyrite layer in a coal is shown in Fig. 5(a). The environment is the same as that in Fig. 4(a), but the view is now perpendicular to the extended cleat surface of the pyrite. The blocky, stepped texture of the pyrite can be seen clearly in this micrograph. Solutions that somewhat preceded deposition of the kaolinite seem to have produced holes in the pyrite layer by corrosive action in which the clay then grew. Some post-corrosion, prismatic pyrite crystals appear to have grown on the walls of these holes. Figure 5(b) reveals a slightly different intergrowth texture involving authigenic kaolinite and quartz formed in a geode. Here the quartz-kaolinite contacts are more sharply defined and more parallel, indicating a closer control on corrosion of the quartz by the later-forming kaolinite crystallites themselves.

Another aspect of texture is shown by the next two sets of figures (Figs. 6a, b, 7a, b). The first micrograph (Fig. 6a) shows the typical surface appearance of a clay largely composed of smectite – a bentonite from Wyoming. This crinkly, ridged, honeycomb-like texture (shown in a closer view in Fig. 6(b)) is characteristic of the smectite group and probably develops from shrinkage of the expandable clay minerals as they dry. The polygonal pattern of this texture resembles dessication mud cracks and other dewatering features. Individual crystal platelets are almost invisible in the smectites because they are small and dispersed, leaving an impression of cohesive thin films composing the basic textural units of these clays.

Between the filmy texture of the smectites and the aggregates of rather thick, stubby plates in the kaolinites (Fig. 1a), is the texture of illitic clays, such as that found in a shale split (the so-called "Blue Band") in an Illinois coal shown in Fig. 7(a). Several small ovoid pods, characteristic of illitic clay minerals found in some underclays, are shown on the left in the micrograph, along with the wavy surfaces of the clay flakes. The detrital illites are generally composed of thin anhedral plates and aggregates. Figure 7(b) shows an underclay from Illinois and again exhibits the typical claystone texture, plus some good examples of individual illite platelets, especially at the left in the micrograph.

Growth mechanics

Details of crystal growth mechanics in clays, such as layering (packet thicknesses), crystal habit, topotaxis, twinning, and spiral growth can be studied with the SEM if the clay mineral crystallites are large, well formed, and of a fairly open texture. Of all the clays we have studied, these criteria are best fulfilled by the authigenic kaolins, which provide most of our examples of these growth features. Authigenic kaolinites collected in Illinois include samples from a concretion, from the interstitial pores of a sandstone, and from the interior of a geode. One sample of a kaolinite from Georgia (courtesy of Georgia Kaolin Company) is also included. Other authigenic kaolin minerals included are samples of dickite from southeastern Kansas and Utah, an example of "halloysite" from North Carolina, and a white bauxite sample from Yugoslavia (courtesy of Professor Olga Sarc-Lahodny, University of Zagreb).

Packet thicknesses vary in authigenic kaolinite. Figures 8(a), (b) depict this variability in a sample of kaolinite from a concretion in a shale from Illinois. In Fig. 8(a), the side view of a stack shows a majority of relatively thin packets of nearly equal thickness. However, closer examination of these packets, especially along broken surfaces, reveals that they are composed of many thinner platelets. An accurate count of the number of platelets making up each packet cannot be made because of the limits imposed by the resolving power of the microscope. In contrast to these thin packets, Fig. 8(b) shows an extremely thick packet from this same concretion. A parting is beginning to develop in the upper quarter, and the lower third of the packet seems to be twinned, as no parallel lamellae edges are visible and the plates seem to meet the overlying packet with angular unconformity. There is probably some factor controlling the thickness of packets, but we have not yet identified it from these micrographs.

Examples of crystal forms and habits are shown in Figs. 9(a), (b), 10(a), (b). Authigenic kaolinite and dickite usually crystallize as stacks of packets, whose length (stacking on the (001) basal surfaces) sometimes exceeds their diameter by several orders. These are the familiar vermicules, or worms, of the tonsteins and other clays. Figure 9(a) shows vermicular kaolinite growing in pores of a sandstone from an outcrop in Illinois. Similar vermicular growth by extended basal stacking was displayed in the cleat sample (Fig. 5a). However, Figure 9(b) shows a crystal form of the kaolin group quite different from the usual stacked buildups of two-dimensional platelets. This unusual morphology was found in dickite from a limestone in southeastern Kansas. It is pseudohexagonal, which is compatible with the monoclinic nature of dickite. It is certainly not quartz, because of its crystal habit and its lack of basal pinacoids. When it is compared with the authigenic quartz crystals from southern Illinois in Fig. 10(a), the difference in crystal morphology is obvious. The tiny pseudohexagonal prism of Fig. 9(b) is apparently either an unusual crystallization of dickite or is some other form of hydrous alumina. As X-ray diffraction analysis showed only dickite, quartz, and calcite present in this sample, the unidentified mineral must be dickite. This case of questionable identity is an example of the potential value of a microprobe accessory, for the problem could have been solved in short order had such a unit been attached to our SEM.

Some other interesting crystal forms that might be found in high alumina clays are shown in Fig. 10(b), a sample of white bauxite from Yugoslavia. The rounded crystallites similar in appearance to grains of rice are probably boehmite, the major bauxite mineral in this sample, and the diamond-shaped crystal near the center may be prismatic gibbsite. These crystal habits are only rarely observed in this sample, the bulk being composed of massive, anhedral aluminates. The well formed crystals seemingly develop only in pores and other voids.

Some evidence for topotaxic clay mineral growth has been observed with the SEM. Figure 11(a) shows the surface of some well formed vermicules of authigenic kaolinite in a sandstone. Imposed on these planar surfaces are very thin, long laths, often overlying one another at 60° angles. These lath-like crystallites are interpreted as authigenic illite, possibly generated by a chemical groundwater reversal during the Pleistocene Epoch. The illite laths are secondary to the kaolinite, because several of the faint laths drape over the edge of one kaolinite platelet and continue onto the surface of the underlying platelet (right-hand side of the micrograph). Such topotaxic growth control (120° angles of growth) exercised by the pseudohexagonal kaolinite on secondary illite also was clearly shown by Rex (1966), and the reasons for it are adequately explained in his paper.

Figure 11(b) is "halloysite" from Spruce Pine, North Caroline. The micrograph shows a feldspar grain weathering to a lath-like kaolin mineral, probably halloysite. The lath-shaped, rod-like crystals forming on the surface of this grain are only tentatively identified as halloysite, however, because in none of the many micrographs made of this clay, nor in the SEM pictures of this same material in Borst and Keller (1969), have any true open-ended tubes been clearly recognized. The originally stubby halloysite crystal laths may elongate by secondary growth on the ends of the prisms (or tubes) to form the slender rods characteristic of the Spruce Pine kaolin. TEM replicate micrographs of this material (Taggart *et al.*, 1955) usually show scrolled or spatulate tubes, unlike the laths shown here.

Twinning and spiral growth are fairly common in the authigenic kaolins, but finding clearly defined examples is rather difficult. Figure 12(a) is a rarity because it displays both these growth phenomena. The crystal packet at the top of the picture is twinned on $hk0$ where $h = k$, probably the most common type of twinning in kaolinite. The larger packet in the center shows the spiral growth mode. This latter phenomenon results in pseudohexagonal crystals that share common interior edges and extend helically in the c-direction to form the larger crystallites of kaolinite vermicules. Figure 12(b) illustrates this composite growth of kaolinite vermicules very well in a sample of Georgia kaolinite. This micrograph is an oblique view of a large vermicule with serrated edges that result from the stacking of a large number of smaller, hexagonal platelets in columnar arrangement around a central axis. Similar serration or scalloping of vermicule edges can be seen in Figs. 5(a), 9(a). Serration seems to be characteristic of authigenic vermicular kaolinites. Authigenic dickite (Fig. 13a) does not usually show this serration. However, twinning is common in dickite, as is shown by the small crystals at the far right center of Fig. 13(a), and the lack of serration is probably due to a slightly different growth mode. Figure 13(b) shows a twinned crystal at the left center of the micrograph, with a large, bent sheaf of platelets just to the right and below it.

Further evidence of twinning, composite crystals, and spiral growth in authigenic kaolinite is given by Figs. 14(a), (b). The highly composite nature of large crystallites is shown by the grouping in the lower right of Fig. 14(a), a sample of cleat kaolinite from Illinois. In the concretion kaolinite of Fig. 14(b), interpenetration is exhibited at the lower left, while the stack of platelets in the upper center shows the "cantilever" structure that sometimes is caused by precession or eccentricity of the spiral growth axis. This cantilever effect is rather common in authigenic kaolinite and dickite.

SUMMARY AND CONCLUSIONS

The SEM has proved very useful for studying clay minerals. Its speed and ease of operation, high magnification, and great depth of focus make it uniquely suited to the study of very fine-grained materials and surfaces.

Past SEM work in clay mineralogy has been primarily concerned with the description of members of the various clay mineral groups. From our studies we conclude that the SEM is almost indispensable for the study of clay mineral configuration (size and shape), fabric (interpenetration), texture (intergrowth), and growth mechanics. In the latter category, such growth-related phenomena as layering, crystal habit, topotaxis, twinning, and spiral growth are clearly visible in samples of many of the larger, well crystallized clay minerals, such as the authigenic kaolinites.

Advances in technology should make the SEM even more useful for studying clay minerals. Particularly needed are increased resolution and built-in spectrographic (microprobe) capabilities.

Because we have clearly observed corrosive effects in nature, excellent information on the effects of artificial mechanical (abrasion) and artificial chemical (etching) treatments should be obtainable with the SEM. The high degree of form demonstrated for authigenic minerals in nature also suggests that further investigation of synthetic and artificial weathering products with the SEM would be profitable.

Acknowledgments—We thank the Center for Electron Microscopy at the University of Illinois for the use of their facilities. This project was partially supported by the National Air Pollution Control Administration, Consumer Protection and Environmental Health Service, United States Public Health Service, through Grant AP 00517.

REFERENCES

Advanced Metals Research Corporation (1969) AMR High Resolution Scanning Electron Microscope, Model 900: Advanced Metals Research Corporation, Burlington, Mass.

Bates, T. F. and Comer, J. J. (1955) Electron microscopy of clays: *Clays and Clay Minerals* **3**, 1–25.

Beutelspacher, H. and Van der Marel, H. W. (1968) *Atlas of Electron Microscopy of Clay Minerals and Their Admixtures—A Picture Atlas* 333 p. Elsevier, Amsterdam.

Borst, R. L. and Keller, W. D. (1969) Scanning electron micrographs of API reference clay minerals and other selected samples: *Proc. Intern. Clay Conf. Tokyo* Vol. I, 871–901. Israel University Press, Jerusalem.

Gillot, J. E. (1969) Study of the fabric of fine-grained sediments with the scanning electron microscope: *J. Sediment. Petrol.* **39**, 90–105.

Hughes, R. E. and Bohor, B. F. (1970) Random clay powders prepared by spray drying: *Am. Mineralogist* **55**, No. 9–10, 1780–1786.

Rex, R. W. (1966) Authigenic kaolinite and mica as evidence for phase equilibria at low temperatures: *Clays and Clay Minerals* **13**, 95–104.

Taggart, M. S., Jr., Milligan, W. O. and Studer, H. P. (1955) Electron micrographic studies of clays: *Clays and Clay Minerals* **3**, 31–64. [*NAS-NRC Publ. 395*]

White, W. A. (1958) Water sorption properties of homoionic clay minerals: *Ill. State Geol. Surv. Rept. Invest. 208.*

Résumé—La microscope électronique à balayage (SEM) prouve qu'il est parfaitement adapté à l'étude de la configuration, de la texture et de la structure des prélèvements argileux. La mécanique de croissance des unités cristallines—interpénétration et inter-verrouillage des cristallites, constitution de cristal, entrelacement, croissance hélicoïdale et topotaxie—est également révélée d'une manière unique par le SEM.

Les kaolins authigéniques forment l'ensemble des exemples à cause de leur cristallite de plus grande taille, de leur meilleure cristallinité et de la texture ouverte qui les rend plus appropriés que les autres types de minéraux argileux, à l'examen par SEM.

Kurzreferat—Es wird festgestellt, dass sich das Abtastelektronenmikroskop (SEM) ideal für die Untersuchung des Gefüges, der Textur und der Struktur von Tonproben eignet. Die Wachstummechanik der gegenseitigen Eindringung kristalliner Einheiten und die Verknüpfung von Kristalliten, Kristallhabitus, Verzwillingung, schraubenförmiges Wachstum und Topotaxis werden ebenfalls auf einzigartige Weise durch SEM zum Vorschein gebracht.

Authigene Kaoline stellen den Hauptanteil der Proben dar weil ihre bedeutendere Kristallitgrösse, ihre bessere Kristallinität und offene Textur sie der Prüfung durch das SEM besser zugänglich machen als die meisten anderen Arten von Tonmineralen.

Резюме — Показано, что сканирующая электронная микроскопия представляет собой идеальный метод для изучения конфигурации, текстуры и структурно-морфологических характеристик образцов глин. Механизм роста кристаллитов, характер их прорастаний и срастаний, габитус кристаллов, двойникование, спиральный рост и топотаксия — все это наилучшим образом выявляется методом сканирующей электронной микроскопии.

Основную массу изученных автором образцов составили аутигенные каолиниты, которые, благодаря большим размерам кристаллитов, более высокой степени кристалличности и ясновыраженной текстуре, являются гораздо более пригодными для изучения методом сканирующей электронной микроскопии, чем другие глинистые минералы.

Geologia Croatica | 62/3 | 201–206 | 5 Figs. | Zagreb 2009

Identification of biogenetic calcite and aragonite using SEM

Željka Žigovečki Gobac[1], Hrvoje Posilović[2] and Vladimir Bermanec[1]

[1]Department of Geology, Faculty of Science, University of Zagreb, Horvatovac 95, 10000 Zagreb, Croatia; (zeljkaz@geol.pmf.hr)

[2]Department of Geology, Faculty of Science, University of Zagreb, Horvatovac 102a, 10000 Zagreb, Croatia

doi: 10.4154/gc.2009.14

Geologia Croatica

ABSTRACT

Identification of calcite and aragonite is very important for studying different fossil or recent biomineralized skeletons. A problem occurs when scanning electron microscopy is used for studying calcite and aragonite present in the same part of skeleton. The same chemical composition of these two minerals produces the same contrast on SEM images. There are three possible ways to distinguish calcite and aragonite in such a mixture. (1) It is possible to recognize the crystal habits of these two minerals, if crystal faces are developed. (2) The geochemical difference can also be an important tool for distinguishing aragonite (containing large cations like Sr, Ba, or Pb) from calcite (containing small cations like Mg, Mn, Fe, Zn, or Ni). However, it is also possible that large cations remain in the calcite crystal structure after phase transformation from aragonite to calcite. (3) The third possibility for distinguishing calcite from aragonite is to use staining methods. Different staining methods used for SEM analyses have had varying degrees of success. SUZUKI et al. (1993) successfully used Meigen's staining method, but results provided by Feigl's staining method were unsatisfactory. The failure when using Feigl's staining method was caused by the erroneous application of the solutions.

Keywords: Calcite, aragonite, morphology, geochemical difference, Feigl's staining method, SEM

1. INTRODUCTION

Different methods have previously been used for distinguishing a variety of carbonate minerals at different scales – from hand specimens to thin sections and micro to nanoscale mixtures. Calcite and aragonite are the two most common polymorphs of calcium carbonate. They very often occur in mixtures within rocks and specially in different organism's carbonate skeletons – either recent or fossil ones.

Calcite $CaCO_3$ is a hexagonal mineral, point group $\bar{3}2/m$, space group $R\bar{3}c$, with a=4.9896(2) Å and c=17.0610(11) Å (ANTHONY et al., 2003).

The structure of calcite was determined by BRAGG (1914), redetermined by SASS et al. (1957) and refined by EFFENBERGER (1981). The customary way of describing the calcite structure is using sodium chloride structure as a starting point (BRAGG, 1937). If sodium chloride is set up so that a threefold axis is vertical and then compressed along the threefold axis until the edges which meet it make an angle of 101°55' with each other, and then sodium atoms are replaced by a calcium atoms, and chlorine atoms with CO_3 groups (BRAGG, 1937), the calcite crystal structure is obtained.

Aragonite, $CaCO_3$ is an orthorhombic mineral, point group $2/m\ 2/m\ 2/m$, space group *Pmcn*, with a=4.9611(4) Å, b=7.9672(6) Å and c=5.7407(4) Å (ANTHONY et al., 2003).

The crystal structure of aragonite is described as calcium atoms that lie approximately in the positions of a hexagonal close-packing lattice, deformed by compression along the hexagonal axis. In such an arrangement, each CO_3 group lies between six calcium atoms (BRAGG, 1937). Calcium atoms in calcite and those in aragonite are arranged in approximate cubic and hexagonal close packing, respectively. In each case CO_3 groups occupy a position between six calcium atoms, but there is a difference. In calcite, the CO_3 group is placed in a way that each oxygen touches two calcium atoms. In aragonite, each oxygen atom touches three calcium atoms (BRAGG, 1937).

This difference in the crystal structure causes not only the different X-ray diffraction patterns, but also the various solubilities of these two polymorphs, which enables the use of several staining methods.

The crystal habit of calcite is extremely variable and some of the most common habits are: prismatic, thin to thick tabular, rhombohedral, or scalenohedral (PALACHE et al., 1951; GOLDSCHMIDT, 1913b). Figures 1A and 1B show the most widespread crystal habits of calcite. Untwinned crystals of aragonite are very rare. If they occur, they are usually short to long prismatic, very often needle like (PALACHE et al., 1951, GOLDSCHMIDT, 1913a). Figure 1C shows the prismatic crystal habit of aragonite. Crystal structure and chemistry are not the only factors affecting morphology. The chemical and physical conditions prevailing during crystal growth could also modify crystal habit (SPEER, 1983). During biomineralization, orthorhombic carbonates (among them aragonite) are used by different creatures to form a variety of structures to support, house and protect themselves (SPEER, 1983). Unfortunately, organisms produce skeletons of carbonate minerals mostly with close packing crystals, so, crystal habit in most cases cannot be observed in biomineralized skeletons. The crystal structure of calcite allows a wide range of compositional variation and different solid solutions, which include many divalent cations (like Mn, Fe, Mg, Zn, Co, or Ni).

Aragonite forms solid solutions with strontianite, cerusite and witherite, so, the presence of large cations like Sr, Pb and Ba could be an indicator for distinguishing aragonite from calcite. This method is not completely accurate, because of the possible phase transformation from aragonite to calcite (ŠEBEČIĆ & SLOVENEC, 1990), after which large cations including Sr, Pb, or Ba could remain in the calcite structure. If a mineral grain contains small cations (Mg, Fe, Mn, Zn, Co, or Ni), it is surely crystallized as calcite.

Staining recipes and procedures as a useful tool for calcite-aragonite differentiation were used and tested by numerous authors (FEIGL & LEITMEIER, 1933; FRIEDMAN, 1959; AYAN, 1965; DICKSON, 1966). Solutions most widely considered and used as contrasting agents for the selective staining of calcite and aragonite in electron microscopy are Feigl's (SCHNEIDERMANN & SANDBERG, 1971; SUZUKI et al., 1993; KATO et al., 2003) and Meigen's stains (SUZUKI et al., 1993; KATO et al., 2003).

FEIGL & LEITMEIER (1933) described Feigl's staining test and its mechanism is based on the different crystal structures, i.e. dissolution rates of calcite and aragonite in water.

SCHNEIDERMANN & SANDBERG (1971) first described the use of Feigl's solution in discrimination between calcite and aragonite by scanning electron microscopy. SUZUKI et al. (1993) stained molluscan shells with Feigl's and Meigen's stains and compared results by SEM, BSE and EDS. They reported much better results with Meigen's solution, because using Feigl's staining method they "were unable to find a good, size-effect-free condition". The main disadvantage of Feigl's staining was the coarse granular appearance of the staining precipitate.

KATO et al. (2003) used both staining methods for the separation of calcite and aragonite for isotopic analyses.

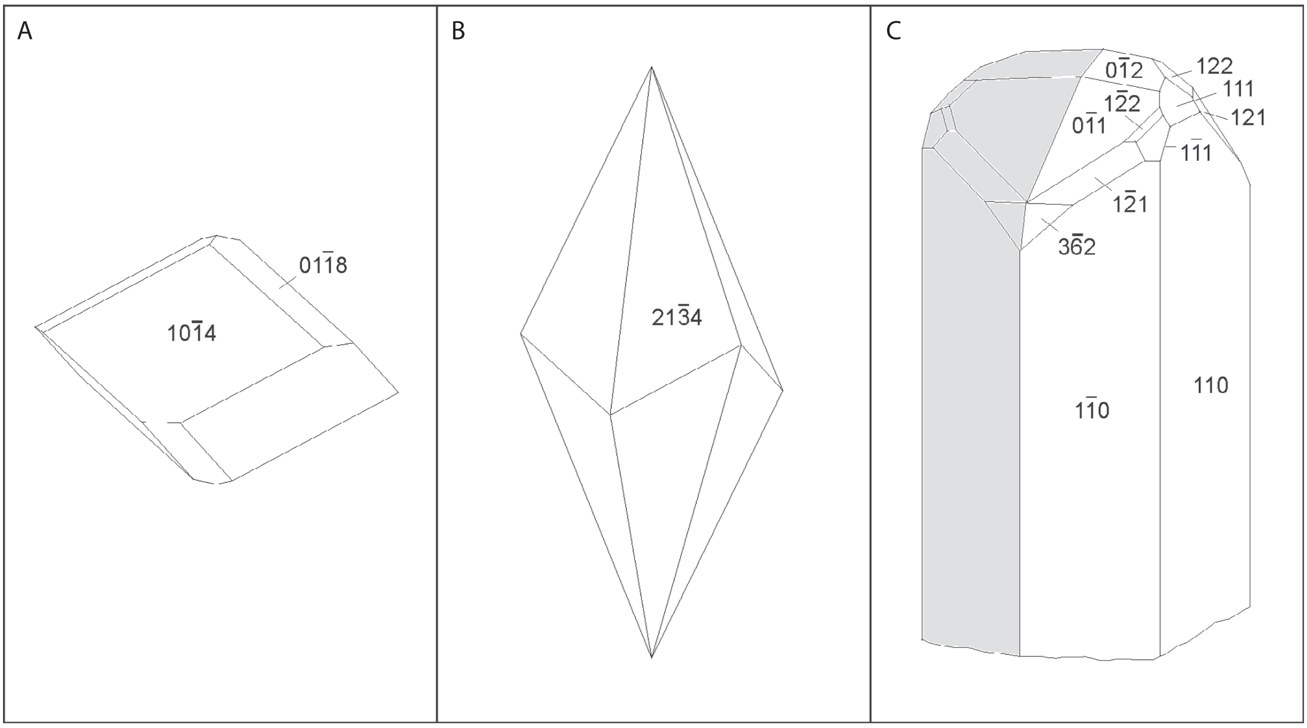

Figure 1: (A) Rhombohedral crystal habit of calcite. (B) Scalenohedral crystal habit of calcite. (C) Prismatic crystal habit of aragonite twins.

They concluded Meigen's solution was not effective for recrystallized or coarse-grained aragonites. Feigl's method was useful for such samples and investigations.

In this paper, in the description of the possible use of morphological observations, geochemical properties and Feigl's staining method are presented as useful tools for studying calcite and aragonite, separately or in mixtures, with scanning electron microscopy. Failure of the experiment described by SUZUKI et al. (1993) is the result of inconsistency in the solutions temperature, chemical composition and staining duration. Careful control of these parameters improves Feigl's staining method as a useful tool for identification of biogenetic calcite and aragonite using SEM.

2. MATERIALS AND METHODS

Two different groups of samples containing calcite and aragonite were studied. The first group consists of bryozoans *Pentapora* sp. skeletons from the Adriatic Sea, collected on Jabuka shoal from 40 to 50 m depth. A second group consists of white, sometimes macroscopically green stained sediment found around the hot well in Varaždinske toplice spa. This sediment precipitated from hot water, at least partially under the influence of some microorganisms.

Mineral phase determinations of the bulk samples were done using a Philips X'pert powder diffractometer, with CuKα radiation filtered with a graphite monochromator running at 40 kV and 40 mA. An X-ray diffraction data set was collected from 4 to 63°2θ.

Preparation of samples for SEM observations was not completely identical. Samples of bryozoans were first cleaned from their organic parts, and then fractured, finely ground, polished and mounted on the SEM stubs. They were not additionally etched prior to staining. Samples of hot well sediments were simply mounted on the SEM stubs. Both groups of sediments were then sputtered with carbon.

Morphological observations on the samples were carried out using a Tescan TS 5136 scanning electron microscope (SEM). For examination of the samples, the SEM was operating in back scattered (BSE) mode at an accelerating voltage of 20 kV and current of 10 mA. The same SEM microscope equipped with the Oxford energy dispersive spectrometer (EDS), coupled with INCA 250 system, was used for elemental distribution analysis in the samples. EDS qualitative analysis and elemental mapping was performed on the carbon coated samples at an accelerating voltage of 20 kV.

Morphological observations with SEM and elemental analysis with EDS on hot well sediment samples from Varaždinske toplice provided enough data to conclude the presence and relationship between calcite and aragonite. So, only the bryozoan samples were stained using Feigl's staining method.

The Feigl's staining method is based on the reduction of silver and manganese cations by hydroxyl anions released during aragonite dissolution, because aragonite is less stable than calcite; the solubility product of aragonite ($6.0 \cdot 10^{-9}$), represented by product of the concentration of ions (mol/dm^3) is larger than solubility product of calcite ($4.5 \cdot 10^{-9}$) (KRAUSKOPF, 1994).

The staining process could be described by the following equation (FEIGL, 1937):

Carbonate dissolution:

$$CaCO_3 + 2H_2O \leftrightarrow Ca^{2+} + H_2CO_3 + 2OH^-$$

Reaction of the cations with hydroxyl anions:

$$Mn^{2+} + 2Ag^+ + 4OH^- \leftrightarrow MnO_2 + 2Ag^\circ + 2H_2O$$

The result is precipitation of manganese dioxide and metallic silver on the carbonate surface, where the maximal concentration of hydroxyl groups lies. The precipitate is black in colour observed by naked eye or using a binocular microscope, (because both colloidal silver and manganese oxide are black), contrasting generally with white calcite and aragonite.

The solution is prepared according to the original recipe (FEIGL & LEITMEIER, 1933). 1 g Ag_2SO_4 is added to a solution of 11.8 g $MnSO_4 \cdot 7H_2O$ and 100 ml distilled water. The mixture is boiled, cooled and filtered. It is very important to neutralize the mixture with dilute sodium hydroxide until a black precipitate starts to form. After neutralization, the solution must be re-filtered and kept in a dark bottle.

Samples of bryozans *Pentapora* sp. were not stained over a set period of time, but until formation of the first light colouration. Aragonite surface colour changed from white to grayish over one to three minutes; more prolonged staining resulted in a completely black aragonite surface.

It is very important to control the complete staining process under the binocular light microscope. During staining, the solution was at room temperature.

3. RESULTS

X-ray powder diffraction patterns proved that both the carbonate shell of the bryozoan *Pentapora* sp. (Fig. 2A) and hot well sediment from Varaždinske toplice (Fig. 2B) are composed of a mixture of aragonite and calcite.

Using the SEM equipped with back scattered electron detector it was possible to recognize both calcite and aragonite crystals (Fig. 3A) on the samples from Varaždinske toplice. Recognition was based on their crystal habits.

Using of EDS allow confirmation of calcite crystal(s) or its agglomerations (Fig. 3B) and aragonite (Fig. 3C), because calcite contains a small but important and recognizable amount of Mg, and aragonite contains a small but important and recognizable amount of Sr. Small amount of S precipitates together with calcite and aragonite in the natural environment of the hot wells.

Morphological observations on the bryozoan samples were not so successful, because the crystal habit of skeleton-bearing carbonate minerals could not be observed, due to close packing of the crystals. EDS qualitative analysis and elemental mapping show that Mg is present in the inner part of a shell. Bryozoan *Pentapora* sp. samples were then stained using Feigl's staining method.

Cross sections of bryozoan *Pentapora* sp. samples showed differential staining indicating a bimineral skeletal composition (Fig. 4).

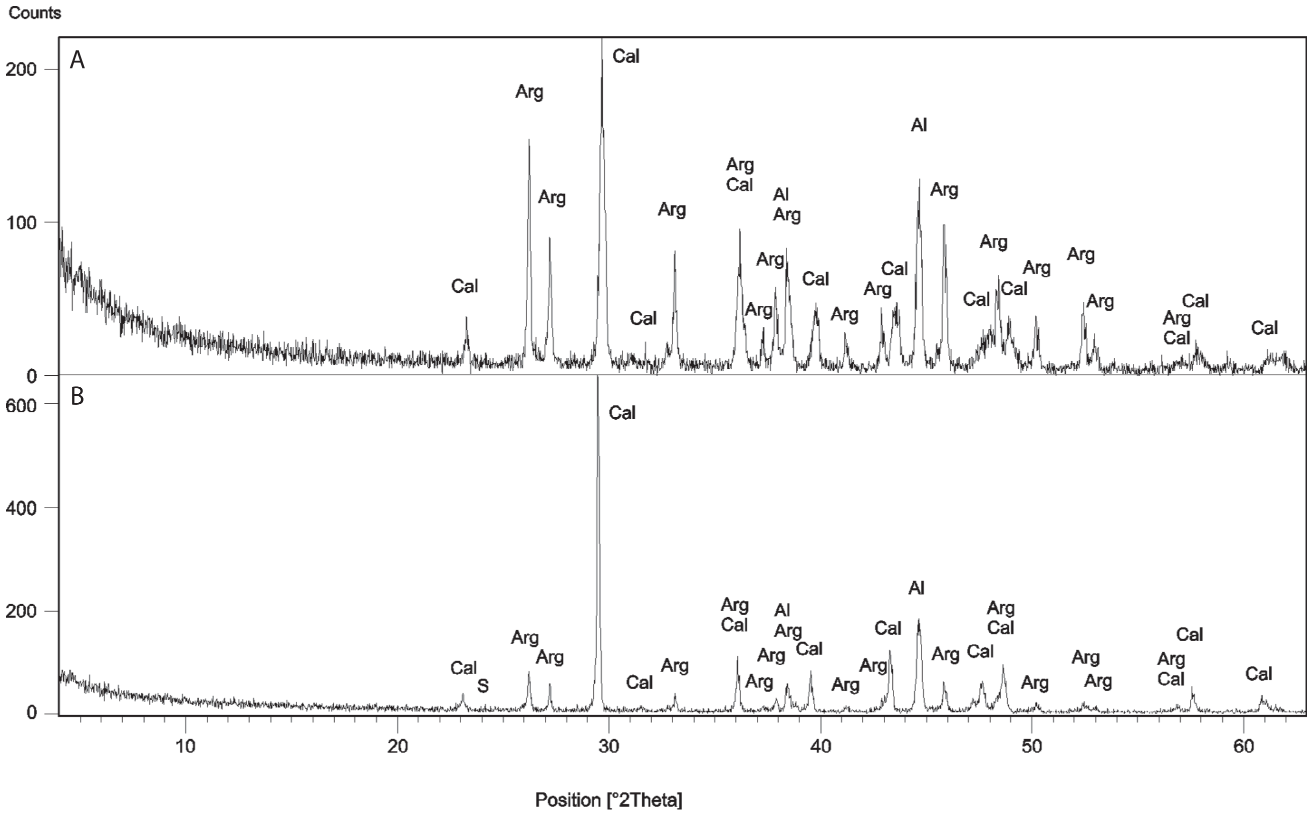

Figure 2: (A) XRD pattern of the sample *Pentapora* sp.; (B) XRD pattern of the sample from Varaždinske toplice; both showing a mixture of calcite and aragonite. Cal – calcite, Arg – aragonite, S – traces of coprecipitated sulfur, Al – aluminum from the sample holder.

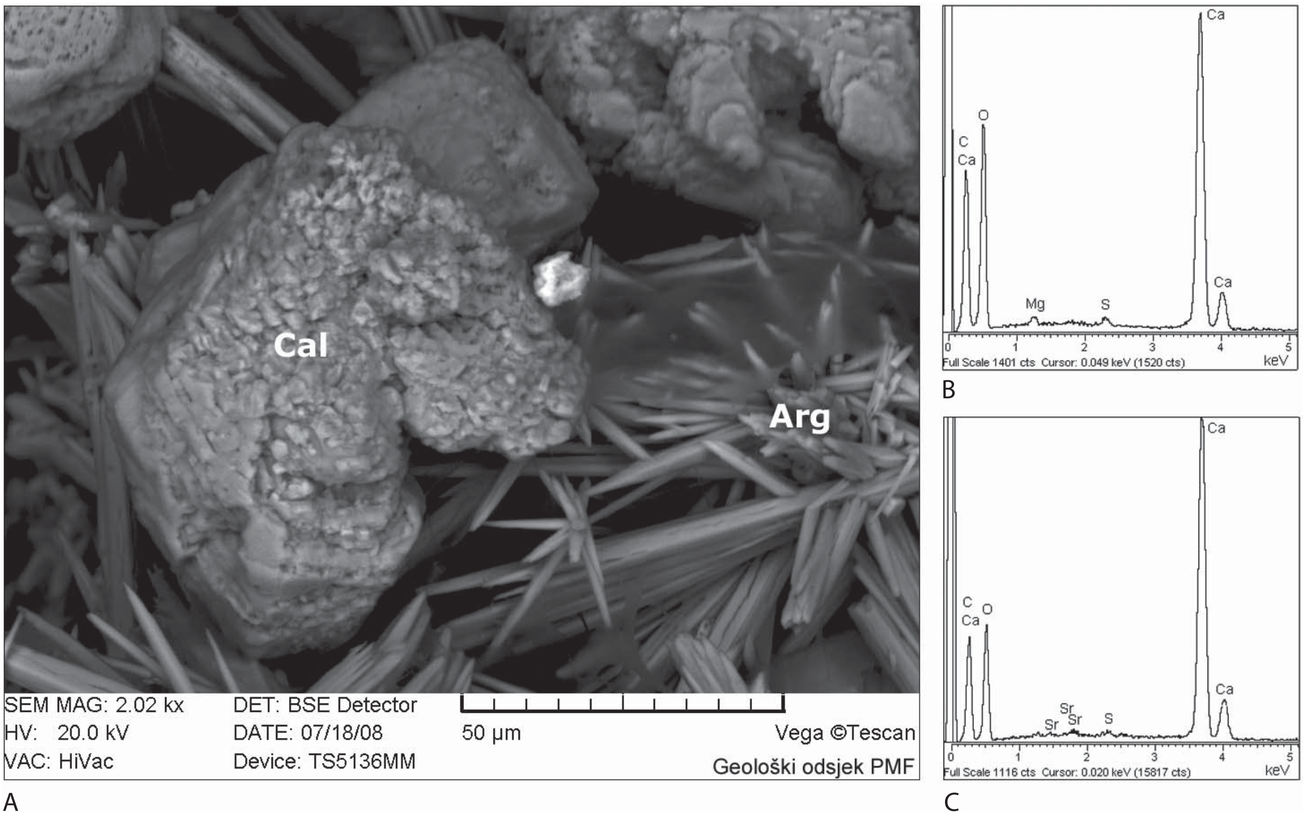

Figure 3: (A) Typical mixture of calcite and aragonite developed around the hot water well, in Varaždinske toplice under extreme conditions for living microbial organisms. Cal – rhombohedral crystals of calcite, Arg – sharp, needle like, crystals of aragonite. (B) EDS spectrum of calcite with minor content of Mg. (C) EDS spectrum of aragonite with increased content of Sr. Small, but measurable amount of sulfur also precipitate on the surface of these carbonates.

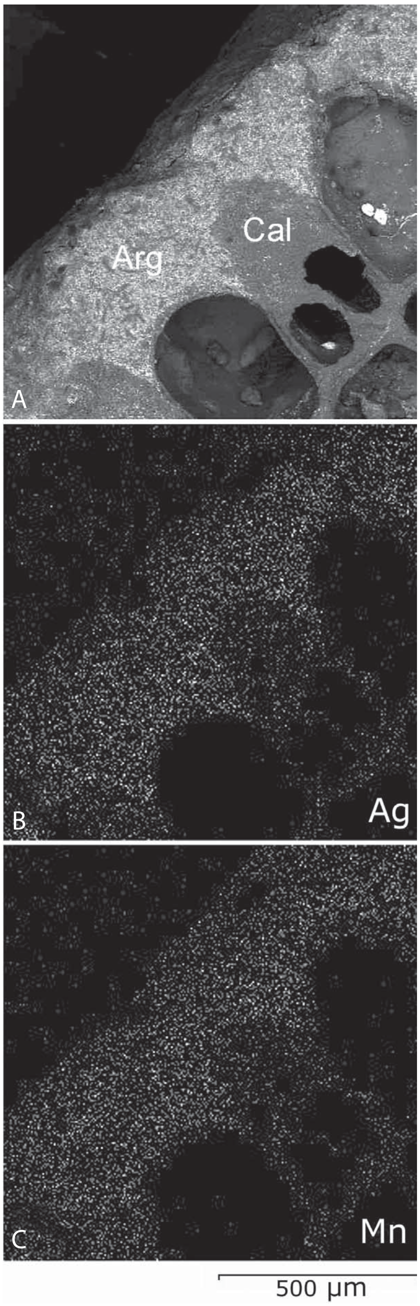

Figure 4: (A) SEM BSE image of the stained cross section of bryozoan *Pentapora* sp. with aragonite in the outer part and calcite inside the carbonate shell. Such images highlight the fine texture (smaller than a few tens of a micrometre), of the calcite and aragonite mixture of the outer shell. (B) Map of Ag. (C) Map of Mn. There is no significant difference between silver and manganese oxide deposition on the smooth aragonite surface.

Stained aragonite areas are covered with nanogranular manganese and silver precipitates, which do not completely cover the bryozoan microstructure, allowing very detailed examination. The calcite part of the shell was almost without any cover.

The black stain is easily recognizable macroscopically and under binocular light microscope, but is also easily recognizable using back scattered electron detector (BSE), because bright surfaces, rich in silver and manganese, on images indicate aragonite. Using light microscope allow to recognize presence of aragonite and/or calcite, but using of electron microscope it is possible to recognize the fine textures, for example the structure of outer bryozoan shell on the SEM BSE image. Mapping of such stained areas shows that there is colloidal silver and manganese oxide deposited homogeneously on aragonite (Fig. 4).

4. DISCUSSION

Many shells or skeletons have a bimineral composition. The ratio of calcite and aragonite could be determined by X-ray investigation (ANDERLE et al., 1998).

Such organisms usually have an aragonite inner and calcite outer layer of the shells. However, this could also be the opposite way around. It is not possible to recognize this arrangement using X-ray diffraction, except if it is combined by careful and sometime impossible separation. Nevertheless, it is possible to stain the sample by Feigl's solution. Using Feigl's staining method in combination with SEM BSE observation provides the opportunity to recognize not just aragonite distribution inside the shell wall, but also any fine textures.

The rates of dissolution of calcite and aragonite in the Feigl's solution control the intensity of manganese dioxide and metal silver precipitation and the size of deposited particles on the crystal surfaces. Aragonite dissolves more rapidly in the staining solution and will be stained by silver and manganese oxide, while calcite reacts slower and remains unstained.

The speed of carbonate dissolution and staining is altered if the staining solution concentration or temperature is changed. However, the speed of dissolution also depends on carbonate crystal size. Dissolution speed decreases with increasing size of the mineral grains. The rate of dissolution also varies with the crystal orientation, because of anisotropy.

Improper use of Feigl's method (e.g. too fast or too slow dissolution) produces coarse grains of metal (Ag and MnO_2)

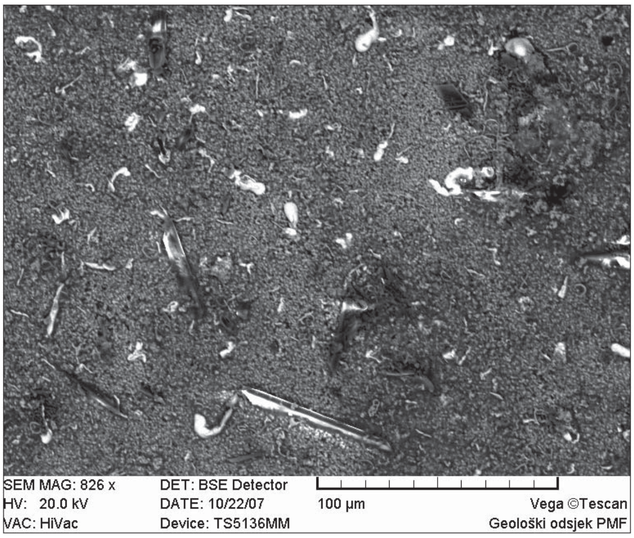

Figure 5: SEM BSE image of the manganese-oxide and metal silver precipitate on the aragonite surface of *Pentapora* sp. The precipitate is very coarse (up to 100 µm long) because of rapid aragonite dissolution in the very acidic Feigl's solution. Such preparation is inadequate for the microstructural observation of aragonite microstructures. White fragments are silver particles and gray particles are manganese oxide.

up to a few µm in size. The grains of silver and manganese oxide are too big for observing fine texture and cover both minerals – aragonite as well as calcite. This will happen when the solution is too acid and the procedure is too rapid. Such conditions caused failure of the method in the case of SUZUKI et al. (1993). If the pH is too low, dissolution of both calcite and aragonite produce an inconsistent and inadequate stain, as can be seen in Fig. 5.

Meigen's solution containing HCl acts more aggressively on aragonite dissolution than Feigl's stain. This means that Feigl's staining method allows preservation of more of the delicate mineral features of the bryozoan mineral textures (up to 10 µm). If the staining procedure is carried out carefully, with binocular light microscope control, it is possible to obtain a black manganese oxide and silver precipitate of nanometer size. If Feigl's solution is not neutralized properly, biogenetic carbonates will be corroded on the surface and this process will be easily visible using SEM BSE. So, SUZUKI et al., (1993) dismissed Feigl's staining method without any reason and favoured the less successful Meigen method.

5. CONCLUSION

Identification of aragonite and calcite is very simple by X-ray diffraction methods. But, it is not possible to describe the textural distribution of these carbonates using such methods.

The first and most logical aragonite-calcite differentiation by SEM BSE is on the basis of crystal morphology. Biogenetic carbonates, i.e. those mostly precipitated under microbial control, could sometimes be recognized (Fig. 3A). However, in most of the biomineralized skeletal structures, the typical crystal morphology is not developed.

Discrimination of two carbonate phases could be based on the large and small cation (usually strontium and magnesium) content of aragonite and calcite respectively, determined by EDS if these elements are present (Figs. 3B, 3C).

If none of the above-mentioned methods could be applied, staining methods alone will be useful. Staining with Feigl's solution can be successfully used for observations in mixtures in biogenetic carbonates using SEM BSE examination. Feigl's solution cannot be used as a standard procedure with fixed staining time or prescribed solution temperature. Because of this, binocular light microscope control is necessary. The difference in crystal structure of aragonite and calcite produces varying dissolution rates and without carefully monitored staining procedure, they will show inconsistent results or a coarse precipitate.

ACKNOWLEDGEMENT

This work was supported by the Ministry of Science, Education and Sports of the Republic of Croatia, under Grants no. 119-0000000-1158, 119-1191152-1169 and 098-0982934-2742.

REFERENCES

ANDERLE, H., STEFFAN, I., WILD, E., HILLE, P., BERMANEC, V. & SÖVERGJARTO, F. (1998): Detection and dosimetry of irradiated biominerals with thermoluminiscence, radioluminiscence and electron spin resonance measurements: comparison of methods.– Radiat. Meas., 29/5, 531–551. doi: 10.1016/S1350-4487(98)00038-9

ANTHONY, J.W., BIDEAUX, R.A., BLADH, K.W. & NICHOLS, M. C. (2003): Handbook of Mineralogy – Vol. 5 – Borates, Carbonates, Sulfates.– Mineral Data Publishing, Tucson, Arizona, 813 p.

AYAN, T. (1965): Chemical staining methods used in the identification of carbonate minerals.– B. Miner. Res. Expl., 65, 133–147.

BRAGG, W.L. (1914): The analysis of crystals by the X-ray spectrometer.– Proc. R. Soc. Lon. Ser.-A, 89, 468–489. doi:10.1098/rspa.1914.0015

BRAGG, W.L. (1937): Atomic structure of minerals.– Cornell University Press, London, 292 p.

DICKSON, J.A.D. (1966): Carbonate identification and genesis as revealed by staining.– J. Sediment. Petrol., 36/2, 491–505.

EFFENBERGER, H., MEREITER, K. & ZEMANN, J. (1981): Crystal structure refinements of magnesite, calcite, rhodochrosite, siderite, smithsonite and dolomite, with discussion of some aspects of the stereochemistry of calcite-type carbonates.– Z. Kristallogr., 156, 233–243.

FEIGL, F. (1937): Quantitative analysis by spot test.– Nordemann Publishing Company, New York, 400 p.

FEIGL, F. & LEITMEIER, H. (1933): "Spot" Test to Distinguish Calcite and Aragonite.– Microchem., 13, 136–138.

FRIEDMAN, G.M. (1959): Identification of Carbonate Minerals by Staining Methods.– J. Sediment. Res., 29/1, 87–97. doi: 10.1306/74D70894-2B21-11D7-8648000102C1865D

GOLDSCHMIDT, V. (1913a): Atlas der Kristallformen – Band I.– Winter, Heidelberg, 244 p.

GOLDSCHMIDT, V. (1913b): Atlas der Kristallformen – Band II.– Winter, Heidelberg, 251 p.

KATO, K., WADA, H. & FUJIOKA, K. (2003): The application of chemical staining to separate calcite and aragonite minerals for micro-scale isotopic analyses.– Geochem. J., 37, 291–297. doi: 14039.35400011830925.0100

KRAUSKOPF, B.K. (1994): Introduction to geochemistry.– McGraw-Hill, Inc. New York, 640 p.

PALACHE, C., BERMAN, H. & FRONDEL, C. (1951): The system of mineralogy of James Dwight Dana and Edward Salisbury Dana, 7th edition – Vol. 2. – Halides, nitrates, borates, carbonates, sulfates, phosphates, arsenates, tungstates, molibdates, etc.– John Wiley and Sons, New York, 1124 p.

SASS, R.L., VIDALE, R. & DONOHUE, J. (1957): Interatomic distances and thermal anisotropy in sodium nitrate and calcite.– Acta Crystallogr., 10, 567–570. doi:10.1107/S0365110X57002029

SPEER, J.A. (1983): Crystal chemistry and phase relations of orthorhombic carbonates.– In: REEDER, R.J. (ed.): Carbonates: mineralogy and chemistry. Rev. Mineral. Geochem., Mineral. Soc. America, Washington, 145–190.

SCHNEIDERMANN, N. & SANDBERG, P.A. (1971): Calcite-aragonite differentiation by selective staining and scanning electron microscopy.– Trans. Gulf Coast Assoc. Geol. Soc., 21, 349–351. doi: 10.1306/A1ADF466-0DFE-11D7-8641000102C1865D

SUZUKI, S., TAGO, Y. & HIKIDA, Y. (1993): Using Meigen's staining for aragonite-calcite identification in fossil molluscan shells under the scanning electron microscope.– J. Geol. Soc. Japan, 99, 1–7.

ŠEBEČIĆ, B. & SLOVENEC, D. (1990): Aragonite in Kerogenous Lower Cretaceous Carbonate Rocks of Mt. Dinara.– Geol. vjesnik, 43, 91–95.

Manuscript received June 02, 2009
Revised manuscript accepted September 18, 2009
Available online October 30, 2009

16 Atlas of Zircon Textures

Fernando Corfu

Institute of Geology, University of Oslo
P B 1047 Blindern
N-0316 Oslo, Norway

John M. Hanchar

Department of Earth and Environmental Sciences
The George Washington University
Washington, D.C. 20006

Paul W.O. Hoskin

Institut für Mineralogie, Petrologie und Geochemie
Albert-Ludwigs-Universität Freiburg
D-79104 Freiburg, Germany

Peter Kinny

Department of Applied Geology
Curtin University of Technology
Perth WA 6845, Australia

INTRODUCTION

The mineral zircon is extremely variable both in terms of external morphology and internal textures. These features reflect the geologic history of the mineral, especially the relevant episode(s) of magmatic or metamorphic crystallization (and recrystallization), strain imposed both by external forces and by internal volume expansion caused by metamictization, and chemical alteration. The paper presents a selection of both the most typical, but also of the less common, features seen in zircon, categorized according to the different geological processes responsible for their formation. The atlas is intended as a general guide for the interpretation of zircon characteristics, and of related isotopic data.

Zircon has become one of the most widely used minerals for the extraction of information on the prehistory and genesis of magmatic, metamorphic and sedimentary rocks. Much of the geological usefulness of zircon stems from its suitability as a geochronometer based on the decay of U (and Th) to Pb, but in addition it is also the major host of the radiogenic isotopic tracer Hf, and it is used to determine oxygen isotopic compositions and REE and other trace element abundances, all of which yield useful clues concerning the history of the host rock, and in some case, the parent rock in which the precursor zircon crystallized.

One of the major advantages of zircon is its ability to survive magmatic, metamorphic and erosional processes that destroy most other common minerals. Zircon-forming events tend to be preserved as distinct structural entities on a pre-existing zircon grain. Because of this ability, quite commonly zircon consists of distinct segments, each preserving a particular period of zircon-formation (or consumption). A long experience and modern instrumentation and techniques have provided the "zircon community" the means to image and interpret preserved textures, and hence to decipher the history and evolution of a rock. One of the most critical tasks is the proper assignment of particular zircon domains or grains to a specific stage in the history of a rock. This is relatively simple and straightforward in many cases where a proper understanding of the geological setting, simple logical deduction, and common sense lead to unambiguous and straightforward interpreta-

1529-6466/03/0053-0016$05.00

tions, but it can be an extremely difficult task in other cases where the interpretation may be affected more strongly by the bias of the investigator than by purely objective criteria. This is sometimes the case in complex gneiss terranes, as exemplified by the recent debate on the history of the Early Archean gneisses in Greenland (e.g., Nutman et al. 1993, 2002; Whitehouse et al. 1999, Myers and Crowley 2000). The interpretation of age and isotopic relations is affected, on the one hand, by the particular megascopic and petrologic relationships of a rock unit and, on the other hand, by the characteristics of the minerals analyzed, most commonly the external and internal characteristics of the accessory mineral zircon.

The intent of this chapter is to provide an overview of the variety of textural relations observed in zircon and their links to particular rock forming and modifying processes. The selection includes both the most common as well as rare textures observed in nature. The zircon pictures and figures are categorized according to their inferred genetic context. The examples chosen, from our own collections, from colleagues, and from the literature, are based mainly on well-understood geological situations where the geological context provides a measure of assurance that the interpretation is valid.

ZIRCON IMAGING

In common rocks zircon ranges in size from about 20 to 200 µm (Silver and Deutsch 1963). Larger zircon grains, up to several cm wide (or even up to 30 cm long as for exceptional examples from carbonatite in the Northern Territories, Australia), can be found in granitic pegmatites, syenites, kimberlites and carbonatites, whereas very small zircons may be present in aphanitic volcanic rocks, and in late stage crystallization in plutonic rocks. Observations of the external and internal properties of zircon are, therefore, made by means of microscopic observation or X-ray or electron scattering techniques.

A binocular microscope (BM; Table 1) allows us to observe macroscopic properties, such as color, degree of transparency or opacity, external morphology and form development, and the presence of inclusions, fractures and alteration. For this task it is generally useful to hold the zircon grains in a dish in ethanol in order to improve the optical quality over that obtained by observing in air. Alcohol also makes it simpler to move, turn or hand-pick the grains and to distinguish zircon from other minerals such as apatite, quartz, feldspar and titanite. Still better optical observation is facilitated by setting the zircons in dense fluids such as immersion oils, glycerine or methylene iodide, although these are usually too cumbersome for routine observation (use of methylene iodide and some immersion oils requires a special ventilation set-up because of health risks). Grain-mounts can be prepared with Canada Balsam, piperine, or various epoxy resins, but it becomes more difficult to subsequently remove the grains for isotope dilution analysis if certain epoxy resins are used.

Insights into the internal texture of zircon can be obtained with a petrographic microscope using either transmitted or reflected light. Transmitted light (TL) is useful for viewing zircon in thin section or grain mount and can reveal features such as growth zoning and metamict zones, which display different interference colors when viewed in crossed-polarized light (Chakoumakos et al. 1987, Murakami et al. 1991, Ewing et al., this volume). Observation in thin section is also useful for establishing the relations of zircon to the main rock-forming minerals. The drawback of the method is usually the small size of zircon that challenges the power of resolution of microscopes, and the difficulty of distinguishing zircon from monazite or other high-relief–high-birefringence minerals. Reflected light microscopy (RL) of polished grain-mounts, briefly etched with dilute HF vapor, is very effective in revealing growth zoning, alteration, and other features in old, relatively metamict zircons (e.g., Krogh and Davis 1974, 1975; Fig. 1.1). These techniques, BM, TL and RL (with HF etching), are

Table 1. List of abbreviations used in the paper.

Imaging technique	Abbreviation
Binocular microscope	BM
Transmitted light microscopy	TL
Reflected light microscopy	RL
U-mapping	UM
Cathodoluminescence	CL
Back-scattered electron microscopy	BSE
Secondary electron microscopy	SEM

generally not capable to properly reveal the internal textural complexity of non-metamict, crystalline zircon crystals providing zircon images that appear unzoned and internally featureless (Rudnick and Williams 1987, Hanchar and Rudnick 1995).

Uranium (and Th) maps (UM) can be obtained by inducing fission tracks in a special detector laid upon polished zircon grains by exposing them to a neutron flux in a reactor (Fig. 1.8) (e.g., Duchesne et al. 1987). Alternatively, autoradiography using a nuclear emulsion technique has been used to map α-particle tracks in zircon (e.g., Silver and Deutsch 1963).

The best resolution of internal textures is provided by cathodoluminescence (CL) or backscattered electron (BSE) imaging (Fig. 1.2–1.7). It has long been known that certain minerals, including zircon, exhibit CL when bombarded with electrons (Crookes 1879). Cathodoluminescence has been widely applied as a petrologic tool in the Earth sciences since the mid-1960s (e.g., Long and Agrell 1965, Smith and Stenstrom 1965) and this technique has been used over the past thirty-years to investigate a wide spectrum of problems in sedimentary petrology (Owen and Carozzi 1986, Owen 1987), igneous and metamorphic petrology and geochronology (e.g., Sippel 1968, 1971; Görz et al. 1970, Malcuit and Heimlich 1972, Sommerauer 1974, Ono 1976, Vocke and Hanson 1981, Vavra 1990, 1993; Hanchar and Miller 1993, and numerous other studies since the mid-1990s).

The elemental, or structural, controls of the CL emission is generally well understood for most minerals (Marshall 1988) and is usually attributed to the electronic transitions of 5d-electron transition elements, of 4f-electron electronic transitions of the trivalent rare earth elements (REEs), vibrational luminescence of the uranyl ion, or defect-related phenomena (Marshall 1988). In zircon, there is usually a broad band emission in either the blue or yellow regions, or both, of the electromagnetic spectrum upon which are superimposed sharp peaks of the trivalent REEs. Dy^{3+} is considered to be the principal elemental factor (e.g., Mariano 1978, 1989; Remond et al. 1992, Hanchar and Rudnick 1995), although other constituents such as Sm^{3+}, Eu^{2+} and Tb^{3+} may also be CL emitters in zircon (e.g., Ohnenstetter et al. 1991, Yang et al. 1992). The presence of U^{4+} and the resulting radiation damage from its decay may also suppress the CL emission (see Nasdala et al. in this volume for a more thorough discussion of the CL of zircon). Ohnenstetter et al. (1991) have

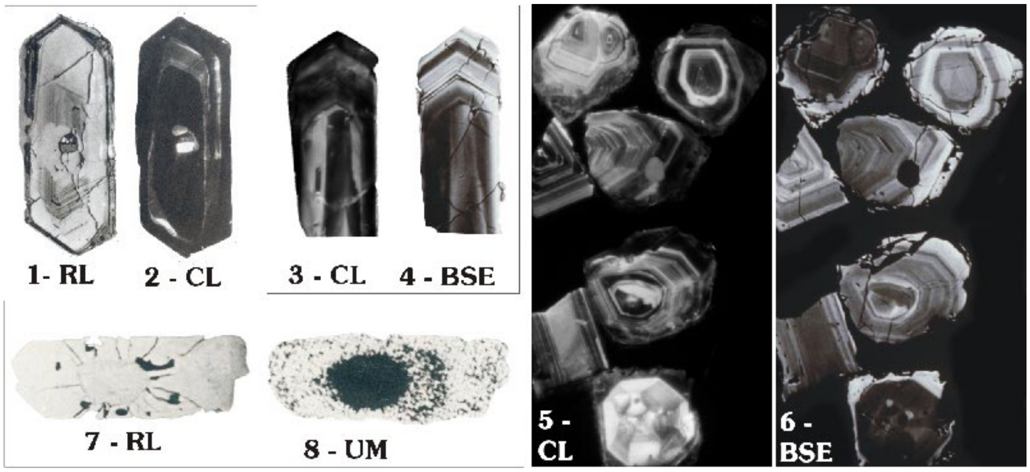

Figure 1. Imaging techniques.**(1-2)** Same zircon imaged with RL, after polishing and etching the surface with HF vapor, and CL; modified from Nemchin and Pidgeon (1997). **(3-4** and **5-6)** Comparison of CL and BSE imaging (from J.M. Hanchar, unpublished results); **(7-8)** RL image of polished zircon crystal reveals inner core and radially fractured outer shell; UM image highlights the zonation indicating very high concentrations of U in the centre, more moderate values in an intermediate shell and lower concentrations in the rim; modified from Duchesne et al. (1987).

suggested that the broad-band blue CL emission may be defect-related due to the presence of Y^{3+} and that the broad band yellow CL emission may also be defect-related due to the presence of Ti^{4+} or U^{4+}.

Back-scattered electron imaging reveals contrasts in average atomic number of regions of a phase; the higher the number, the more electrons an area will "reflect" and the brighter it will appear in the resulting image. Back-scattered electron imaging is now widely used in a variety of geologic studies and is recognized as a powerful tool for studying zonation in minerals and especially accessory minerals (e.g., Wayne and Sinha 1988, 1992; Krinsley and Manley 1989, Paterson et al. 1989, 1992a,b; Paterson and Stephens 1992, Miller et al. 1992, and numerous studies since the mid-1990s). The element primarily responsible for these BSE intensity variations in crustal zircon is Hf, with U having a secondary effect (Hanchar and Miller 1993).

In investigating zircons with these imaging techniques we have found that in many cases both techniques reveal similar features, however, usually the bright areas in CL are dark in BSE and vice versa—an observation noted by Hanchar and Miller (1993), Koschek (1993) and many other workers (Fig. 1.3-1.6). We have found that CL is generally more useful than BSE in identifying different growth regions in zircon due to the greater range in intensity of the CL emission and the additional variations in color (if done using a petrographic microscope based CL system and using color negative or slide film, or a digital camera). In addition, different growth events often have characteristic CL emission colors and this attribute of using CL can help locate *in situ* analysis locations of different isotopic age. Using a scanning electron microscope based CL system obviously reveals similar features in zircons, but unless false-color processing is done, images are in grey-scale only and the different colored CL regions remain unnoticed.

MORPHOLOGY OF ZIRCON

Zircon is tetragonal and most commonly grows as doubly-terminated prismatic crystals with elongation (length-to-width) ratios ranging from 1 to 5. This ratio is commonly believed to reflect crystallization velocity. Indeed, needle-shaped acicular zircon crystals are common in rapidly crystallized, porphyritic, sub-volcanic intrusions, high-level granites, and gabbros (e.g., Fig. 2.15–2.18),

Figure 2. External morphology variations.All grains are between 70 and 250 μm in size. **(1-21)** Variable morphology characteristics in terms of length to width ratios and typology. The latter is shown in the general context of the diagram of Pupin (1980) which is based on the relative development of the prismatic (vertical axis) and pyramidal crystal faces (horizontal axis). Note also the local presence of xenocrystic cores, inclusions of other minerals and degree of fracturing. 1 – modified from Pupin (1980), TL; 2 – only one pyramid is developed on a large subrounded core, from F. Corfu (unpublished data), BM; 3 – modified from Machado et al. (1989), BM; 4 – from F. Corfu (unpublished data), BM; 5 – ghost xenocrystic core evidenced only by bubble structure, modified from Oberli et al. (1994), TL; 6 – modified from Kröner et al. (1998), SEM; 7 – complex twinning, modified from Jocelyn and Pidgeon (1974), BM; 8 – zircon crystal totally lacking prismatic faces, from U. Schaltegger (unpublished data), SEM; 9, 10 – flat shaped, twinned crystals, from F. Corfu (unpublished data), BM; 11, 12 – modified from Pupin (1980), TL; 13,14,15 – from F. Corfu (unpublished data), BM; 16 – modified from Moser (1997), SEM; 17, 18 – highly fractured prisms in gabbro, modified from Corfu and Stott (1998), BM; 19, 20 – prominent cores overgrown by clean prisms, modified from Palmer and Davis (1987), BM; 21 – modified from Corfu and Ayres (1984), BM. **(22)** Zircon aggregate in A-type pluton, modified from Charoy and Raimbault (1994), SEM. **(23)** Thin-walled hollow zircon crystal, modified from Huneke and Rossman (1978), SEM. **(24)** Zircon fragment, typical of populations extracted from many mafic rocks, modified from Abati et al (1999), SEM. **(25-27)** Composite, resorbed grains (cauliflower zircon); 25, 27 – in meta-trondhjemite, modified from Pin and Lancelot (1982), SEM; 26 – in mafic gneiss, modified from Peucat et al. (1990), BM. **(28-30)** Magmatically resorbed grains without overgrowths. 28 – free xenocryst in granitoid rock, modified from Corfu and Ayres (1994), BM; 29-30 – highly resorbed xenocrysts in pyroclastic volcanic rock (from F. Corfu, unpublished data), BM. **(31-34)** Sub-rounded to multifaceted zircon in metamorphic rocks. 31 – in metagabbro, modified from van Breemen et al. (1986), SEM; 32 – in leucogranulite, modified from Kröner et al. (1998), SEM; 33,34 – in lower crustal xenolith, modified from Chen et al. (1998), SEM. **(35-36)** Meteorite impact related zircons. 35 – resorbed shocked zircon with traces of planar deformation features; 36 – post impact growth of polycrystalline zircon; both modified from Moser (1997), SEM.

whereas stubby and equant forms are more common in deep-seated, slowly cooled intrusions (Fig. 2.13–2.14).

Other factors affecting the shape of the zircon crystals are the composition and possibly the temperature of the crystallization medium. Systematic examination of zircon typology has led to the establishment of the widely used "Pupin diagram" (Fig. 2 inset), in which zircon crystals are classified according to the relative development of the {100} vs. {110} prismatic forms and the {211} vs. {101} pyramidal crystal forms (Pupin 1980). In general, zircon grains from relatively dry alkalic and tholeiitic igneous rocks tend to be dominated by {100} and {101} forms, where those

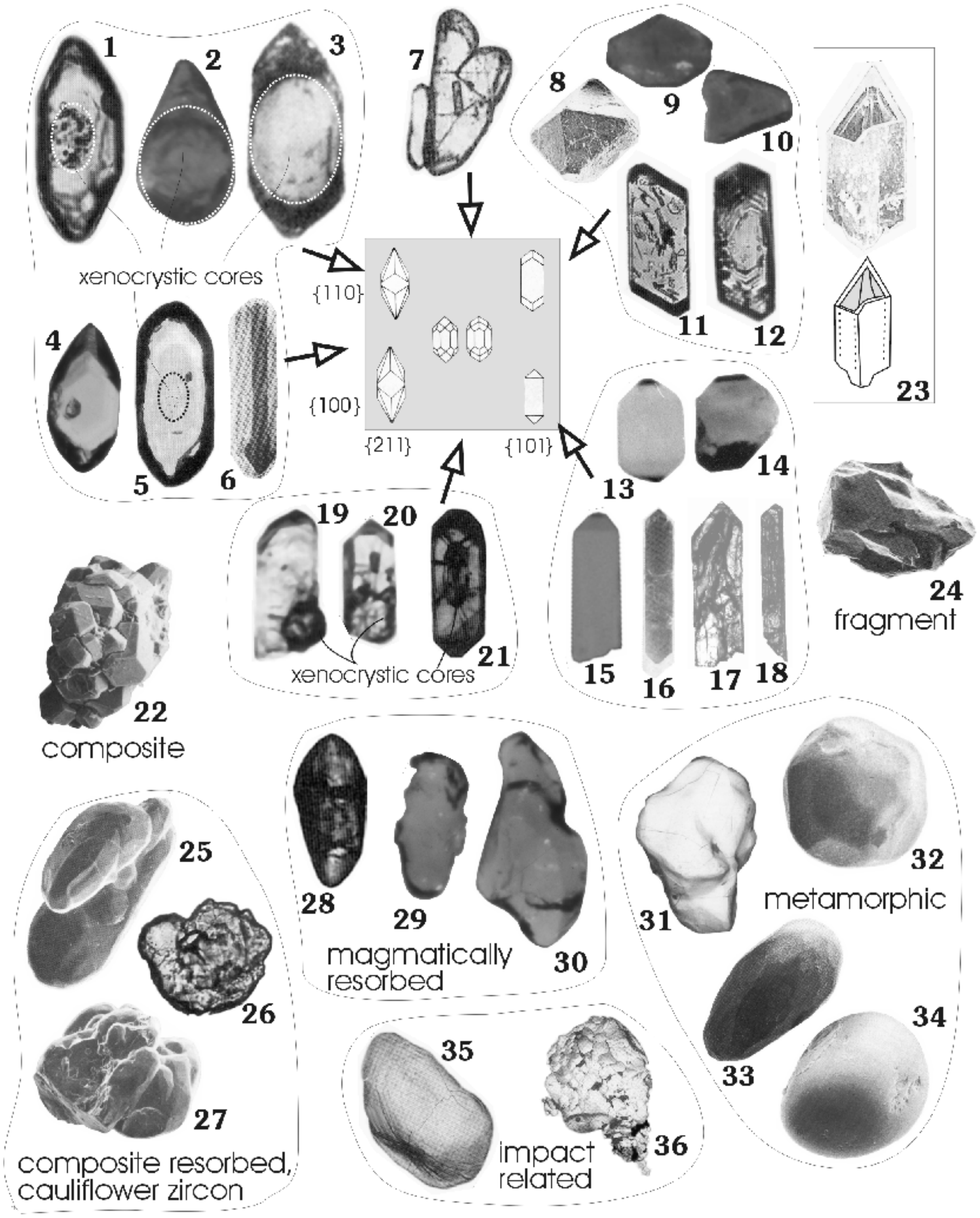

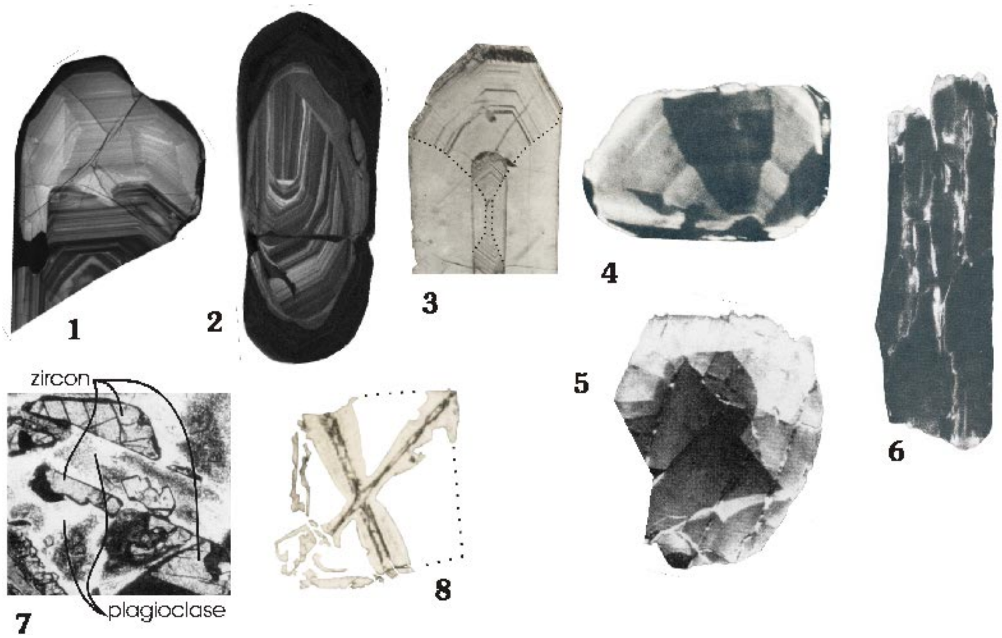

Figure 3. Complex and other types of zoning in magmatic rocks. All grains are between 70 and 250 μm. **(1-2)** Complex growth zoning with local intermediate resorption in zircon from anatectic granite, from P. Kinny (unpublished data), CL. **(3-4)** Sector zoning; 3 – section parallel to the c-axis (dotted line highlights the boundary between sectors), modified from Krogh (1982), RL of vapor etched grain; 4 – section normal to the c-axis, modified from Hoffman and Long (1984), CL. **(5-6)** Patchy zoning; 5 – zircon in norite with broad zoning superimposed by irregular domainal texture, modified from Paquette et al. (1995), CL; 6 – bright seams indicate altered fractures disrupting original zoning; modified from Vavra and Hansen (1991), CL. **(7-8)** Skeletal growth; 7 – incomplete zircon fragments growing on opposite sides of plagioclase, modified from Paquette et al. (1995), TL; 8 – incomplete zircon due to rapid growth, section perpendicular to the c-axis, modified from Krogh et al. (1982), TL.

from aluminous to calc-alkaline rocks exhibit various combinations of forms with a prominent presence of {211}, and those from water-rich granites and pegmatites tend to have {110} and {101} as their dominant forms. Pupin (1980) related the relative development of the prismatic faces mainly to the temperature of crystallization whereas the pyramidal faces were linked to chemical factors, and suggested that the typological parameters of a zircon population can be used to describe the evolution of a magma system. The somewhat simplistic nature of this interpretation has been challenged by Vavra (1993), who introduced a more sophisticated method to determine the relative growth-rates of zircon forms in order to characterize the kinetics of a crystallizing environment. Benisek and Finger (1993) also showed that compositional factors have a significant effect on the development of prism faces in zircon.

As mentioned above, the velocity of crystallization appears to be the major controlling factor of the elongation ratio for zircon. Skeletal zircon crystals are the most extreme form of rapid growth. Such zircons, observed locally in mafic and undersaturated alkaline rocks (Figs. 3.7 and 3.8) are characterized by the development of crystal-beams and walls surrounding empty space (Bossart et al. 1986). A comparable zircon type, exhibiting hollow prisms or other incompletely grown crystals, has been reported from cavities in basaltic andesite and interpreted to indicate rapid growth from a vapor phase (Fig. 2.23; Huneke and Rossman 1978). Many magmas tend to reach zircon saturation relatively early in their evolution and thus precipitation of zircon can accompany that of most other minerals. In some magmas, however, saturation is only reached late in the crystallization history, either because of very low Zr contents, or high Zr solubility or both (see Hanchar and Watson, this volume). In these cases zircon forms late in pools of highly fractionated magma, either in isolated magma pools or interstitially to other minerals. Such zircons commonly exhibit only partially developed crystal faces (e.g., Poldervaart 1956, Scoates and Chamberlain 1995; Fig. 3.7), and they are recovered from mineral separation as an assortment of broken fragments (Fig. 2.24). This is a common feature for gabbroic rocks.

The opposite case occurs when a magma is oversaturated with respect to zircon for part or most of its crystallization. Such magmas are unable to completely dissolve restitic or assimilated zircon, which quite commonly become the seed of newly grown magmatic zircon. The appearance of xenocrystic zircon can thus range from highly "polished" grains free of any overgrowth (Figs. 2.28–2.30) to subrounded grains totally enclosed in new zircon mantles (Figs. 2.1–2.3; 2.19–2.21). In some rocks one can observe a whole range of occurrences from overgrowth-free xenocrystic zircon, xenocrystic cores and volumetrically-large mantles, to entirely new igneous zircon. In addition, newly-grown zircon crystals can themselves exhibit evidence for multiple stages of growth and corrosion. All these features can be linked to complex magma evolution from initial formation by source melting, through various stages of movement through the crust, contamination and perhaps mixing with different magma batches, fractional crystallization and differentiation, with loss of cumulates and vapor, and final emplacement or extrusion. The solubility of zircon itself is largely a function of the composition of the system, described by the parameter $M = (2Ca + Na + K)/(Si \times Al)$ as well as H_2O content and temperature (Watson 1979, 1996; Harrison and Watson 1983, Watson and Harrison 1983, Hanchar et al., this volume).

Besides resorption that may occur when zircon is immersed in magma, resorption and modification, including recrystallization and Ostwald coarsening (Watson et al. 1989) can result from metamorphism. The slow diffusivity of most cations in non-metamict zircon suggests that no substantial water-free recrystallization will occur over geologically significant time periods by volume diffusion alone at the temperature conditions in normal continental crust (Cherniak et al. 1997a,b; Cherniak and Watson 2001, Cherniak and Watson, this volume). It is thus likely that any subsolidus modification of zircon will reflect active corrosion and precipitation mechanisms related to a fluid phase. Hence, it is also likely that any such reaction will occur coevally with metamorphic reaction of other mineral phases present in a rock.

As far as the external morphology is concerned, metamorphically grown, or metamorphically modified zircon crystals are generally characterized by subrounded and highly resorbed shapes (Figs. 2.25–2.27, 2.31–2.34), but euhedral shapes are also possible, especially in very fluid-rich systems such as in amphibolite facies mica schists or migmatites. Where in the former case, the development of crystal faces was probably facilitated mainly by the presence of aqueous or carbonic fluids, in the case of migmatites, zircon is likely to have grown in contact with a melt phase, and hence, strictly speaking is no longer metamorphic but magmatic. As for the subrounded metamorphic zircon type, it is possible to recognize various degrees of modification. Zircon crystals in some gneisses may only exhibit moderate rounding of the crystal edges whereas in others the original crystal shape has been destroyed, and the final product being smoothly subrounded grains (Fig. 2.31). This is commonly the case in granulite facies rocks, where zircon grains sometimes display multifaceted exteriors (Figs. 2.32–2.33). The grains may consist largely of reworked original zircon, or at the other extreme, comprise entirely new-grown metamorphic zircon. Metamorphosed mafic rocks locally contain irregular zircon grains such as the cauliflower type of Peucat et al. (1990) (Figs. 2.25–2.27). In some instances the shape of these grains may reflect resorption of originally irregular and fragmented zircons such as those recovered from some mafic rocks (Fig. 2.24), or of the composite crystals found in some granites (Fig. 2.22), but in other cases they likely represent metamorphically grown polycrystalline zircon. These are discussed in more detail later in this chapter. A special case shown in Figures 2.35 and 2.36 is that of shocked zircons from meteorite impact craters that reveal both traces of impact-related fracturing and rapid new growth of polycrystalline zircon in the immediate aftermath of impact.

ZONING TEXTURES IN IGNEOUS ZIRCON

One of the more typical features of magmatic zircon is the presence of well developed growth zoning. This feature is best seen in CL and BSE images, but in zircon affected by metamictization of U-rich areas, zoning can be revealed very well by microscopic examination (BM, RL, TL).

The zoning reflects compositional variation of Zr and Si and more importantly, variations in Hf, P, Y, the REE, U and Th—up to an order of magnitude for some of these elements (e.g., Köppel and Sommerauer 1974, Benisek and Finger 1993, Hanchar and Rudnick 1995, Fowler et al. 2002, and many other studies). The composition of the zones tends to vary between two end-members, one of which is very low in trace-elements, approaching the composition of pure zircon, and the other a zircon component highly enriched in trace elements with up to several wt % of the impurity element (Speer 1982). The mode of development of the zoning also varies widely. In some cases one observes an almost bimodal succession of trace-element rich and trace-element poor bands with almost no intermediate compositions (Figs. 4.1 and 4.2) where in other cases the zones span a much wider compositional range (Figs. 4.3–4.12), or the compositional difference becomes very small yielding only faintly visible zoning patterns (Figs. 4.13–4.15), and in some cases there is no visible zoning at all (Fig. 4.16). The thickness of the bands also varies widely. For example the bands in Figure 4.1 are on the order of 20-100 μm wide, while those in Figure 4.2 are barely 5-10 μm wide. Fowler et al. (2002) show that periodicity can be observed at different scales in their zircon megacryst, ranging from 0.5 mm down to a few μm. Moreover, within individual crystals one can observe strong variations in the relative development of zoned domains, such as in Figures 4.11 and 4.12 where one large uniform central zone is succeeded by much finer oscillatory-zoned bands. Halden and Hawthorne (1993) have shown that the zoning pattern of zircon from a carbonatite can be quantified by spectral analysis.

The origin of growth zoning is discussed in some detail by Mattinson et al. (1996) who conclude that episodic growth results from the interplay between the stage of crystal growth, the nature of the crystal-liquid interface, the degree of supersaturation of the melt, the rates of diffusion, and the state of oxidation.

In the only study yet published that investigates zircon zonation patterns in zircon populations from a range of related rocks, Hoskin (2000) analyzed the variation of oscillatory zoning in zircon (Fig. 4.17) from compositional sectors of a zoned I-type pluton (SiO_2 from 50-75 wt %; diorite to aplite zones) using CL images and fractal statistical characterization. It was found that trace-element incorporation into zircon was affected by "external forcing" (processes occurring within the magma system and not at the crystal/melt interface). The result of external forcing is to impose increasing order (as measured by the mean Lyapounov exponent, λ_m, a statistical parameter) on the oscillatory zoning pattern as magmatic differentiation proceeds. The correlation between magmatic differentiation and increasing zonation order is related to ordering in the melt by polymerization. Hoskin (2000) presented a model for zonation pattern generation that accounts for dynamics at the zircon/melt interface, cation substitution, diffusion, and melt polymerization and structure generation. This model remains untested, although new generation ion probes (e.g., nanoSIMS) may provide a means to test the model.

It is quite commonly observed that regular growth zoning is interrupted by textural discontinuities along which the original zoning is resorbed and succeeded by the deposition of new-growth-zoned zircon (Figs. 4.1, 3.1 and 3.2). These resorption intervals probably reflect intermediate periods of Zr undersaturation in the magma, owing to large-scale mixing phenomena, or to local kinetic phenomena. For example, the zircon shown in Figure 4.15 derives from the charnockitic phase of a zoned pluton and is characterized by an irregular subrounded external appearance, an almost uniform internal texture, and evidence of marginal resorption and reprecipitation. These textures suggest that it may have formed by very slow and complex crystallization of a magma body with prolonged residence time in the lower crust. In contrast, the coeval zircon in a mangeritic part of the same pluton displays simple growth zoning and no evidence of resorption (zircon not shown).

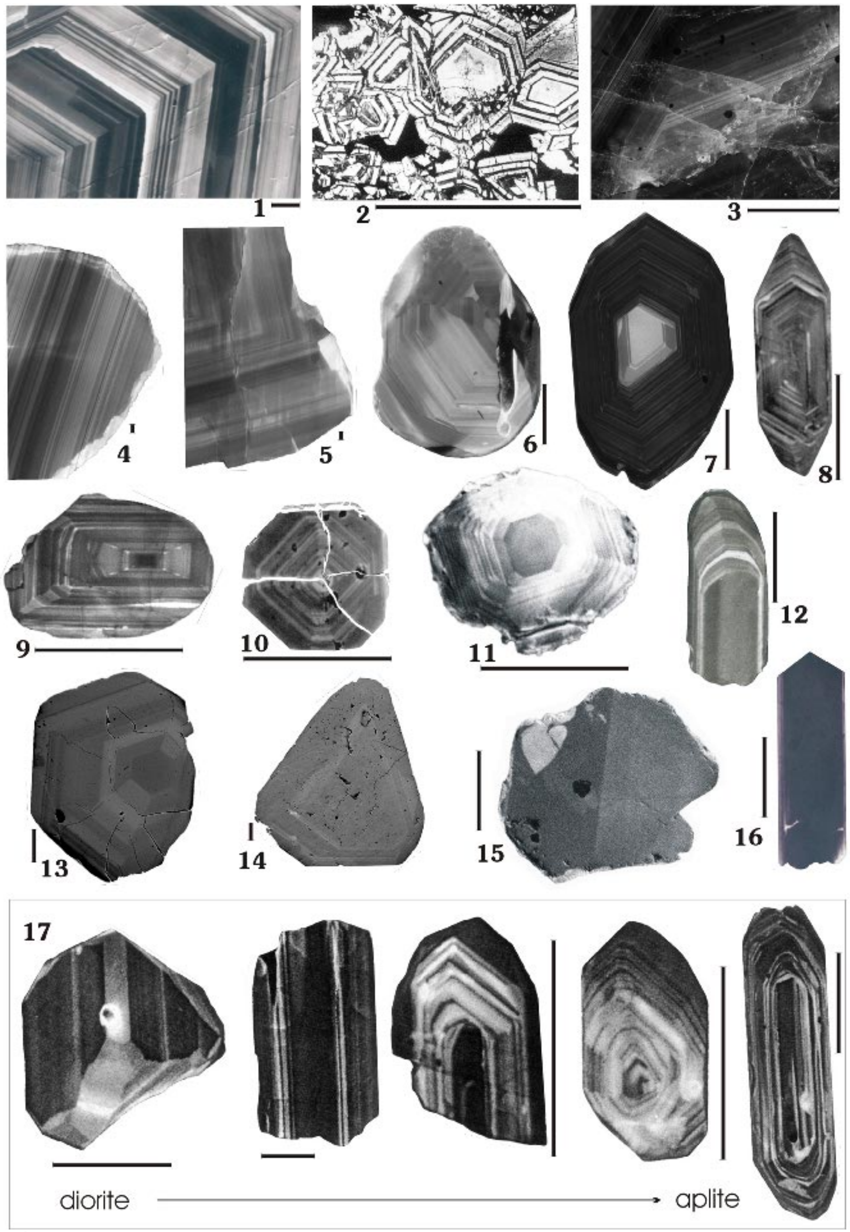

Figure 4. Variations in growth zoning in magmatic zircon. Scale bar corresponds to approximately 100 μm. **(1)** Zoned crystal from larvikite, from S. Dahlgren, unpublished data), CL. **(2)** Bimodal zoning, peralkaline complex, modified from Smith et al. (1991), BSE. **(3)** finely zoned crystal from carbonatite, from J. Hanchar (unpublished data), CL. **(4, 5**) zoned megacrystic zircon from kimberlite, from P. Kinny (unpublished data), CL. **(6-12**) growth zoning in typical crustal rocks: 6- from J. Hanchar (unpublished data), CL; 7 – from P. Kinny (unpublished data), CL; 8 – Poller (1997), CL; 9 – from P. Kinny (unpublished data), Cl; 10 – modified from Benisek and Finger (1993), BSE; 11 – from F. Corfu (unpublished data), CL, 12 – modified from Christoffel et al. (1999), CL. **(13-15)** Faint and broad zoning: 13 – carbonatite, from J. Hanchar (unpublished data), CL; 14 – pegmatite, from J. Hanchar (unpublished data), CL; 15 – mangerite (from F. Corfu (unpublished data), CL. **(16)** Homogeneous unzoned zircon in dacite, modified from Zeck and Williams (2002), CL. **(17)** Transition in style of zoning with differentiation of a pluton from diorite, through granodiorite, different adamellite phases, and finally aplite. Broad zones in zircon of diorite tend to become progressively narrower, but more frequent as the magma evolves; modified from Hoskin (2000), CL.

A special case of zoning is sector zoning. In the crystal shown in Figure 3.3, a section parallel to the c-axis, the pyramidal sectors are enriched in U (and presumably other trace-elements) whereas the prismatic sectors contain less U (Krogh 1982). In the example shown in Figure 3.4, the sectors are defined by variations between the two prismatic faces. Microprobe analyses of the different sectors reveal variations of 20-100% in Hf and Y, in part correlating with smaller changes in Zr and Si, (U is below detection limit; Hoffman and Long 1984). The development of sector zoning in zircon has been attributed to kinetic factors and rapid changes in the growth environment during crystal development (e.g., Paterson and Stephens 1992). Watson and Liang (1995) propose, however, that the occurrence of sector zoning is mainly dependent on the relation between growth rates and lattice diffusivity. In their model, particular growth surfaces are initially enriched in some elements with respect to others and these disparities are then preserved in the growing crystal if lattice diffusion is sufficiently slow. Vavra et al. (1996) attribute sector zoning to rapidly fluctuating and unequal growth rates related to the roughness of the growth surface and degree of saturation of the growth medium.

The skeletal zircon in Figure 3.8 represents an extreme case of preferential growth along specific crystallographic directions. Here, one of the prismatic faces has grown along four "ridges" that extend from the centre of the crystal (which presumably runs parallel to the c-axis). The second prismatic face only started to develop in exterior parts of the crystal late in the crystallization sequence. The central regions of the ridges remained hollow and locally may have been filled with high-U zircon, now highly metamict. Such cavities occur commonly in rapidly grown, elongated prismatic zircons.

A particular type of zoning is the irregular and patchy texture shown in Figure 3.5 (Paquette et al. 1995). This type of texture is reminiscent of undulatory extinction in strained quartz, and may reflect strain experienced by zircon during final magmatic emplacement. A distinct bending of very thin zircon crystals was observed by the first author in crystals 0.5-2 cm long from pegmatitic phases of two massive gabbroic intrusions, although the zircon was not examined by CL. The texture shown in Figure 3.5 suggests that the microfractures between the various domains were subsequently healed by new zircon growth during cooling. A somewhat similar patchy texture in elongated crystals with faint zoning and irregular longitudinal streaks (Fig. 3.6) has been interpreted by Vavra and Hansen (1991) to indicate local recrystallization along longitudinal microfractures.

Perfectly euhedral prisms without any evidence of zoning are locally observed in some rocks (Fig. 4.16). It is not clear whether the lack of zoning is due to the insufficient resolution of the imaging techniques used, or whether the particular growth environment and kinetics have contributed to form compositionally homogeneous crystals, or whether original zonation patterns have been destroyed.

XENOCRYSTIC CORES

The occurrence of xenocrystic zircon is a common feature of many igneous rocks. Zircon xenocrysts occur as cores mantled by newly grown magmatic zircon, or simply as unmantled subrounded or rarely euhedral crystals (such as when zircon is assimilated into a magma during late-stage crystallization, with too little time for corrosion or overgrowth). The recognition of xenocrystic cores is easy in some rocks but more difficult in others. Where there are distinct differences in U-content between a core and rim, differential metamictization expands the high-U part and transforms the original colorless domains into pink to brown, or even opaque, zircon. If the core is richer in U than the rim, core expansion will eventually cause fracturing of the more rigid rim (Figs. 2.19–2.21; 5.1–5.4). In the opposite case, with a low-U core surrounded by a high-U rim, there is generally no fracturing (Figs. 2.1 and 2.3, but see Figs. 13.1 and 13.2 below) but the rim will become much darker than the core. The presence of such fracture patterns and the differential coloration allow us to identify core-rim textures by simple microscopic (BM) examination. For solution-based isotope analysis it is usually relatively simple to break-off cores and rims and analyze

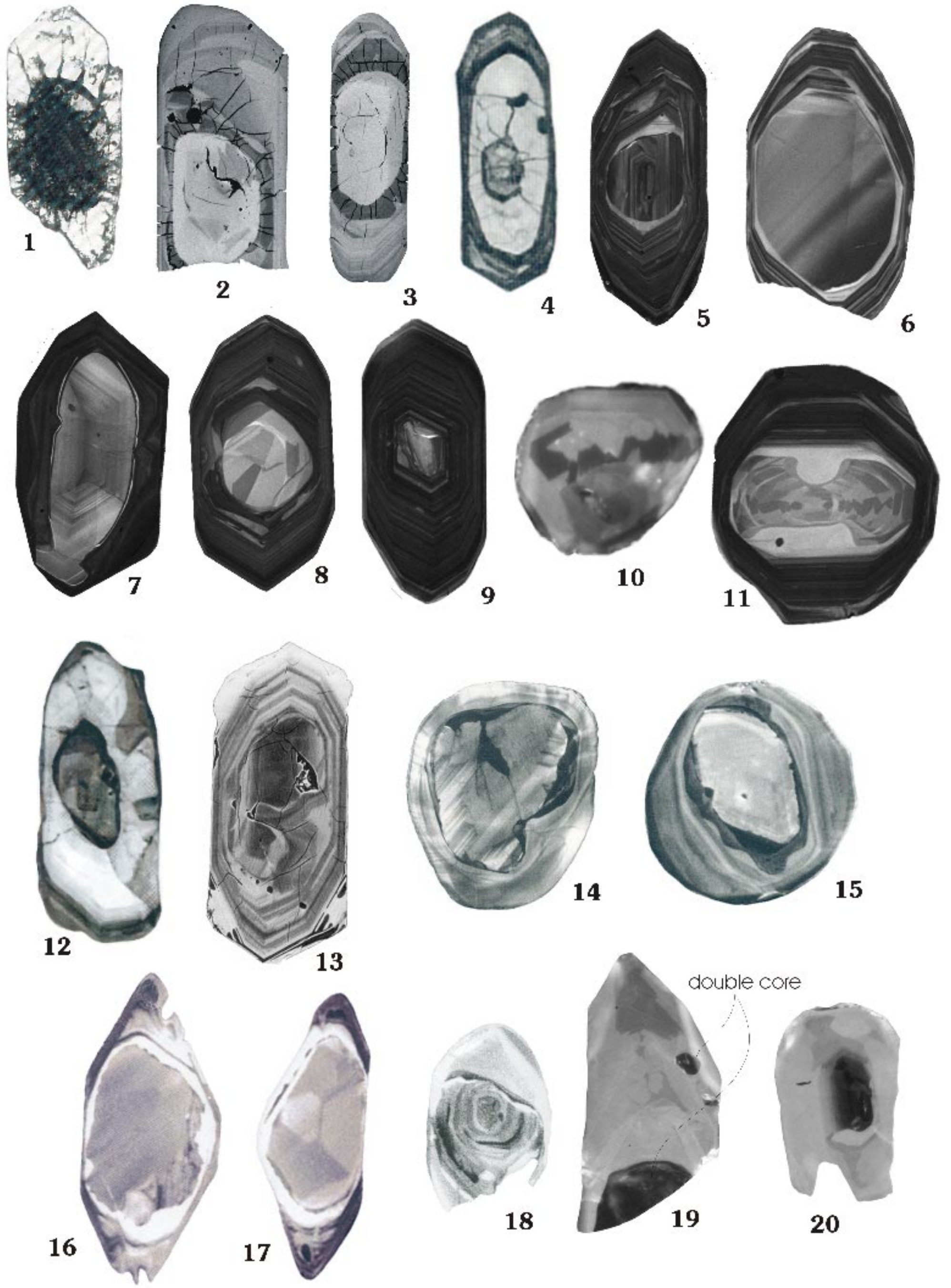

Figure 5. Variable appearance of xenocrystic cores in magmatic and high-grade meta-morphic rocks. **(1-20)** Variable appearance of xenocrystic cores in magmatic (1-13, 16-20) and high-grade metamorphic rocks (14-15), (all grains were between 70 and 250 µm in size); 1- Large metamict core has expanded and cracked the rim, modified from Welin et al. (1982), TL; 2, 3 – from J. Hanchar (unpublished data), BSE; 4 – modified from Corfu and Ayres (1984), RL; 5, 6, 7, 8, 9 – from P. Kinny (unpublished data), CL; 10 – from J. Hanchar (unpublished data), CL; 11 – from P. Kinny (unpublished data), CL; 12 – modified from Andersson and Williams (2001), CL; 13 – modified from Paterson et al. (1992b), BSE; 14-15 detrital cores, modified from Vavra et al. (1996), CL; 16,17 – modified from Zeck and Williams (2002), CL; 18 – modified from Whitehouse et al. (1999), CL; 19, 20 – from D. Moser (unpublished data), CL.

them separately for age determination. In some cases the only visible sign of a xenocrystic core is a trail of small bubbles at the core-rim boundary (Fig. 2.5).

Detection of core-rim textures becomes much more difficult in cases were both core and rim are low in U, and can thus remain colorless and unfractured even after 2 or 3 billion years. In such cases a simple visual examination under a binocular microscope will in general not be able to reveal the presence of a xenocrystic core, and even techniques like HF-etching may not help. By contrast, the application of CL or BSE imaging is successful in the majority of cases (e.g., Figs. 3.2, 5.5, 5.6, and 7.8 and 9.14 below) and, as noted above, it is often the case that different growth events preserved in zircon emit different color CL emission.

Xenocrystic cores are commonly differentiated from their rims by geometrically irregular surfaces, which truncate internal zoning (Figs. 5.5–5.8, 5.11 and 5.18) or separate subrounded, unzoned, or chaotically zoned cores from growth zoned rims (Fig. 5.2–5.3, 5.9, 5.12–5.16 and 5.19–5.20). Such discontinuities can indicate deep resorption of the early zircon phase (Figs. 5.7, 5.11–5.13), and locally they reveal that new zircon growth has occurred in a different crystallographic orientation than the substrate zircon (Fig. 5.11). In specific situations, however, it can be difficult to distinguish a xenocrystic core from other features such as zones of local recrystallization or specific magmatic growth bands, or to exactly locate the actual boundary between a core and a magmatic rim (Figs. 5.4, 5.12, 5.16 and 5.17). It is common to have more than one discontinuity within an individual zircon, and, in principle, they could indicate the presence of multiple core generations, a combination of core (early) and mantle (later) resorption events, or multiple stages of magmatic resorption within a single magmatic event. Interpretations can commonly be made with confidence, or the possibilities reduced, when the textural observations are combined with isotopic analysis of specific zones.

In some instances zoned xenocrystic cores can retain a euhedral outline that progresses—without apparent discontinuity—into zoned rims. In such cases, only isotopic analysis of specific areas (crystal middle and crystal edge) can delineate the presence of a xenocrystic core (Paterson et al. 1992b).

Some difficulties are met when one attempts to evaluate the origin of xenocrystic cores. In specific cases, key evidence can be provided by direct field observation. For example, xenocrystic cores found in zircon grown in a migmatite within a clastic sedimentary sequence, or in a classical S-type granitic body, can readily be interpreted as being of detrital origin. The frequency of isotopic ages and age omissions obtained for xenocrystic zircon populations can be linked to potential sedimentary sources. In the case of xenocrystic zircon cores found in granitic bodies of less obvious crustal origin it is not possible in general to unambiguously verify a detrital origin. If the source-region of a granitoid body is a mixed gneissic terrane, then the xenocrystic zircons could be both supracrustal and magmatic in origin; in other cases one could easily expect that multistage magmatic zircon will become incorporated into newly grown igneous zircon. Hence, in most cases a clear and straightforward interpretation of the origin of xenocrystic cores is not possible.

Xenocrystic cores themselves do not yield many clues as to their origin. Occasionally they preserve the abrasions and fracturing caused by erosion and sedimentation process (Figs. 5.14 and 5.15) that support independent evidence for a detrital origin, but otherwise such clues are too ambiguous to be trusted.

SUBSOLIDUS MODIFICATIONS AND GROWTH OF ZIRCON

Late-magmatic phenomena

Zircon can be affected by various processes at various times: the final stages of magmatic crystallization, during slow cooling of large intrusive bodies, and by later metamorphic events. Distinction between the effects of the processes is not always straightforward, and there is not always consensus on the interpretation of secondary textures.

Modifications of magmatic zircon during late and post-magmatic cooling tends to result in a disruption of concentric oscillatory zoning. One of the most commonly observed textures is the development of irregular domains of homogenous, low-U zircon cutting discordantly across growth zoned domains (Figs. 6.1–6.7). These domains are thought to develop by recrystallization, a process promoted by the relative instability of trace-element-rich domains with respect to trace-element-poor zircon. Recrystallization is probably promoted by the presence of magmatically derived aqueous fluids in deep-seated settings (Pidgeon 1992, Nemchin and Pidgeon 1997, Schaltegger et al. 1999). The recrystallization process expels trace elements, shifting the composition closer to that of pure zircon, and apparently concentrates the impurities in trace element-rich convolute zones (Figs. 6.5, 6.10–6.12 and 6.17; Pidgeon et al. 1998).

Another process appears to involve metasomatic replacement of zircon creating trace-element-rich domains. For example, the zircon prism displayed in Figure 6.16 is characterized by a mosaic texture which appears to have developed by modification of an originally low-U zircon, either during a late magmatic stage or subsequent metamorphism (Corfu and Ayres 1984). The occurrence of "bent" prisms in this population suggests that development of the mosaic texture may have been preceded by the formation of a patchy (strained) texture similar to that observed in Figure 3.5.

Medium to high temperature metamorphism

The three zircons shown in Figures 6.13–6.15 display the progressive development of a veined and brecciated texture starting from relatively homogeneous zircon (Ashwal et al. 1999). U-Pb dating indicates that the amount of veining affecting these zircon grains correlates with the degree of younging, indicating that loss of Pb was caused by metamorphic recrystallization, in which case grain boundary diffusion most likely overrode volume diffusion. Similarly, the bulbous replacement or recrystallization texture displayed by the zircon crystal in Figure 6.6 has been shown to have occurred during a metamorphic event (Schaltegger et al. 2002). Connelly (2001) has documented very subtle metamorphic recrystallization, which has led to a gradual but homogeneous fading of original growth zoning and is correlated with extensive amounts of Pb loss.

Zircon in high-grade metamorphic rocks display a wide diversity and complexity of textures that reflect variations in the physico-chemical conditions and the duration of each metamorphic event, and are caused by modifications of pre-existing structures and/or by growth of new zircon (Fig. 7). The least severely affected zircon grains can partially preserve vestiges of an original growth zoning, only locally modified by metamorphism, thus displaying textures closely resembling those for late-magmatic recrystallization as discussed above (Figs. 7.1–7.5; cf. Fig. 6) (Hoskin and Black 2000). Igneous protolith zircon from the Proterozoic Georgetown Region, Australia, experienced variable recrystallization during an upper-amphibolite-grade event. The zircon largely preserves igneous oscillatory zoning, although this becomes progressively convoluted, blurred and thickened in response to metamorphism. The dominant texture, however, is transgressive (across all pre-existing textures) zircon patches and lobes. Areas of recrystallization occur dominantly at crystal terminations, but also anywhere else within the interior of a crystal and sometimes apparently not connected to the crystal surface. Of significance is the preservation of relics of primary textures (growth zoning) within areas of recrystallisation. These relics are termed the "ghost texture" and are responsible for "mixed" isotopic ages and trace-element abundances between growth-zoned and fully recrystallized areas. Hoskin and Black (2000) interpreted these textures to represent recrystallization in the solid-state because ghost textures and the isolation of some recrystallized areas from the crystal surface are inconsistent with a local dissolution/reprecipitation (fluid) process.

In general, zircon in granulite facies rocks tends to be characterized by very chaotic textures. Concentric zoning, when present (Figs. 7.6–7.12), is rather irregular and resembles only weakly the parallel or regular geometry of zoned magmatic zircon (cf. Fig. 4). Some variants of sector and fir-tree zoning are very common (Figs. 7.13–7.19), the latter reflecting strong fluctuations of growth rates (Vavra et al. 1996). The most extreme textural types have abstract and chaotic designs that

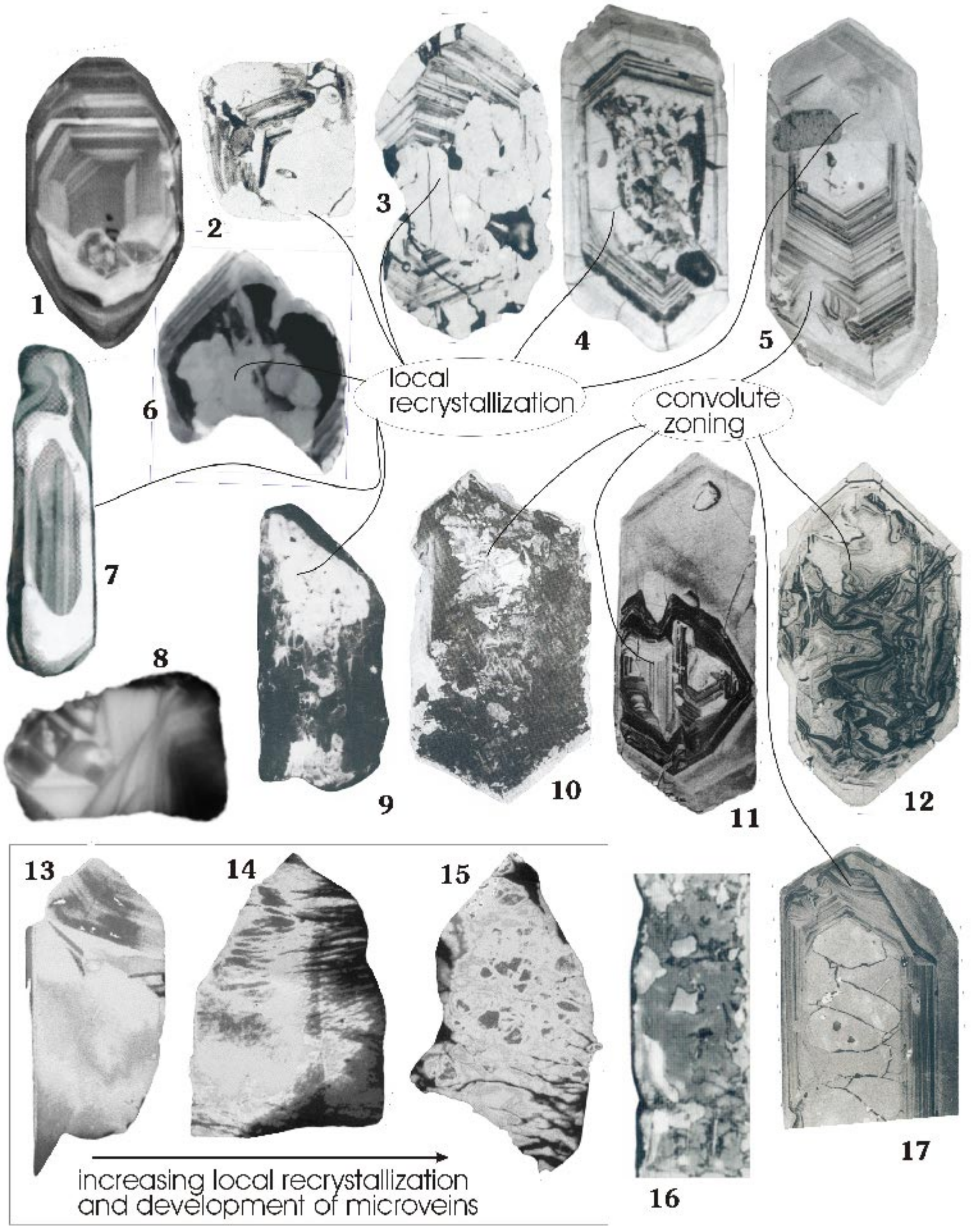

Figure 6. Late to post-magmatic recrystallization of zircon. The grains shown are between 70 and 250 μm in size. **(1)** Oscillatory zoning cut off by area of re-homogenized zircon, modified from Poller (1997), CL. **(2-7)** Partially preserved growth zoned zircon penetrated by trangressive zones of recrystallization and with local development of convolute zoning; 2,3 – modified from Pidgeon (1992); RL; 4, 5 - modified from Nemchin and Pidgeon (1997), RL; 6 – modified from Schaltegger et al. (2002), CL; 7 - modified from Andersson and Williams (2001), CL. **(8)** ”cross-bedding type” texture (from J. Hanchar, unpublished data) **(9-12, 17)** Heterogeneous patchy pattern and convolute zoning attributed to post-crystallization purification of crystal structure with progressive migration of trace element rich bands; 9 - modified from Vavra and Hansen (1991), CL; 10 – modified from Mulch et al. (2002), CL; 11, 12, 17 – modified from Pidgeon et al. (1998), RL. **(13-15)** Zircon in leuconorite exhibiting increasing amount of local recrystallization and microveining (with addition of U), which correlates with resetting of U-Pb age, modified from Ashwal et al. (1999), CL. **(16)** Patchy, mosaic texture, indicating metasomatic replacement of low-U domain by zircon richer in U (and presumably other trace elements), modified from Corfu and Ayres (1984), RL.

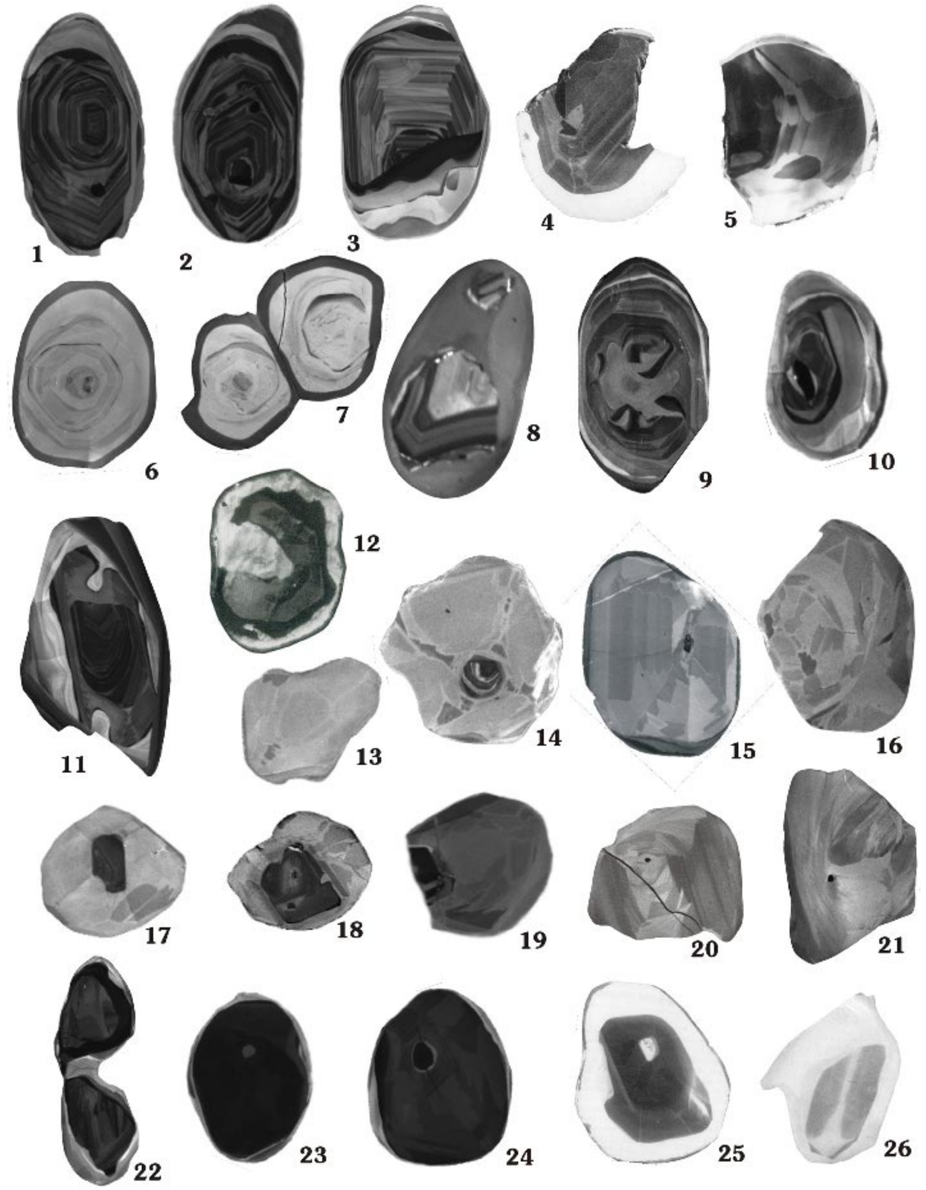

Figure 7. Recrystallization and new growth of zircon in high-grade metamorphic rocks. All grains between 70 and 350 µm in size. **(1-5)** Original euhedral zircon is cut by recrystallized or newly grown domains of more homogeneous composition; 1, 2 – Akilia gneisses, from P. Kinny (unpublished data), CL; 3– Akilia gneisses, modified from Nutman et al. (2002); 4, 5 – lower crustal xenoliths, modified from Moser and Heaman (1997), CL. **(6-12)** Zircon displaying very irregular concentric zoning locally overprinted by zones of recrystallization or new growth; 6, 7, 8 – lower crustal xenolith, from M. Schmitz (unpublished data), CL; 9, 10, 11 – in various metamorphic rocks, from P. Kinny (unpublished data), CL; 12 – in mafic granulite, modified from Peucat et al. (1990), CL. **(13-19)** Sector and fir-tree zoning, locally surrounding older zircon components; 14,16 – in lower crustal xenolith, modified from Schmitz and Bowring (2002b), CL; 15 – in granulite facies rock, modified from Pidgeon et al. (2000), CL; 13,17,18 – in high-grade gneisses, from P. Kinny (unpublished data), CL. **(20-22)** Chaotic textures with local appearance of 'flow' domains; 20,21 – lower crustal xenoliths, modified from Schmitz and Bowring (2001), CL; 22 – in migmatitic gneiss, from P. Kinny (unpublished data), CL. **(23-25)** Bands or other large segment of homogeneously textured zircon; 23, 24 – Akilia gneiss, from P. Kinny (unpublished data), CL; 25 – lower crustal xenolith, modified from Moser and Heaman (1997), CL, 26 – in granulite, modified from Bingen et al. (2001a), CL.

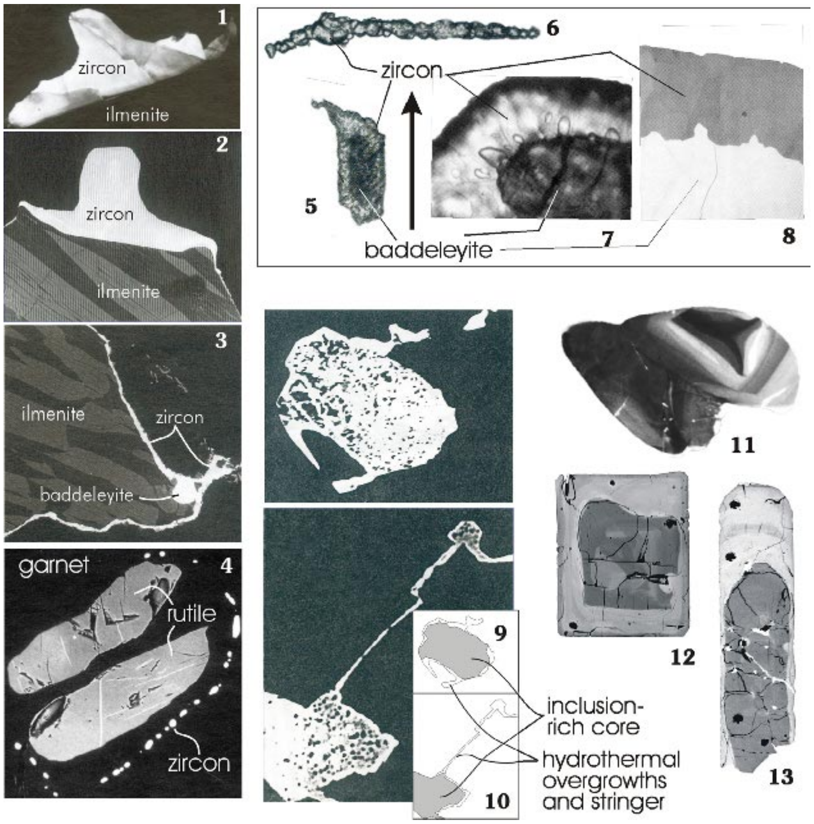

Figure 8. Modes of metamorphic-hydrothermal zircon growth. **(1-3)** Development of zircon in granulites; 1,2 – hat-shaped zircon wrapping around ilmenite, 3 – Thin layer of zircon coating ilmenite, in contact with a baddeleyite grain; modified from Bingen et al. (2001a), 1 = CL, 300µm wide; 2, 3 = BSE, 100 µm wide. **(4)** Zircon forms string of beads around rutile, both surrounded by garnet, modified from Bingen et al. (2001a), BSE, 100 µm wide. **(5-8)** Formation of zircon from baddeleyite; 5 – zircon corona around baddeleyite, TL (thin section), 100 µm long; 6 – chain of zircon crystals in plagioclase (complete reaction from baddeleyite); TL (thin section), 250 µm long; 7, 8 – detail of zircon-baddeleyite relationship, TL (7) and BSE (8), image ca. 80 µm wide; all modified from Davidson and van Breemen (1988). **(9-10)** Late-magmatic zircon, inclusion (thorite) – rich, overgrowth by hydrothermal, inclusion-free zircon, modified from Rubin et al. (1989), BSE, grains are 5 to 10 µm wide. **(11)** Metasomatic zircon in ultramafic rock, modified from Grieco et al. (2001), CL. **(12-13)** U-rich hydrothermal replacement rims around low-U zircon, from J. Hanchar (unpublished data) BSE, both crystals are ca. 100 µm wide.

combine stepwise growth patterns with flow structures (Figs. 7.20–7.22). Besides these geometrically complex patterns, it is not uncommon to find zircons, or at least large domains of zircons, that are completely homogeneous (or nearly so) when examined by common imaging techniques (Figs. 7.23–7.26; also parts of other grains in Fig. 7). In the case of domains that are homogeneously dark in CL (or light in BSE), they can be suspected to be free of zoning because the luminescence may be poisoned by high trace-element contents or by metamictization. However, the domains that provide very bright CL images are likely to be genuinely homogeneous as they have very low trace-element contents. Figures 7.8, 7.11 and 7.12, in particular, indicate how such domains evolve as marginal bands and as lobes that locally penetrate the interior of grains, but locally they also form amoebic zones entirely enclosed in the centre of the grains (Fig. 7.9).

Bingen et al. (2001a) describe how metamorphic zircon in a granulite developed hat-shaped overgrowths on older zircon and ilmenite (Fig. 7.26), or very long, thin coatings following the

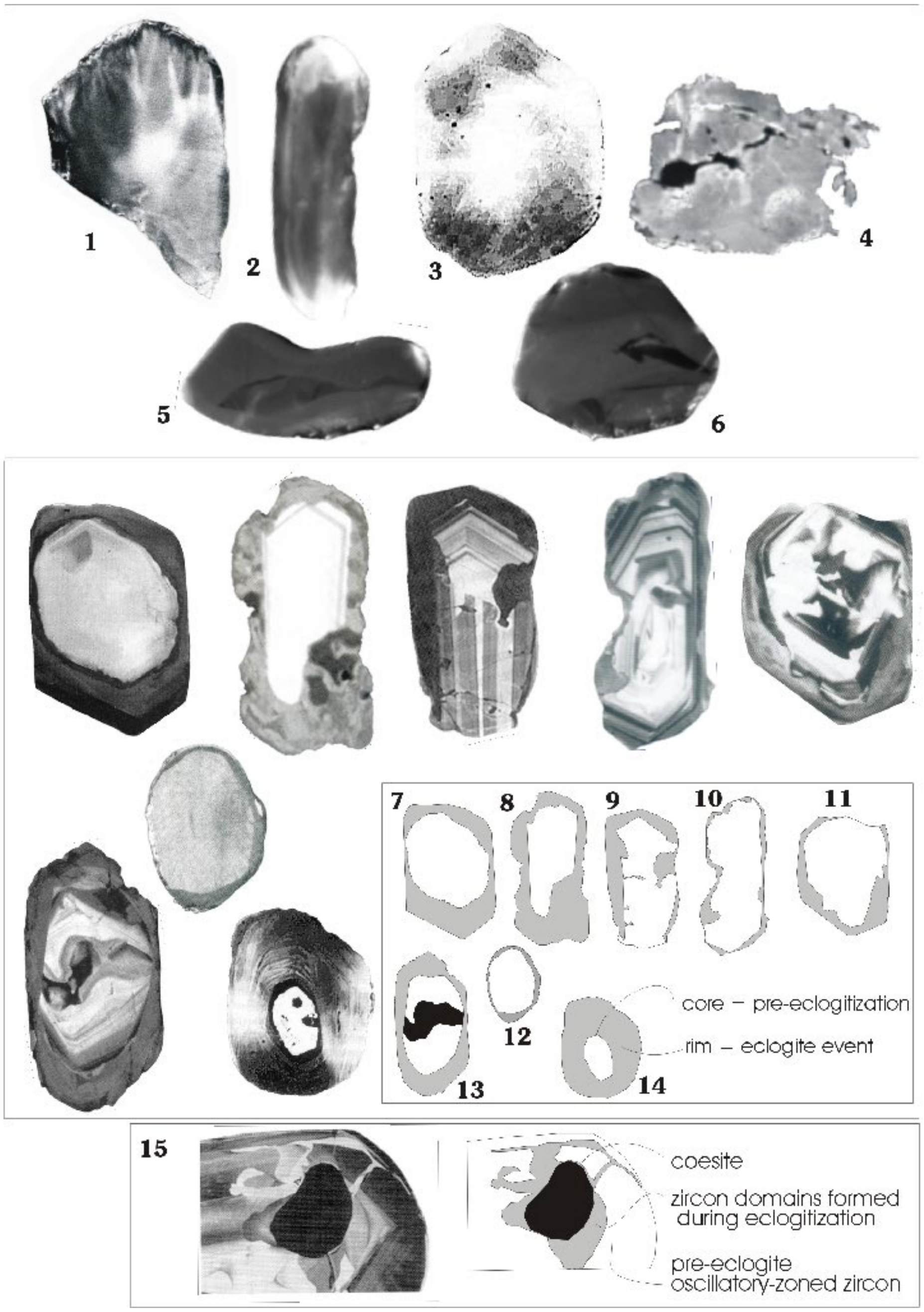

Figure 9. Zircon in high-pressure rocks. The grains shown are all between 70 and 300 μm in size. **(1-3)** Irregular, diffuse (auroral-light) zoning; 1 – Corfu et al. (2002), CL; 2 – modified from Schmitz and Bowring (2002a), CL; 3 – modified from Rowley et al. (1997), CL. **(4-6)** Largely homogeneous texture; 4 – modified from Lopez Sanchez-Vizcaino et al. (2001), CL; 5,6 – modified from Schmitz and Bowring (2002a), CL. **(7-14)** Eclogitic zircon replacing and rimming pre-metamorphic phase; 7- modified from Rubatto et al. (1998), CL; 8 – modified from Hacker et al. (1998), CL; 9 – modified from Gebauer et al. (1997), CL; 10,11 – modified from Rubatto and Gebauer (1999), CL; 12 - modified from Oberli et al. (1994), CL; 13 – modified from Liermann et al. (2002), CL; 14 - modified from Rowley et al. (1997), CL. **(15)** Relationship between old-zoned zircon and zircon domains formed metamorphically together with the coesite pseudo-inclusion, modified from Gebauer et al. (1997), CL.

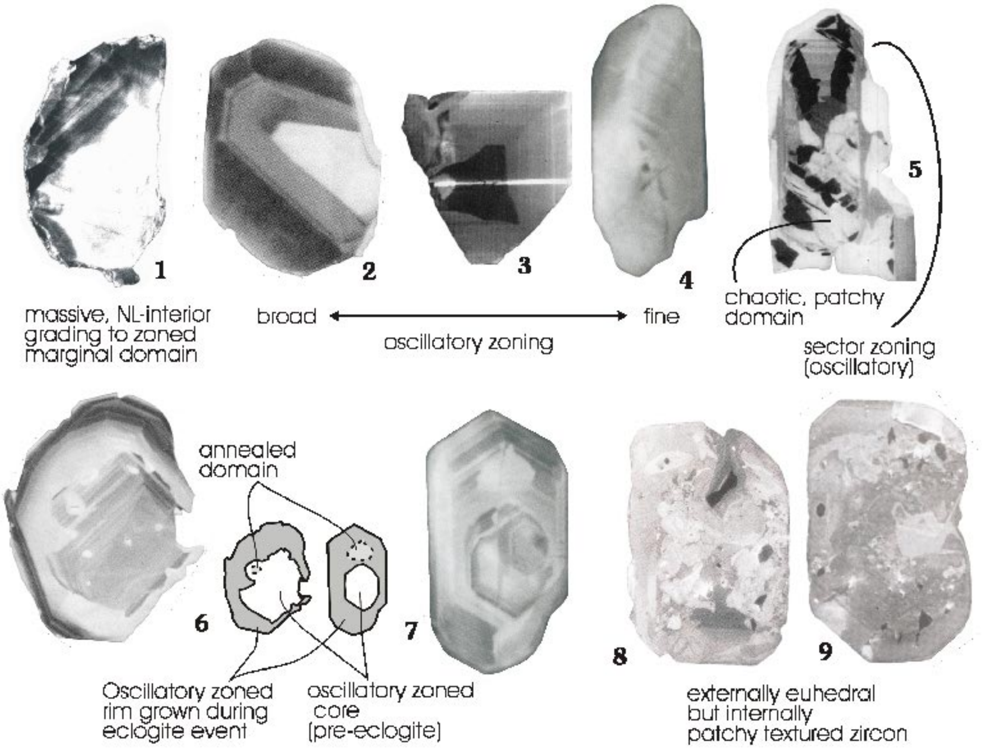

Figure 10. Zoning of zircon in high-pressure rocks. The grains shown are all between 70 and 300 μm in size. **(1)** Internal diffuse zoning rimmed by growth zoned marginal domain; Corfu et al. (2002), CL. **(2-4)** Variation in growth zoning, 2 – modified from Gebauer et al. (1997), CL; 3 – modified from Rubatto et al.(1998), CL; 4 – modified from Bingen et al. (2001b), CL. **(5)** complex zoning, modified from Rubatto et al. (1998), CL. **(6-7)** cored eclogitic zircon with zoned texture; 6 – modified from Gebauer et al. (1997), CL; 7 - modified from Bingen et al. (2001b), CL. **(8-9)** Patchy textured zircon in eclogite, modified from Bröcker and Enders (1999), CL.

grain-boundary of or fractures in ilmenite (Figs. 8.1–8.3), and deduce that the required Zr was provided by the breakdown of ilmenite and baddeleyite.

High-pressure metamorphism

Understanding the nature of zircon in eclogites is an intriguing and difficult task, especially given that the dating of high-pressure events is significant for the reconstruction of the history of ancient collisional belts. In the simplest cases, eclogite zircons are subrounded and somewhat irregular, but display relatively homogeneous internal textures. The example in Figure 9.1 exhibits a wavy "auroral light" texture. This texture is typical for a zircon population yielding an isotopic age that dates a high-pressure event (Corfu et al. 2002). A similar texture is also shown by the grains in Figures 9.2 and 9.3, whereas those in Figures 9.4–9.6 are more uniform but locally contain darker zones.

In general, eclogites contain complex zircon types. One common type contains two distinct phases, older relicts pre-dating eclogitization of the rock surrounded and/or penetrated by new metamorphic zircon (Figs. 9.7–9.15). Cores can be homogeneous or growth zoned, locally with traces of earlier resorption and recrystallization (Figs. 9.9 and 9.13). Metamorphic rims are generally homogeneous to somewhat heterogeneous, and are separated from cores by irregular interfaces indicative of corrosion. The latter feature is especially evident in Figure 9.15, which shows new metamorphic zircon developed, together with coesite, in a cavern in the interior of the original crystal. The new material likely penetrated from outside the crystal along a network of thin fractures.

The homogeneity of metamorphic zircon and intra-crystalline domains discussed above contrasts with the oscillatory zoning shown by zircon in Figure 10. The metamorphic nature of the latter is supported, in each case, by the consistency of their U-Pb ages within geological context. In general, the zoning is regular, defining either very fine or very coarse bands, and is quite similar to that of magmatic zircon (Figs. 10.1–10.4; 10.6 and 10.7). A complex pattern more typical of granulite facies zircon crystals is shown by the grain in Figure 10.5. The grain shown in Figure 10.1 is the only grain within a zircon population (examined by CL; see also Fig. 9.1) that shows such marginal fine-scale zoning. More prominent development at the margin of the grain is also evident in Figure 10.6. The presence of such zoning in metamorphic zircon runs against "common wisdom" and has caused some consternation in the literature. Gebauer et al. (1997) suggest that the zoning seen in such grains (Figs. 10.2 and 10.6) probably reflects crystallization in local melt or supercritical fluids that may have developed at peak metamorphic conditions. They also draw attention to the occurrence within these grains of homogeneous domains around small inclusions, suggesting that they represent zones of annealing that caused exchange of chemical elements with the inclusion (Figs. 10.6 and 10.7).

A more unusual texture is the highly irregular patchy pattern (Figs. 10.8 and 10.9) observed in euhedral zircon from a low-temperature eclogite from Greece (Bröcker and Enders 1999). The authors interpret the zircons as having formed by metasomatic processes during a high-pressure event, although it could be argued that the eclogite event may only have caused textural disruption rather than new zircon formation. Some clues concerning the mechanisms that form zircon in eclogite have been provided by Bingen et al. (2001b) who suggest that zircon coronas around ilmenite are cannibalized during breakdown of ilmenite (to rutile and garnet; Fig. 8.4) to form larger zircon grains.

HYDROTHERMAL ZIRCON

This is a somewhat artificial subdivision since it could be that all metamorphic zircon growth (and resorption) occurs only in the presence of a fluid phase (silicate melt or aqueous fluid). The reaction producing zircon during baddeleyite breakdown (Figs. 8.5–8.8; Davidson and van Breemen 1988) involves the addition of silica and probably also other cations, since such zircons have, for example, quite different Th/U ratios than the parent baddeleyite. The transport of silica and other cations is probably via aqueous fluid. Other examples of zircon growth that may have been assisted by fluid are the growth of zircon on ilmenite (Figs. 8.1–8.3) in granulites and the coronas of micro-zircons observed around rutile in eclogites (Fig. 8.4).

Hydrothermal zircon growth has been described in a peralkaline environment (Figs. 8.9 and 8.10; Rubin et al. 1989), where metasomatism appears to have occurred during late-stage magmatic crystallization. The metasomatic zircon shown in Figure 8.11 developed during metasomatism of ultramafic rocks in the mantle (Grieco et al. 2001). In a similar setting, zircon has been observed in association with baddeleyite/zirconolite rims in metasomatic veins cutting mantle peridotite (Kinny and Dawson 1992). The examples in Figures 8.12 and 8.13 indicate the formation of high-U zircon margins, which in some cases are simple overgrowths, but more commonly are embayments into low-U regions in the zircon crystals. These high U regions may have formed by metasomatism, or by recrystallization, or dissolution and reprecipitation during an event, which probably was accompanied by regional hydrothermal activity (McLelland et al. 2001, Hanchar et al. in preparation). The well preserved outer boundary of the crystal would tend to support some simple replacement mechanism although the nature of this process remains elusive. The pattern observed for the grains in Figures 3.6 and 6.13–6.15 may well fit a similar process. Most likely, these high-U regions in the zircon crystals are not the result of simple volume diffusion of U diffusing in and Zr diffusing out based on the sluggish kinetics of U-diffusion in zircon under crustal conditions (Cherniak et al. 1997b).

Although on occasions workers suggest that their zircons are of hydrothermal origin, ambiguity still exists. Unequivocal occurrences of aqueous-fluid precipitated zircon reveal it to have a "spongy" texture (Wayne and Sinha 1992, Hacker et al. 1998—Fig. 3 therein; Hoskin et al. 1998) and to be extremely enriched in high-field strength elements, the REE (Hoskin et al. 1998), non-radiogenic lead (Watson et al. 1997) and F (Hoskin 1999). We consider these characteristics to be useful criteria for identifying zircon crystallization from aqueous fluids at low pressure (<2 kbar), low temperature (<500°C) and high water/rock ratios.

KIMBERLITIC AND MANTLE-RELATED ZIRCON

The term "kimberlitic zircon" is used here to refer to megacrystic zircons commonly found in kimberlite, carbonatite, alkali basalt and other magmas of deep-seated origin, and more rarely found as a component of syenitic xenoliths carried by such magmas. The dominant characteristic of kimberlitic zircon is their common large size (up to cm size) and anhedral morphology (Kresten et al. 1975; Belousova et al. 1998). The internal textures display a broad range of variation. The megacrysts shown in Figures 11.1–11.4 are largely homogeneous, except for some faint outlines of large angular domains, possibly related to fracturing. The grain in Figure 11.5 preserves a very faint

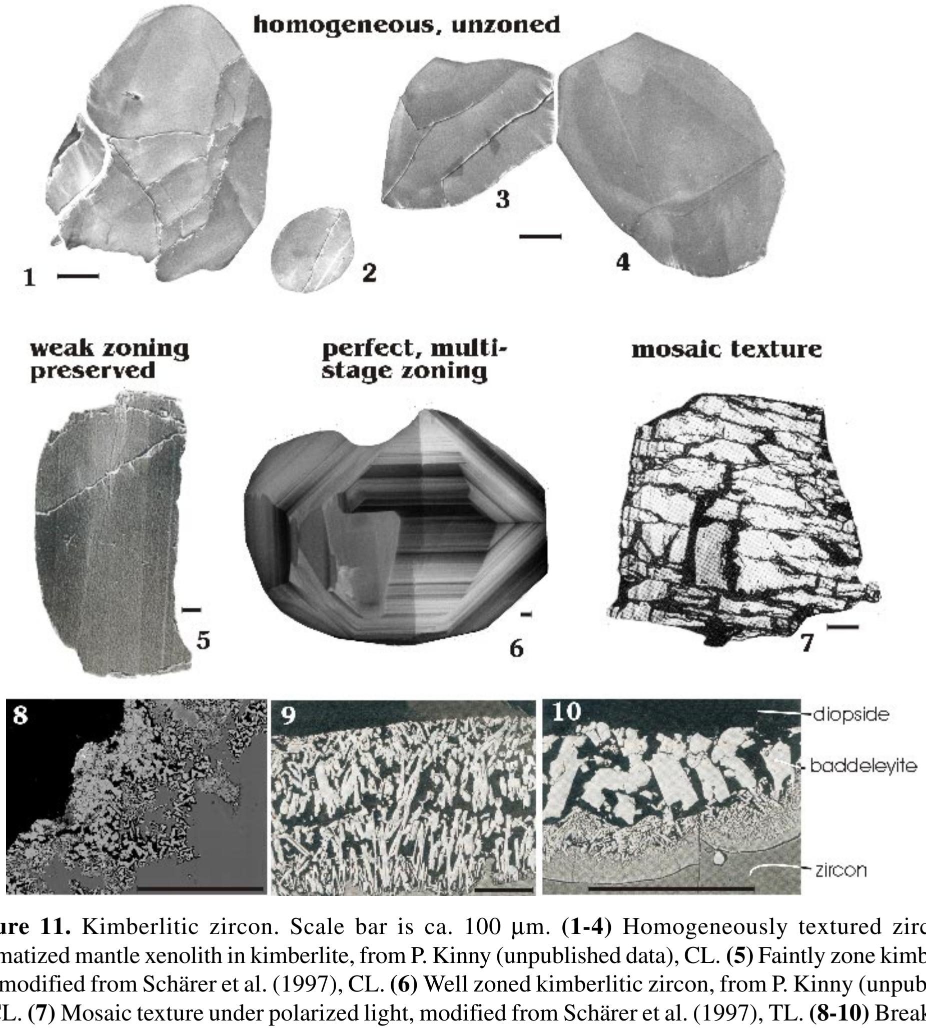

Figure 11. Kimberlitic zircon. Scale bar is ca. 100 µm. **(1-4)** Homogeneously textured zircon in metasomatized mantle xenolith in kimberlite, from P. Kinny (unpublished data), CL. **(5)** Faintly zone kimberlitic zircon, modified from Schärer et al. (1997), CL. **(6)** Well zoned kimberlitic zircon, from P. Kinny (unpublished data), CL. **(7)** Mosaic texture under polarized light, modified from Schärer et al. (1997), TL. **(8-10)** Breakdown of kimberlitic zircon to baddeleyite, 8 – from P. Kinny (unpublished data), BSE; 9,10 – modified from Heaman and LeCheminant (1993); BSE.

and broad zoning texture. By contrast, the grain shown in Figure 11.6 reveals a splendid, though complex, growth zoning. Two similar grains are shown in Figures 4.4 and 4.5. The reason for these variations is not clear. Perhaps the poor development of zoning in some grains may be related to prolonged residence of the megacrysts at very high temperatures in the mantle, which may have led to partial or complete homogenization of any original zoning, in which case those megacrysts with well preserved zoning would not have remained in the source region for a long time. Certainly, the commonly observed age relation of megacrysts to the erupting magma is one of short pre-eruptive residence time for the megacrysts, but there are exceptions. Another common observation is that, where present, the oscillatory zonation in kimberlitic zircons is often truncated by the anhedral grain margin (e.g., Figs. 4.4 and 4.5) indicating that despite their large size they have been substantially resorbed from originally larger grain-sizes.

Figure 11.7 illustrates a polarized light view of the same grain seen in Figure 11.5. The distinct mosaic structure has been interpreted as a possible brittle stress-related feature affecting the zircon at great depths (Schärer et al. 1997) although this is more likely due to rapid pressure reduction prior to eruption.

Figures 11.8–11.10 show a commonly observed reaction rim between zircon and other silicates leading to the formation of intervening baddeleyite and occasionally also zirconolite (Heaman and LeCheminant 1993). These desilification reactions have been linked to episodes of metasomatism in the mantle, but may also develop during late-stage contact of zircon megacrysts with a silica-undersaturated, ascending magma.

IMPACT-RELATED TEXTURES

A rare class of zircon comprises those grains related to large meteorite impacts. Their most diagnostic characteristic is the presence of multiple sets of planar deformation features (Figs. 12.1–12.6 and Fig. 2.35), which are revealed particularly well by scanning electron microscopy (SEM) on etched surfaces (Bohor et al. 1993). These features, however, can often also be seen with normal transmitted or reflected light microscopy (Figs. 12.2 and 12.4) in grain-mounts, or in thin section. Under a binocular microscope, shocked grains appear whitish and highly turbid to completely opaque, but occasionally it is possible to detect the characteristic planar features (Krogh et al. 1984, 1993).

At increasing degrees of shock the zircons develop granular textures and turn into polycrystalline grains (Figs. 12.7 and 2.36). Under the most extreme conditions they start to melt, a process that results in textures such as those shown in Figures 12.8 and 12.9. Shocked zircon grains that get trapped in an impact melt layer may grow new rims, which are distinguished mainly by their lack of impact-related deformation, indicating that they formed after the immediate impact event (Figs. 12.5, 12.6 and 2.16). Such zircons are invaluable for dating the time of the impact (Kamo et al. 1996, Moser 1997, Gibson et al. 1997).

FRACTURING

Differential metamictization of zircon causes volume expansion of the U-rich domains (Holland and Gottfried 1955) with consequent fracturing of the more resistant and brittle low-U domains (e.g., Chakoumakos et al. 1987; Figs. 13.1–13.4). Typically the fractures start at the interface with the more metamict domains or with high-U inclusions and develop radially outward across the low-U bands (Figs. 2-19–2.21; 5.1–5.4; 13.1 and 13.2). There is also a second type of fracture which develops concentrically along the boundary between high and low U domains (Figs. 13.2 and 13.3). Lee and Tromp (1995) discuss the parameters involved in the development of such fracture systems concluding that they are controlled principally by the degree of metamictization, the relative “shell” thickness and the confining (external) pressure. They also suggest that the latter factor may provide a tool to estimate the depth of residence of a rock. This may not be achievable, however, because the elevated temperatures of the lower crust increase the rates of self annealing to the point where zircon fractures are rarely developed. This is demonstrated by the generally very

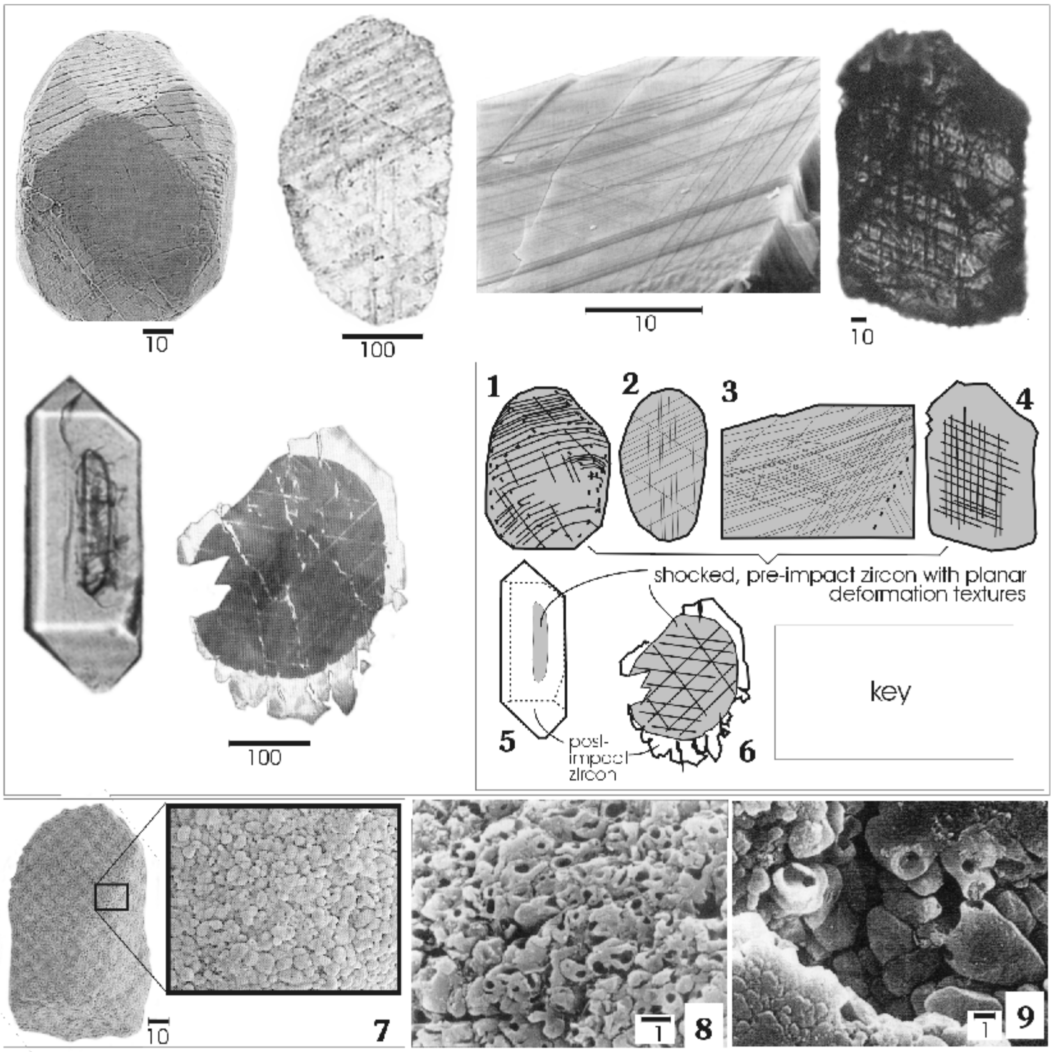

Figure 12. Appearance and texture of zircon in meteorite impact structures. **(1, 2)** Shocked zircon crystals from charnockite in Vredefort structure, modified from Kamo et al. (1996), 1 = SEM, 2 = TL, crossed nicols. **(3)** Euhedral zircon with three sets of planar deformation features; Manicouagan impact crater, modified from Bohor et al. (1993); SEM. **(4)** Multiple sets of planar deformation features in shocked zircon in Copper Cliff rhyolite, Sudbury structure, from F. Corfu (unpublished data), TL. **(5, 6)** Zircons from post-impact granite from Vredefort structure, modified from Gibson et al. (1997); 5 – euhedral crystal without shock-related features enclosing a fractured core (RL); 6 – zircon core with three sets of planar deformation features surrounded by post-impact unfractured zircon rim (CL). **(7)** granular zircon grain from granophyric part of melt-breccia dyke, Vredefort structure, modified from Kamo et al. (1996), SEM. **(8, 9)** polycrystalline grains with degassing and melting textures; 8 – K/T distal impact ejecta, Berwind Canyon, Colorado, modified from Bohor et al. (1993); SEM; 9 – Onaping Formation (impact melt), Sudbury structure, modified from Krogh et al. (1996), SEM.

good preservation of zircon in exhumed lower crustal rocks (e.g., Rudnick and Williams 1987, Hanchar and Rudnick 1995).

The parallel breaking shown by the zircon from a lower crustal xenolith in Figure 13.5 is a more rare occurrence. It has been interpreted to represent rapid decompression during eruption of the carrier volcanic rock (Rudnick and Williams 1987). It might be analogous to the deformation

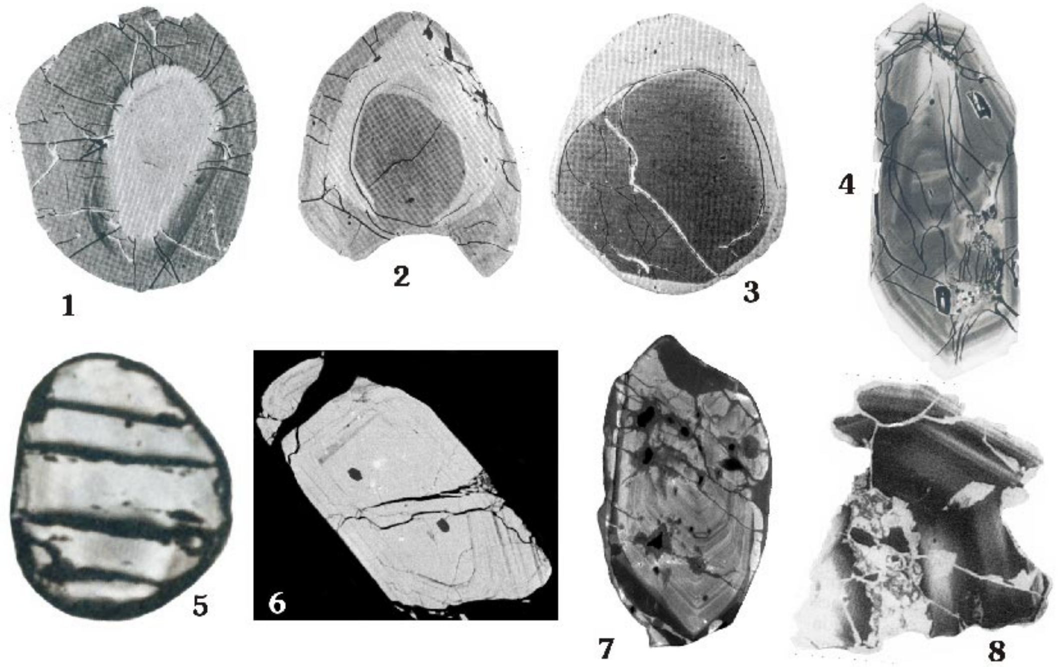

Figure 13. Fracture patterns in zircon. **(1-3)** Radial and concentric fractures in zircon from the Musgrave Ranges (modified from Lee and Tromp 1995; BSE); 1- radial fractures starting at the margin of the high-U+Th central part and propagating into the external, low-U+Th shell; 2 – expansion of the middle, U-Th-rich shell causes concentric fractures along the central part and radial fractures in the rim; 3 – metamictization of the high-Th+U rim causes concentric fracturing of the interface to the less metamict inner part. **(4)** Fractured zircon from Strontian pluton (modified from Paterson et al. 1992b, BSE); most of the cracks propagate from two spots that contain U+Th-rich inclusions but the fractures become concentric along the margin to the outermost high-U+Th rim. **(5)** Zircon from lower crustal xenolith (eastern Australia) showing pronounced parallel parting, apparently reflecting deformation during rapid decompression (modified from Rudnick and Williams 1987, TL). **(6)** Zoned zircon from a Witwatersrand conglomerate fractured during compaction between quartz and pyrite pebbles; the fractures are now healed with quartz; modified from Medenbach (1976), RL on polished section. **(7)** Ancient fractures, propagating from inclusions, were healed by the low-luminescence material grown metamorphically in external domains of zircon from upper crustal xenolith; modified from Schmitz and Bowring (2001), CL. **(8)** Fractures healed by luminescent material; modified from Rubatto et al. (1998), CL.

mechanism producing mosaic textures observed in some kimberlitic zircons (Fig. 11.7). Other factors that cause zircon fracturing are external stresses during mylonitization (Wayne and Sinha 1988) or diagenesis (Fig. 13.6; Medenbach 1976). When subjected to progressive diagenesis, or other metamorphic overprints, such fracture systems may heal and only be visible in specific circumstances (Fig. 13.7–13.8; also Figs. 3.5, 3.6 and 9.15).

ALTERATION

Chemical alteration is generally seen in zircon grains that are extensively metamictized and where pathways are available (e.g., grain boundary diffusion) for fluids to penetrate the structure. These pathways are most commonly the fracture systems discussed above, but occasionally also textural discontinuities (e.g., zoning, Fig. 14.5) and interfaces between zircon and inclusions of other minerals (Fig. 14.7). Alteration typically forms bulbous, botryoidal fronts, but locally also feathery textures (Fig. 14.2), that propagate along the cracks and within the crystal. The grain shown in Figure 14.1 consists of a low-U central part, surrounded by a high-U mantle, itself locally rimmed

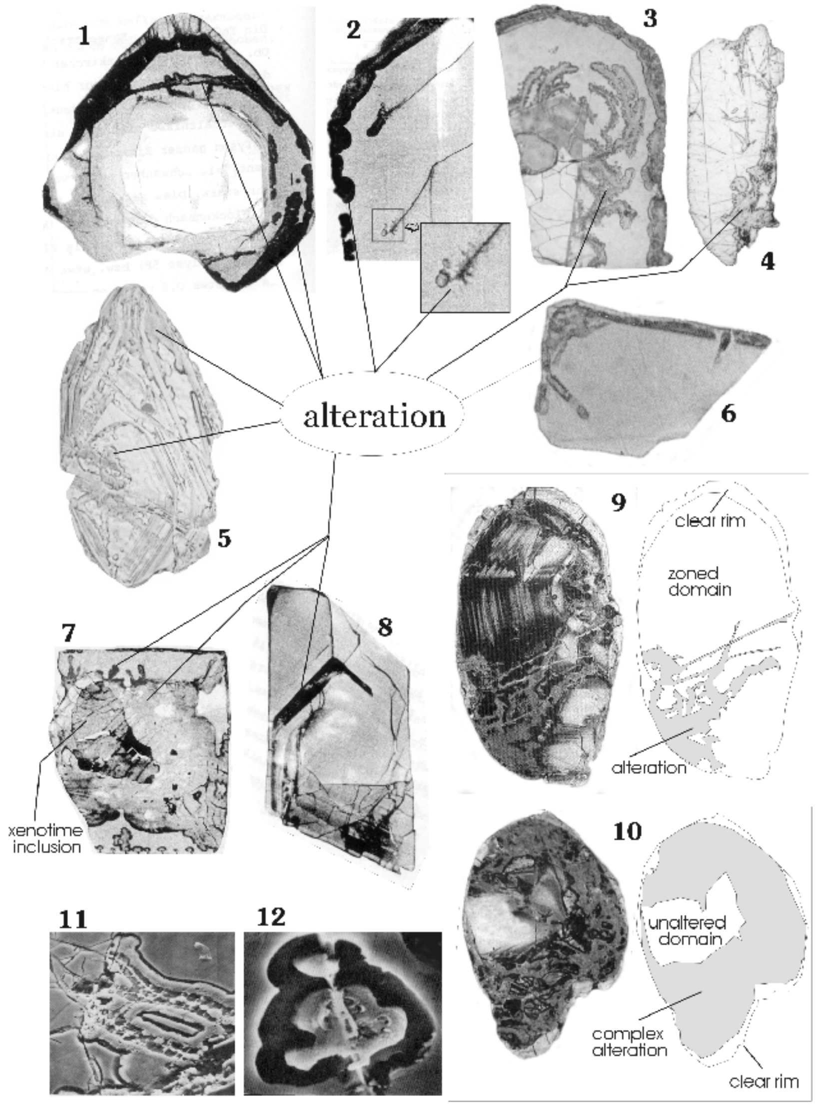

Figure 14. Patterns of alteration in zircon. **(1)** Alteration developed along concentric fractures parallel to the boundary between the low-U interior part of the zircon and the high-U outer shell; an outermost low-U rim has radial cracks, which have allowed the access of the fluids; modified from Medenbach (1976), RL. **(2)** Detail of a high-U zircon showing an outermost alteration ring and two internal alteration fronts with botryoidal and feathery propagation patterns; modified from Medenbach 1976), RL. **(3)** Zircon grain with low-U, fractured interior part surrounded by a high-U external band; alteration has developed both along an external rim and along curvilinear paths originating at the fractures in the euhedral, low-U inner zone; modified from Krogh and Davis (1974), RL. **(4)** Local alteration around fractures parallel and orthogonal to the c-axis; from F. Corfu (unpublished data), RL. **(5)** Zoned zircon with alteration controlled mainly by crystallographic discontinuities; modified from van Breemen et al. (1987), BSE. **(6)** High-U, homogeneous zircon with alteration restricted to its margin; modified from Krogh (1982), RL.**(7)** Zircon grain with a large inclusion of xenotime surrounded by an extensive zone of hydration propagating outwards, and with minor appendices moving inwards from the margin; modified from Medenbach (1976), RL. **(8)** Extensively altered, narrow high-U zones inside largely low-U zircon; modified from Medenbach (1976), RL. **(9,10)** Complexly zoned and altered zircon from the 4.0 Ga Acasta gneiss; modified from Bowring and Williams (1999), RL. **(11,12)** Brief exposure to HF vapor has dissolved the altered and hydrated part leaving behind ridges and plateaus of unaltered zircon; modified from Krogh and Davis (1975), SEM.

by a thin low-U zone. The latter is radially cracked allowing fluids to penetrate into the high-U material, which became altered—the alteration front propagating along concentric fractures. In Figure 14.3, a low-U central zone has become fractured allowing access (presumably from areas along the c-axis) to fluids, which then attack the surrounding metamict zone. The latter is also affected by alteration along an outer ring, the two alteration zones gradually approaching each other. Figures 14.4–14.6 and 14.7 illustrate other combinations of the same phenomenon, whereas Figure 14.8 displays the case of a predominantly low-U zircon with just a few high-U zones that have been reached by fluids along cracks in the low-U material and have become almost totally altered. The two grains in Figures 14.9 and 14.10 are ancient zircon crystals from the Acasta gneiss (Bowring and Williams 1999) that exhibit extremely complex alteration patterns penetrating zoned zircon domains and totally enclosing local islands of homogeneous unaltered zircon.

The alteration process has been shown to hydrate zircon, leaching some elements such as Pb and depositing others such as Fe and Ca (and possibly common Pb), hence making the mineral unsuitable for isotopic analysis (Krogh and Davis 1974, 1975; Medenbach 1976, Krogh 1982). The altered zones are much more soluble than crystalline zircon, and can be easily dissolved by brief exposures to dilute Hf vapor, providing a 3-dimensional image of the alteration process (Figs. 14.11 and 14.12).

INCLUSIONS, INTERGROWTHS AND OVERGROWTHS OF ZIRCON AND OTHER MINERALS

The relations between zircon and the minerals it includes, or which it is included in or overgrown, can provide important clues concerning crystallization conditions and paragenetic associations. This information can be critical when it comes to the interpretation of U-Pb zircon ages. Zircon crystals commonly carry inclusions of other minerals (Figs. 2.4, 2.7, 2.11, 13.4; 15.1–15.12; 15.18–5.19), especially of the main rock-forming minerals such as biotite, quartz and feldspar, but their relative abundance varies significantly between different populations. The study of mineral inclusions in metamorphic zircon helps to constrain the relative paragenesis of zircon with respect to the main rock-forming minerals. Zircons also often contain inclusions of melt that was present when the zircon crystallized (see Thomas et al., this volume, for a discussion of melt inclusions in zircon crystals). As an example, the zircon grains shown in Figures 15.1–15.3 include, or are included in, high pressure minerals such as diamond, garnet and coesite. Inclusions of melt and fluids (Figs. 15.5–15.9) can provide information on the composition of magma and gases at particular stages in the evolution of a magmatic or metamorphic system. Figure 15.9 illustrates the particular example of a kimberlitic zircon including both solid mineral inclusions as well as numerous fluid inclusions, which display very distinct crystallographically controlled arrangements.

Figures 15.10 and 15.11 show examples of zircon containing numerous inclusions of common minerals such as quartz and apatite, together with U and Th-rich components and many cavities. In general, the interpretation of such inclusions in highly metamict and altered grains is difficult because the inclusions could be either real xenocrysts or exsolved phases, or phases introduced after the formation of zircon. This is the case with the zircon grain shown in Figure 15.13 that contains secondary monazite crystallized along a crack in the crystal, or the zircon in Figure 15.12 that contains abundant galena introduced into the zircon long after its original crystallization. Figure 9.15 is an example of where omphacite was included in the zircon grain but it is surrounded by healed cracks, hence it was formed during the secondary eclogite event that affected the zircon (Gebauer et al. 1997). The crystallographically controlled baddeleyite inclusions in zircon (Fig. 15.14) presumably reflect the breakdown of zircon to baddeleyite and silica (cf. also McLaren et al. 1994).

The structural affinity (i.e., isostructural) of zircon and xenotime means that the two minerals are locally found in association with each other in the form of xenotime overgrown by zircon (Figs. 14.7; 15.17), or the other way around (Figs. 15.16 and 15.17), or as complex intergrowths (Figs. 15.18 and 15.19). The two xenotime crystals attached to zircon in Figure 15.15 were formed during diagenesis and can thus be used to constrain the age of sedimentation (e.g., Fletcher et al. 2000).

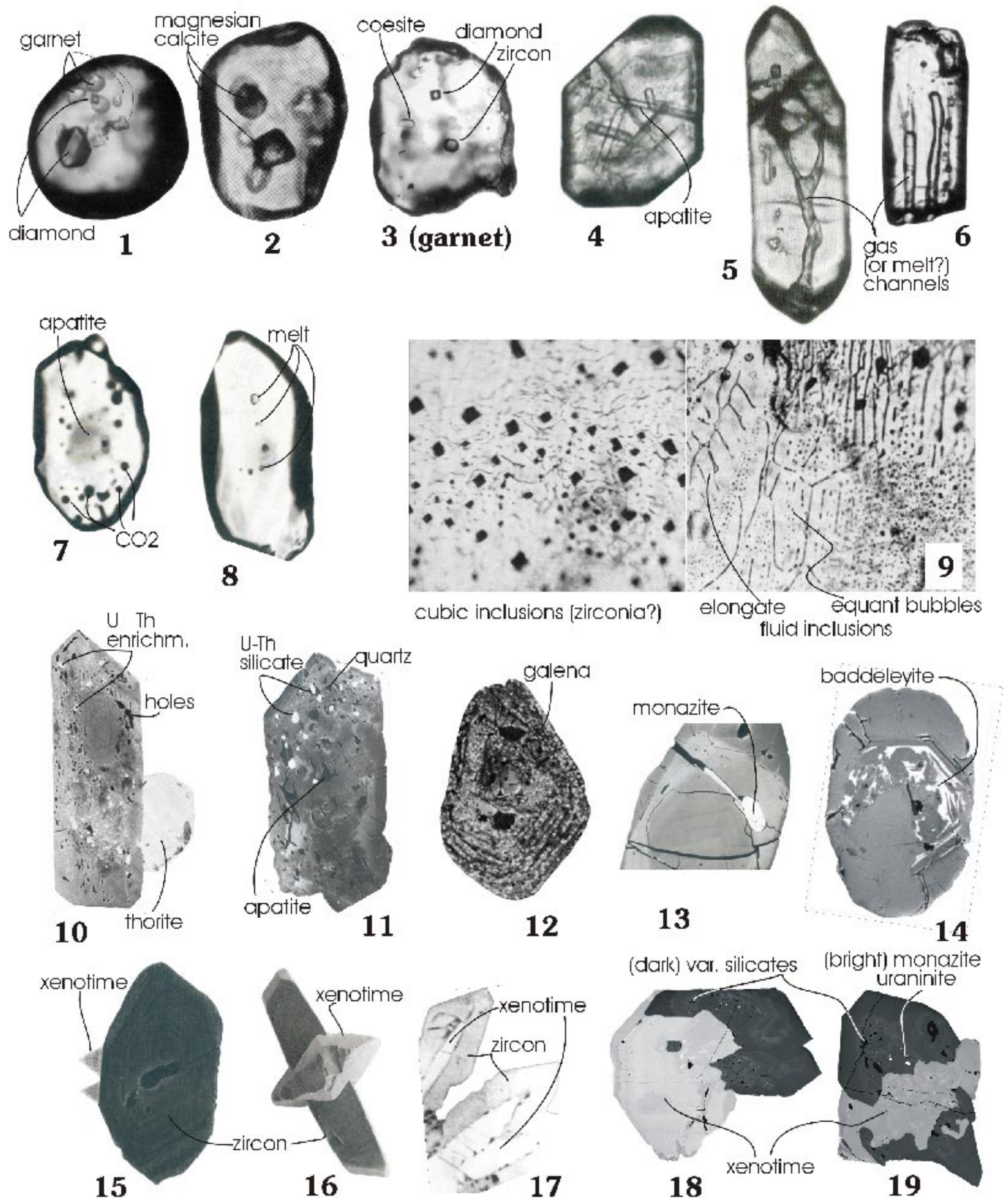

CONCLUDING REMARKS

The above presentation emphasizes the variety of internal and external features that characterise zircon, and shows how such features can be used to extract valuable information concerning the geological history and petrogenetic context of zircon. The diagnostic value of such studies is naturally much increased once the zircon features are considered in conjunction with elemental or isotopic constraints from the same mineral and in the context of well characterised rock units. It is also important to keep in mind that the interpretation of some features such as growth zoning or resorption phenomena can be somewhat ambiguous and controversial. Thus some caution is required when textural interpretations are carried out.

Figure 15. Inclusions, intergrowths, and overgrowths in zircon. All grains shown here are about 100 to 200 µm in size. **(1-3)** Zircon from an ultra-high pressure gneiss contains inclusions of garnet and diamond (1), and magnesian calcite (2) but is itself included in garnet together with diamonds and coesite (3); (modified from Korsakov et al. 2002, TL). **(4-5)** Zircon in granitic rock with needle like apatite inclusions (4) and an elongated, bifurcating cavity (with melt?) (5); (modified from Bussy and Cadoppi 1996, TL). **(6)** Tubular cavities in zircon from charnockite (modified from Chiarenzelli and McLelland 1993; TL). **(7-8)** Melt inclusions (8) and CO_2 plus an apatite inclusion (7) in zircon from a lower crustal xenolith (modified from Rudnick and Williams 1987, TL). **(9)** Inclusions in zircon of kimberlite. **Left:** cubic minerals (zirconia?; 10-20 µm wide); **right:** oriented trails of fluid inclusions (droplets or elongated channels, <10 µm wide)(modified from Kresten et al. 1975, TL). **(10)** Porous zircon from peralkaline granite with numerous U and Th rich inclusions and a lateral overgrowth of thorite (modified from Poitrasson et al. 1998, BSE). **(11)** Inclusions of quartz, apatite and a U-Th silicate phase in zircon from diorite (modified from Mulch et al. 2002, BSE). **(12)** zircon from a sedimentary rock in the Oklo fossil reactor; the crystal is sprinkled with galena inclusions (white spots) introduced during late hydrothermal events (modified from Mathieu et al. 2001, BSE). **(13)** Monazite growing in a fracture in zircon (modified from Barbey et al. 1989, BSE)**. (14)** Baddeleyite replacement inside zoned zircon from tonalitic gneiss (modified from Barth et al. 2002, BSE). **(15)** Detrital zircon with lateral outgrowths of two diagenetic xenotime crystals (modified from Fletcher et al. 2000, BSE). **(16)** Euhedral xenotime overgrowing zircon (modified from Schärer et al. 1994, SEM). **(17)** Zircon overgrowths on xenotime crystals in peralkaline magmatic complex (modified from Smith et al. 1991, BSE). **(18-19)** Intergrowth of zircon and xenotime in leucogranite sill. Convolutely zoned cores of both phases are rimmed by oscillatory zoned material and then by a broad homogeneous mantle (modified from Viskupic 2003, CL).

ACKNOWLEDGMENTS

Thanks to Sven Dahlgren, Desmond Moser, Urs Schaltegger, Mark Schmitz and Karen Viskupic for providing unpublished images and Mark Schmitz for his attentive review.

REFERENCES

Abati J, Dunning GR, Arenas R, Diaz Garcia F, Gonzalez Cuadra P, Martinez Catalan JR, Andonaegui P (1999) Early Ordovician orogenic event in Galicia (NW Spain): Evidence from U-Pb ages in the uppermost unit of the Ordenes Complex. Earth Planet Sci Lett 165:213-228

Andersson J, Williams IS (2001) Late-magmatic modification of zircon in the 1.38 Ga Tjärnesjö granite, eastern Sveconorwegian orogen, SW Sweden. *In* Andersson J (2001) Sveconorwegian orogenesis in the southwestern Baltic Shield—Zircon geochronology and tectonothermal setting of orthogneisses in SW Sweden. Doctoral thesis, Lund University, Sweden

Ashwal LD, Tucker RD, Zinner EK (1999) Slow cooling of deep crustal granulites and Pb-loss in zircon. Geochim Cosmochim Acta 63:2839-2851

Barbey P, Bertrand J-M, Angoua S, Dautel D (1989) Petrology and U/Pb geochronology of the Telohat migmatites, Aleksod, Central Hoggar, Algeria. Contrib Mineral Petrol 101:207-219

Barth MG, Rudnick RL, Carlson RW, Horn I, McDonough WF (2002) Re-Os and U-Pb geochronological constraints on the eclogite-tonalite connection in the Archean Man Shield, West Africa. Precambrian Res 118:267-283

Belousova EA, Griffin WL, Pearson NJ (1998) Trace element composition and cathodoluminescence properties of southern African kimberlitic zircons. Mineral Mag 62:355-366

Benisek A, Finger F (1993) Factors controlling the development of prism faces in granite zircons: A microprobe study. Contrib Mineral Petrol 114:441-451

Bingen B, Austrheim H, Whitehouse M (2001a) Ilmenite as a source for zirconium during high-grade metamorphism? Textural evidence from the Caledonides of western Norway and implications for zircon geochronology. J Petrol 42:355-375

Bingen B, Davis WJ, Austrheim H (2001b). Zircon U-Pb geochronology in the Bergen arc eclogites and their Proterozoic protoliths, and implications for the pre-Scandian evolution of the Caledonides in western Norway. Geol Soc Am Bull 113:640-649

Bohor BF, Betterton WJ, Krogh TE (1993) Impact-shocked zircons: discovery of shock-induced textures reflecting increasing degrees of shock metamorphism. Earth Planet Sci Lett 119:419-424

Bossart PJ, Meier M, Oberli F, Steiger RH (1986) Morphology versus U-Pb systematics in zircon: A high-resolution isotopic study of a zircon population from a Variscan dyke in the Central Alps. Earth Planet Sci Let 78:339-354

Bowring SA, Williams IS (1999) Priscoan (4.00-4.03 Ga) orthogneisses from northwestern Canada. Contrib Mineral Petrol 134:3-16

Bröcker M, Enders M (1999) U-Pb zircon geochronology of unusual eclogite-facies rocks from Syros and Tinos (Cyclades, Greece). Geol Mag 136:111-118

Bussy F, Cadoppi P (1996) U-Pb zircon dating of granitoids from the Dora-Maira massif (western Italian Alps). Swiss Bull Mineral Petrol 76:217-233

Chiarenzelli JR, McLelland JM (1993) Granulite facies metamorphism, palaeo-isotherms and disturbance of the U-Pb systematics of zircon in anorogenic plutonic rocks from the Adirondack Highlands. J Metamor Geol 11:59-70

Chakoumakos BC, Murakami T, Lumpkin GR, Ewing RC (1987) Alpha-decay-induced fracturing in zircon: the transition from the crystalline to the metamict state. Science 236:1556-1559

Charoy B, Raimbault L (1994) Zr, Th, and REE-rich biotite differentiates in the A-type granite pluton of Suzhou (Eastern China): the key role of fluorine. J Petrol 35:919-962

Chen YD, O'Reilly SY, Griffin WL, Krogh TE (1998) Combined U-Pb dating and Sm-Nd studies of lower crustal and mantle xenoliths from the Delegate basaltic pipes, southeastern Australia. Contrib Mineral Petrol 130:154-161

Cherniak DJ, Hanchar JM, Watson EB (1997a) Rare-earth diffusion in zircon. Chem Geol 134:289-301

Cherniak DJ, Hanchar JM, Watson EB (1997b) Diffusion of tetravalent cations in zircon. Contrib Mineral Petrol 127:383-390

Cherniak DJ, Watson EB (2001) Pb diffusion in zircon. Chem Geol 172:5-24

Christoffel CA, Connelly JN, Åhäll K-I (1999) Timing and characterization of recurrent pre-Sveconorwegian metamorphism and deformation in the Varberg-Halmstad region of SW Sweden. Precambrian Res 98:173-195

Connelly JN (2001) Degree of preservation of igneous zonation in zircon as a signpost for concordancy in U/Pb geochronology. Chem Geol 172:25-39

Corfu F, Ayres LD (1984) U-Pb ages and genetic significance of heterogeneous zircon populations in rocks from the Favourable Lake area, northwestern Ontario. Contrib Mineral Petrol 88:86-101

Corfu F, Stott GM (1998) The Shebandowan greenstone belt, western Superior Province: U-Pb ages, tectonic implications and correlations. Geol Soc Am Bull 110:1467-1484

Corfu F, Krogh Ravna E, Kullerud K (2002) A Late Ordovician U-Pb age for HP metamorphism of the Tromsdalstind eclogite in the Uppermost Allochthon of the Scandinavian Caledonides. 12th Annual Goldschmidt Conference, Geochim Cosmochim Acta 77:A153

Crookes W (1879) Contributions to molecular physics in high vacua. Phil Trans Roy Soc 170:641-642

Davidson A, van Breemen O (1988) Baddeleyite-zircon relationships in coronitic metagabbro, Grenville Province, Ontario: Implications for geochronology. Contrib Mineral Petrol 100:291-299

Duchesne JC, Caruba R, Iacconi P (1987) Zircon in charnockitic rocks from Rogaland (southwest Norway): Petrogenetic implications. Lithos 20:357-368

Fletcher IR, Rasmussen B, McNaughton NJ (2000) SHRIMP U-Pb geochronology of authigenic xenotime and its potential for dating sedimentary basins. Austral J Earth Sci 47:845-859

Fowler A, Prokoph A, Stern R, Dupuis C (2002) Organization of oscillatory zoning in zircon: Analysis, scaling, geochemistry, and model of a zircon from Kipawa, Quebec, Canada. Geochim Cosmochim Acta 66:311-328

Gebauer D, Schertl H-P, Brix M, Schreyer W (1997) 35 Ma old ultrahigh-pressure metamorphism and evidence for very rapid exhumation in the Dora Maira Massif, Western Alps. Lithos 41:5-24

Gibson RL, Armstrong RA, Reimold WU (1997) The age and thermal evolution of the Vredefort impact structure: A single-grain zircon study. Geochim Cosmochim Acta 61:1531-1540

Görz H, Bhalla RJRSB, White EW (1970) Detailed cathodoluminescence characterization of common silicates. Space Sci Applic Solid State Luminesc Phen, MRL Publ 70-101:62-70

Grieco G, Ferrario A, von Quadt, A, Koeppel V, Mathez EA (2001) The zircon-bearing chromitites of the phlogopite peridotite of Finero (Ivrea Zone, Southern Alps): Evidence and geochronology of a metasomatized mantle slab. J Petrol 42:89-101

Hacker BR, Ratschbacher L, Webb L, Ireland T, Walker D, Shuwen D (1998) U/Pb zircon ages constrain the architecture of ultrahigh-pressure Qinling-Dabie Orogen, China. Earth Planet Sci Lett 161:215-230

Halden NM, Hawthorne FC (1993) The fractal geometry of oscillatory zoning in crystals: Application to zircon. Am Mineral 78:1113-1116

Hanchar JM, Miller CF (1993) Zircon zonation patterns as revealed by cathodoluminescence and backscattered electron images: Implications for interpretation of complex crustal histories. Chem Geol 110:1-13

Hanchar JM, Rudnick RL (1995) Revealing hidden structures: the application of cathodoluminescence and backscattered electron imaging to dating zircons from lower crustal xenoliths. Lithos 36:289-303

Harrison TM, Watson EB (1983) Kinetics of zircon dissolution and zirconium diffusion in granitic melts of variable water content. Contrib Mineral Petrol 84:67-72

Heaman LM, LeCheminant AN (1993) Paragenesis and U-Pb systematics of baddeleyite (ZrO_2). Chem Geol 110:95-126

Hoffman JF, Long JVP (1984) Unusual sector zoning in Lewisian zircons. Mineral Mag 48:513-517

Holland HD and Gottfried D (1955) The effect of nuclear radiation on the structure of zircon. Acta Crystallogr 8:291-300

Hoskin PWO (1999) SIMS determination of μg g^{-1}-level fluorine in geological samples and its concentration in NIST SRM 610. Geostand Newslett: J Geostand Geoanal 23:69-76

Hoskin PWO (2000) Patterns of chaos: Fractal statistics and the oscillatory chemistry of zircon. Geochim Cosmochim Acta 64:1905-1923

Hoskin PWO, Black LP (2000) Metamorphic zircon formation by solid-state recrystallization of protolith igneous zircon. J Metamor Geol 18:423-439

Hoskin PWO, Kinny PD, Wyborn D (1998) Chemistry of hydrothermal zircon: Investigating timing and nature of water-rock interaction. *In* Water-rock Interaction. Arehart GB, Hulston JR (eds) Balkema, Rotterdam, The Netherlands, p 545-548

Huneke JC, Rossman GR (1978) Zircons of Summit Rock, Oregon. Mineral Record 392-393

Jocelyn J, Pidgeon RT (1974) Examples of twinning and parallel growth in zircons from some Precambrain granites and gneisses. Mineral Mag 39:587-594

Kamo SL, Reimold WU, Krogh TE, Colliston WP (1996) A 2.023 Ga age for the Vredefort impact event and a first report of shock metamorphosed zircons in pseudotachylitic breccias and Granophyre. Earth Planet Sci Lett 144:369-387

Kinny PD and Dawson JB (1992) A mantle metasomatic injection event linked to Late Cretaceous kimberlite magmatism. Nature 360:723-726

Köppel V, Sommerauer J (1974) Trace elements and the behaviour of the U-Pb system in inherited and newly formed zircons. Contrib Mineral Petrol 43:71-82

Korsakov AV, Shatsky VS, Sobolev NV, Zayachokovsky AA (2002) Garnet-biotite-clinozoisite gneiss: A new type of diamondiferous metamorphic rock from the Kokchetav Massif. Eur J Mineral 14:915-928

Koschek G (1993) Origin and significance of the SEM cathodoluminescence from zircon. J Micros 171:223-232

Kresten P, Fels P, Berggren G (1975) Kimberlitic zircons—a possible aid in prospecting for kimberlites. Mineral Dep 10:47-56

Krinsley DH, Manley CR (1989) Backscattered electron microscopy as an advanced technique in petrography. J Geol Educ 37:202-209

Krogh TE (1982) Improved accuracy of U-Pb zircon ages by the creation of more concordant systems using an air abrasion technique. Geochim Cosmochim Acta 46:637-649

Krogh TE, Davis GL (1974) Alteration in zircons with discordant U-Pb ages. Carnegie Inst Washington Yrbk 73:560-567

Krogh TE, Davis GL (1975) Alteration in zircons and differential dissolution of altered and metamict zircon. Carnegie Inst Washington Yrbk 74:619-623

Krogh TE, McNutt RH, Davis GL (1982) Two high precision U-Pb zircon ages for the Sudbury Nickel Irruptive. Can J Earth Sci 19:723-728

Krogh TE, Davis DW, Corfu F (1984) Precise U-Pb zircon and baddeleyite ages for the Sudbury area. Ontario Geol Surv Spec Vol 1:431-446

Krogh TE, Kamo SL, Bohor BF (1993) Fingerprinting the K/T impact site and determining the time of impact by U-Pb dating of single shocked zircons from distal ejecta. Earth Planet Sci Lett 119:425-429

Krogh TE, Kamo SL, Bohor B (1996) Shock metamorphosed zircons with correlated U-Pb discordance and melt rocks with concordant protolith ages indicate an impact origin for the Sudbury Structure. *In* Earth Processes: Reading the Isotopic Code. Basu A, Hart S (eds) Am Geophys Union, Geophys Monogr 95:343-353

Kröner A, Jaeckel P, Reischman T, Kroner U (1998) Further evidence for an early Carboniferous (~340 Ma) age of high-grade metamorphism in the Saxonian granulite complex. Geol Rundsch 86:751-766

Lee JKW, Tromp J (1995) Self-induced fracture generation in zircon. J Geophys Res 100:17753-17770

Liermann H-P, Isachsen C, Altenberger U, Oberhänsli R (2002) Behaviour of zircon during high-pressure, low-temperature metamorphism: Case study from the Internal Unit of the Sesia Zone (Western Italian Alps). Eur J Mineral 14:61-71

Long JVP, Agrell SO (1965) The cathodoluminescence of minerals in thin section. Mineral Mag 34:318-326

Lopez Sanchez-Vizcaino V, Rubatto D, Gomez-Pugnaire MT, Trommsdorff V, Münterer O. (2001) Middle Miocene high-pressure metamorphism and fast exhumation of the Nevado-Filabride Complex, SE Spain. Terra Nova 13:327-332

Machado N, Goulet N, Gariépy C (1989) U-Pb geochronology of reactivated Archean basement and of Hudsonian metamorphism in the northern Labrador Trough. Can J Earth Sci 26:1-15

Malcuit RJ, Heimlich RA (1972) Zircons from Precambrian Gneiss, southern Bighorn Mountains, Wyoming. Am Mineral 57:1190-1209

Mariano AN (1978) The application of cathodoluminescence for carbonatite exploration and characterization. Proc Intl Symp Carbonatites. Brasil Depart Nac Prod Mineral, Brasilia, 39-57

Mariano AN (1989) Cathodoluminescence emission spectra of rare earth element activators in minerals. Rev Mineral 21:339-348

Marshall DJ (1988) Cathodoluminescence of geological materials. Unwin Hyman, London

Mathieu R, Zetterström L, Cuney M, Gauthier-Lafaye F, Hidaka H (2001) Alteration of monazite and zircon and lead migration as geochemical tracers of fluid paleocirculations around the Oklo-Okélobondo and Bangombé natural nuclear reaction zones (Francesville basin, Gabon). Chem Geol 171:147-171

Mattinson JM, Graubard CM, Parkinson DL, McLelland WC (1996) U-Pb reverse discordance in zircons: the role of fine-scale oscillatory zoning and sub-microscopic transport of Pb. Am Geophys Union, Geophys Monogr 95:355-370

McLaren AC, FitzGerald JD, Williams IS (1994). The microstructure of zircon and its influence on the age determination from U-Pb isotopic ratios measured by ion microprobe. Geochim Cosmochim Acta 58:993-1005

McLelland J, Hamilton M, Selleck B, McLelland J, Walker D, Orrell S (2001) Zircon U-Pb geochronology of the Ottawan Orogeny, Adirondack Highlands, New York: Regional and tectonic implications. Precambrian Res 109:39-72

Medenbach O (1976) Geochemie der Elemente in Zirkon und ihre räumliche Verteilung—eine Untersuchung mit der Elektronenstrahlmikrosonde. Doctoral thesis, Ruprecht-Karl-Universität, Heidelberg, Germany

Miller CF, Hanchar JM, Wooden JL, Bennett VC, Harrison TM, Wark DA, Foster DA (1992) Source region of a granite batholith: Evidence from lower crustal xenoliths and inherited accessory minerals. Trans Roy Soc Edinburgh 83:49-62

Moser DE (1997) Dating the shock wave and thermal imprint of the giant Vredefort impact, South Africa. Geology 25:7-10

Moser DE, Heaman LM (1997) Proterozoic zircon growth in Archean lower crustal xenoliths, southern Superior craton—a consequence of Matachewan ocean opening. Contrib Mineral Petrol 128:164-175

Mulch A, Rosenau M, Dörr W, Handy MR (2002) The age and structure of dikes along the tectonic contact of the Ivrea-Verbano and Strona-Ceneri Zones (southern Alps, Northern Italy, Switzerland). Swiss Bull Mineral Petrol 82:55-76

Murakami T, Chakoumakos BC, Ewing RC, Lumpkin GR, Weber WJ (1991) Alpha-decay event damage in zircon. Am Mineral 76:1510-1532

Myers JS, Crowley JL (2000) Vestiges of life in the oldest Greenland rocks? A review of early Archean geology in the Godthåbsfjord region, and reappraisal of field evidence for >3850 Ma life on Akilia. Precambrian Res 103:101-124

Nemchin AA, Pidgeon RT (1997) Evolution of the Darling Range Batholith, Yilgarn Craton, Western Australia: A SHRIMP zircon study. J Petrol 38:625-649

Nutman AP, Friend CRL, Kinny PD, McGregor VR, (1993) Anatomy of an Early Archaean gneiss complex: 3900 to 3600 Ma crustal evolution in southern West Greenland. Geology 21:415-418

Nutman AP, McGregor VR, Shiraishi K, Friend CRL, Bennett VC, Kinny PD (2002) •3850 Ma BIF and mafic inclusions in the Early Archaean Itsaq Gneiss Complex around Akilia, southern West Greenland? The difficulties of precise dating of zircon-free protoliths in migmatites. Precambrian Res 117:185-224

Oberli F, Meier M, Biino GG (1994) Time constraints on the pre-Variscan magmatic/metamorphic evolution of the Gotthard and Tavetsch units derived from single zircon U-Pb results. Swiss Bull Mineral Petrol 74:483-488

Ohnenstetter D, Cesbron F, Remond G, Caruba R, Claude J-M (1991) Émissions de cathodoluminescence de deux populations de zircons naturels: téntative d'interpretation. C R Acad Sci Paris 313:641-647

Ono A (1976) Chemistry and zoning of zircon from some Japanese granitic rocks. J Japan Assoc Mineral Petrol Econ Geol 71:6-17

Owen MR (1987) Hafnium content of detrital zircons: A new tool for provenance study. J Sed Petrol 57:824-830

Owen MR, Carozzi AV (1986) Southern provenance of upper Jackfork Sandstone, southern Ouachita Mountains: Cathodoluminescence petrology. Geol Soc Am Bull 97:110-115

Palmer HC, Davis DW (1987) Paleomagnetism and U-Pb geochronology of volcanic rocks from Michipicoten Island, Lake Superior, Canada: Precise calibration of the Keweenawan polar wander track. Precambrian Res 37:157-171

Paquette JL, Monchoux P, Couturier M (1995) Geochemical and isotopic study of a norite-eclogite transition in the European Variscan belt: Implications for U-Pb zircon systematics in metabasic rocks. Geochim Cosmochim Acta 59:1611-1622

Paterson BA, Stephens WE (1992) Kinetically induced compositional zoning in titanite: Implications for accessory-phase/ melt partitioning of trace elements. Contrib Mineral Petrol 109:373-385

Paterson BE, Stephens WE, Herd DA (1989) Zoning in granitoid accessory minerals as revealed by backscattered electron imagery. Mineral Mag 53:55-62

Paterson BA, Rogers G, Stephens WE (1992a) Evidence for inherited Sm-Nd isotopes in granitoid zircons. Contrib Mineral Petrol 111:378-390

Paterson BA, Stephens WE, Rogers G, Williams IS, Hinton RW, Herd DA (1992b) The nature of zircon inheritance in two granite plutons. Trans Roy Soc Edinburgh: Earth Sci 83:459-471

Peucat JJ, Bernard-Griffiths J, Gil Ibarguchi JI, Dallmeyer RD, Menot RP, Cornichet J, Iglesias Ponce de Leɓn M (1990) Geochemical and geochronological cross-section of the deep Variscan crust: The Cabo Ortegal high-pressure nappe (northwestern Spain). Tectonophysics 177:263-292

Pidgeon RT (1992) Recrystallization of oscillatory zoned zircon: some geochronological and petrological implications. Contrib Mineral Petrol 110:463-472

Pidgeon RT, Nemchin AA, Hitchen GJ (1998) Internal structures of zircons from Archean granites from the Darling Range batholith: Implications for zircon stability and the interpretation of zircon U-Pb ages. Contrib Mineral Petrol 132:288-299

Pidgeon RT, Nemchin AA, Kinny PD (2000) Fir-tree and nebulously zoned zircons from granulite facies rocks: Evidence for zircon growth and interaction with metamorphic fluids. Goldschmidt 2000, J Conf Abstr 5:798

Pin C, Lancelot J (1982) U-Pb dating of an Early Paleozoic bimodal magmatism in the French Massif Central and its further metamorphic evolution. Contrib Mineral Petrol 79:1-12

Poitrasson F, Paquette J-L, Montel J-M, Pin C, Duthou J-L (1998) Importance of late-magmatic and hydrothermal fluids on the Sm-Nd isotope mineral systematics of hypersolvus granite. Chem Geol 146:187-203

Poldervaart A (1956) Zircon in rocks. 2. Igneous rocks. A, J Sci 254:521-554

Poller U (1997) U-Pb single zircon study of gabbroic and granitic rocks of Val Barlas-ch (Silvretta nappe, Switzerland). Swiss Bull Mineral Petrol 77:351-359

Pupin JP (1980) Zircon and granite petrology. Contrib Mineral Petrol 73:207-220

Remond G, Cesbron F, Chapoulie R, Ohnenstetter D, Roques-Carmes C, Schoverer M (1992) Cathodoluminescence applied to the microcharacterization of mineral materials: A present status in experimentation and interpretation. Scan Microsc 6:23-68

Rowley DB, Xue F, Tucker RD, Peng ZX, Baker J, Davis A (1997) Ages of ultrahigh pressure metamorphism and protolith orthogneisses from the eastern Dabie Shan: U/Pb zircon geochronology. Earth Planet Sci Lett 151:191-203

Rubatto D, Gebauer D (1999) Eo/Oligocene (35 Ma) high-pressure metamorphism in the Gornergrat Zone (Monte Rosa, Western Alps): Implications for paleogeography. Swiss Bull Mineral Petrol 79:353-362

Rubatto D, Gebauer D, Fanning M (1998) Jurassic formation and Eocene subduction of the Zermatt-Saas-Fee ophiolites: Implications for the geodynamic evolution of the Central and Western Alps. Contrib Mineral Petrol 132:269-287

Rubin JN, Henri CD, Price JG (1989) Hydrothermal zircons and zircon overgrowths, Sierra Blanca Peaks, Texas. Am Mineral 74:865-869

Rudnick RL, Williams IS (1987) Dating the lower crust by ion microprobe. Earth Planet Sci Lett 85:145-161

Schaltegger U, Gebauer D, von Quadt A (2002) The mafic-ultramafic rock association of Loderio-Biasca (lower Pennine nappes, Ticino, Switzerland): Cambrian oceanic magmatism and its bearing on early Paleozoic paleogeography. Chem Geol 186:265-279

Schaltegger U, Fanning CM, Gunther D, Maurin JC, Schulmann K, Gebauer D (1999) Growth, annealing and recrystallization of zircon and preservation of monazite in high-grade metamorphism: Conventional and *in situ* U-Pb isotope, cathodoluminescence and microchemical evidence. Contrib Mineral Petrol 134:186-201

Schärer U, Zhang L-S, Tapponnier P (1994) Duration of strike slip movement in large shear zones: The Red River belt, China. Earth Planet Sci Lett 126:379-397

Schärer U, Corfu F, Demaiffe D (1997) U-Pb and Lu-Hf isotopes in baddeleyite and zircon megacrysts from the Mbuji-Mayi kimberlite: Constraints on the subcontinental mantle. Chem Geol 143:1-16

Schmitz MD, Bowring SA (2001) The significance of U-Pb zircon dates in lower crustal xenoliths from the south-western margin of the Kaapvaal Craton, southern Africa. Chem Geol 172:59-76

Schmitz MD, Bowring SA (2002a) High precision U-Pb zircon geochronology of southern African cratonic mantle eclogites and implications for subcontinental lithospheric mantle evolution and metasomatism. EOS Trans, Am Geophys Union 83:S376

Schmitz, MD, Bowring SA (2002b) Ultrahigh-temperature metamorphism in the lower crust during Neoarchean Ventersdorp rifting and magmatism, Kaapvaal Craton, southern Africa. Geol Soc Am Bull (in press)

Scoates JS, Chamberlain KR (1995) Baddeleyite (ZrO_2) and zircon ($ZrSiO_4$) from anorthositic rocks of the Laramie anorthosite complex, Wyoming: Petrologic consequences and U-Pb ages. Am Mineral 80:1317-1327

Silver LT, Deutsch S (1963) Uranium-lead isotopic variations in zircons: A case study. J Geol 71:721-758

Sippel RF (1968) Sandstone petrology, evidence from luminescence petrography. J Sed Petrol 38:530-554

Sippel RF (1971) Luminescence petrography of the Apollo 12 rocks and comparative features in terrestrial rocks and meteorites. Proc Second Lunar Conf 1. MIT, Cambridge, Massachusetts, p 247-263

Smith DGW, de St. Jorre L, Reed SJB, Long JVP (1991). Zonally metamictized and other zircons from Thor Lake, Northwest Territories. Can Mineral 29:301-309

Smith JV, Stenstrom RC (1965) Electron-excited luminescence as a petrologic tool. J Geol 73:627-635

Sommerauer J (1974) Trace element distribution patterns and the mineralogical stability of zircon—an application for combined electron microprobe techniques. Electron Micros Soc S Afr Proc 4:71-72

Speer JA (1982) Zircon. Rev Mineral 5(2nd edn):67-112 van Breemen O, Davidson A, Loveridge WD, Sullivan RW (1986) U-Pb zircon geochronology of Grenville tectonites, granulite and igneous precursors, Parry Sound, Ontario. *In* The Grenville Province, Moore JM, Davidson A, Baer AJ (eds) Geol Assoc Can Spec Paper 3, p 191-207

van Breemen O, Henderson JB, Loveridge WD, Thompson PH (1987) U-Pb zircon and monazite geochronology and zircon morphology of granulites and granite from the Thelon Tectonic Zone, Healey Lake and Artillery Lake map areas, N.W.T. Geol Surv Can Paper 87-1A:783-801

Vavra G (1990) On the kinematics of zircon growth and its petrogenetic significance: A cathodoluminescence study. Contrib Mineral Petrol 106:90-99

Vavra G (1993) A guide to quantitative morphology of accessory zircon. Chem Geol 110:15-28

Vavra G, Hansen BT (1991) Cathodoluminescence studies and U-Pb dating of zircons in pre-Mesozoic gneisses of the Tauern Window: Implications for the Pennine basement evolution. Geol Rundsch 80:703-715

Vavra G, Gebauer D, Schmid R, Compston W (1996) Multiple zircon growth and recrystallization during polyphase Late Carboniferous to Triassic metamorphism in granulites of the Ivrea zone (Southern Alps): An ion microprobe (SHRIMP) study. Contrib Mineral Petrol 122:337-358

Viskupic K (2003) Crustal melting in the Himalayan orogen: field, geochemical and geochronological studies in the Everest region, Nepal. PhD thesis, Massachusetts Institute of Technology, 190 p

Vocke RD Jr, Hanson GN (1981) U-Pb zircon ages and petrogenetic implications for two basement units from Victoria valley, Antarctica. *In* Antarctica Research Series, Dry Valley Drilling Project. McGinnis L (ed) Am Geophys Union, Washington, DC, 33:247-255

Watson EB (1979) Zircon saturation in felsic liquids: Experimental results and applications to trace element geochemistry. Contrib Mineral Petrol 70:407-419

Watson EB (1996) Dissolution, growth and survival of zircons during crustal fusion: kinetic principles, geological models and implications for isotopic inheritance. Trans Roy Soc Edinburgh: Earth Sci 87:43-56

Watson EB, Harrison TM (1983) Zircon saturation revisited: temperature and composition effects in a variety of crustal magma types. Earth Planet Sci Lett 64:295-304

Watson EB, Liang Y (1995) A simple model for sector zoning in slowly grown crystals: Implications for growth rate and lattice diffusion, with emphasis on accessory minerals in crustal rocks. Am Mineral 80:1179-1187

Watson EB, Vicenzi EP, Rapp RP (1989) Inclusion/host relations involving accessory minerals in high-grade metamorphic and anatectic rocks. Contrib Mineral Petrol 101:220-231

Watson EB, Cherniak DJ, Hanchar JM, Harrison, TM, Wark DA (1997) The incorporation of Pb into zircon. Chem Geol 141:19-31

Wayne DM, Sinha AK (1988) Physical and chemical response of zircons to deformation. Contrib Mineral Petrol 98:109-121

Wayne DM, Sinha AK (1992) Stability of zircon U-Pb systematics in a greenschist-grade mylonite: an example from the Rockfish Valley fault zone, central Virginia, USA. J Geol 100:593-603

Welin E, Gorbatschev R, Kähr A-M (1982) Zircon dating of polymetamorphic rocks in southwestern Sweden. Sver Geol Unders C797:1-34

Whitehouse MJ, Kamber BS, Moorbath S (1999) Age significance of U-Th-Pb zircon data from early Archaean rocks of West Greenland-a reassessment based on combined ion-microprobe and imaging studies. Chem Geol 160:201-224

Yang B, Luff, BJ, Townsend, PD (1992) Cathodoluminescence of natural zircons. J Phys: Condens Matter 4:5617-5624

Zeck HP, Williams IS (2002) Inherited and magmatic zircon from Neogene Hoyazo cordierite dacite, SE Spain—anatectic source rock provenance and magmatic evolution. J Petrol 43:1089-1104

PS Strategies for Identifying Organic Matter Types in SEM*

Wayne K. Camp[1]

Search and Discovery Article #70233 (2017)**
Posted February 6, 2017

*Adapted from poster presentation given at SEPM-AAPG 2016 Hedberg Research Conference, Santa Fe, New Mexico, October 16-19, 2016

[1] Anadarko Petroleum Corporation, The Woodlands, Texas, U.S.A. (wayne.camp@anadarko.com)

Abstract

Solid organic matter is easily identified in scanning electron microscope (SEM) images acquired from flat, smoothly polished surfaces (e.g., Ar-ion milled) by its characteristic low secondary electron yield and low backscatter intensity; appearing dark gray in standard grayscale images. However, SEM is poorly suited for interpreting specific organic maceral and kerogen types as described by optical petrographic or geochemical methods.

Lack of consistent and standardized descriptions of organic matter in SEM has led to confusion and controversy in the characterization of organic composition, interpretations of the origins of pores in organic matter, and organic diagenesis.

This paper describes a practical method for the description and classification of organic matter in SEM and various strategies used to help bridge the gap between optical and electron microscopic characterization of organic matter in carbonaceous mudstones.

Reference Cited

Canter, L., S. Zhang, M. Sonnenfeld, C. Bugge, M. Guisinger, and K. Jones, 2016, Primary and Secondary Organic Matter Habit in Unconventional Reservoirs, *in* T. Olson (ed.), Imaging Unconventional Reservoir Pore Systems: American Association of Petroleum Geologists Memoir 112, p. 9-24.

Strategies For Identifying Organic Matter Types in SEM

Wayne K. Camp

Introduction

Solid organic matter is easily identified in scanning electron microscope (SEM) images acquired from flat, smoothly polished surfaces (e.g., Ar-ion milled) by its characteristic low secondary electron yield and low backscatter intensity; appearing dark gray in standard grayscale images. However, SEM is poorly suited for interpreting specific organic maceral and kerogen types as described by optical petrographic or geochemical methods.

Lack of consistent and standardized descriptions of organic matter in SEM has led to confusion and controversy in the characterization of organic composition, interpretations of the origins of pores in organic matter, and organic diagenesis.

This paper describes a practical method for the description and classification of organic matter in SEM and various strategies used to help bridge the gap between optical and electron microscopic characterization of organic matter in carbonaceous mudstones.

SEM Organic Matter Classification

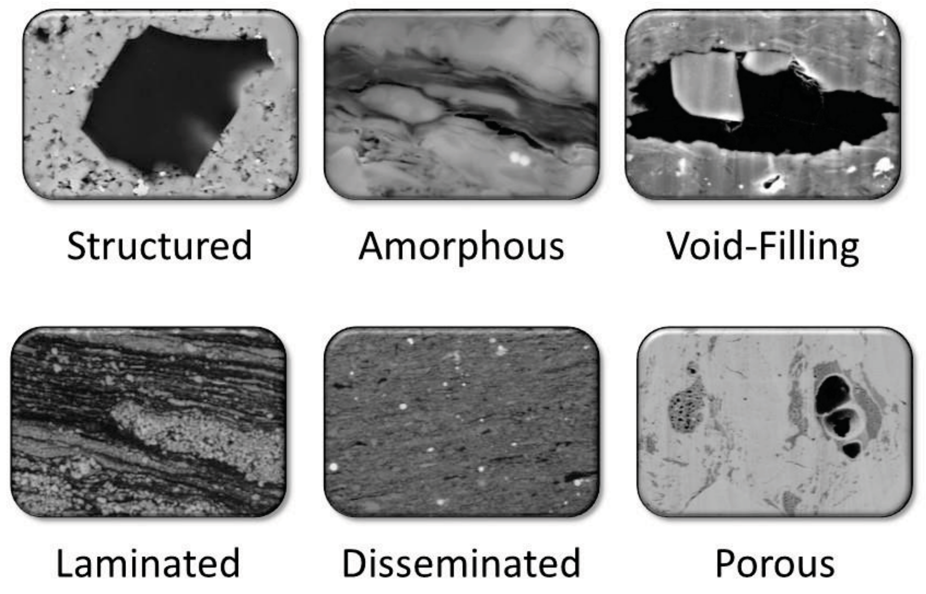

SEM Organic Matter Classification

In the absence of other supporting criteria, it is recommended using common petrographic terms when describing organic matter in SEM images. Terms such as kerogen, vitrinite, type III kerogen, algal mat, bitumen, pyrobitumen, etc. should not be used for organic matter descriptions. These terms are interpretations of the type of organic matter, and should be clearly stated as interpretations, including the supporting evidence.

Organic matter can be classified based on petrographic evidence into three main types: 1) structured, 2) amorphous, and 3) void-filling. The term void-filling should be restricted to where there is clear evidence of a prior void, such as fossil cavities, micro-fractures, and mineral-cement lined pores. Additional descriptive terms such as layered, interlaminated, disseminated, porous, non-porous, etc. can be appended as modifiers.

Direct Optical-SEM Comparison

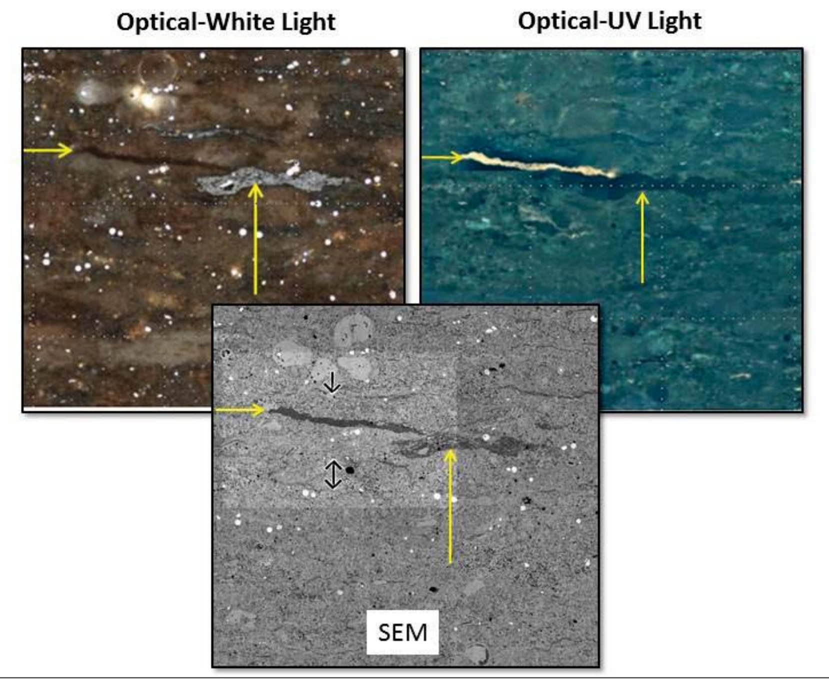

Direct Optical-SEM Comparison

Organic macerals are the microscopically identifiable remains of fossil organic matter. Standardized optical petrographic methodology and nomenclature have been developed initially for coal petrology and later applied to studies of dispersed organic matter in sedimentary rocks. The International Committee for Coal and Organic Petrology (ICCP, 1994) has defined a classification scheme that recognizes four main groups of organic macerals based on optical characteristics observed from polished samples immersed in oil in reflected white and ultraviolet light: 1) liptinite, 2) inertinite, 3) huminite and 4) vitrinite, with over 30 subgroups, macerals and varieties.

The most reliable method for identifying organic maceral types in SEM is by acquiring SEM images of the polished samples used to identify organic macerals in reflected light. Because the optical petrographic specimens are coated in oil, it may be preferable to either remove the oil, or sputter coat the samples with a conductive metal (e.g., iridium, palladium, etc.) to reduce the effect of electron charging. Note that attempting to remove the oil by solvents may alter or remove soluble forms of organic matter (bitumen). Wiping the surface with cloth or paper may contaminate the surface with organic fibers.

Because of the relatively low magnification limits of optical microscopy, this technique is limited to the identification of the larger organic matter particle population observed in SEM.

Comparative Anatomy

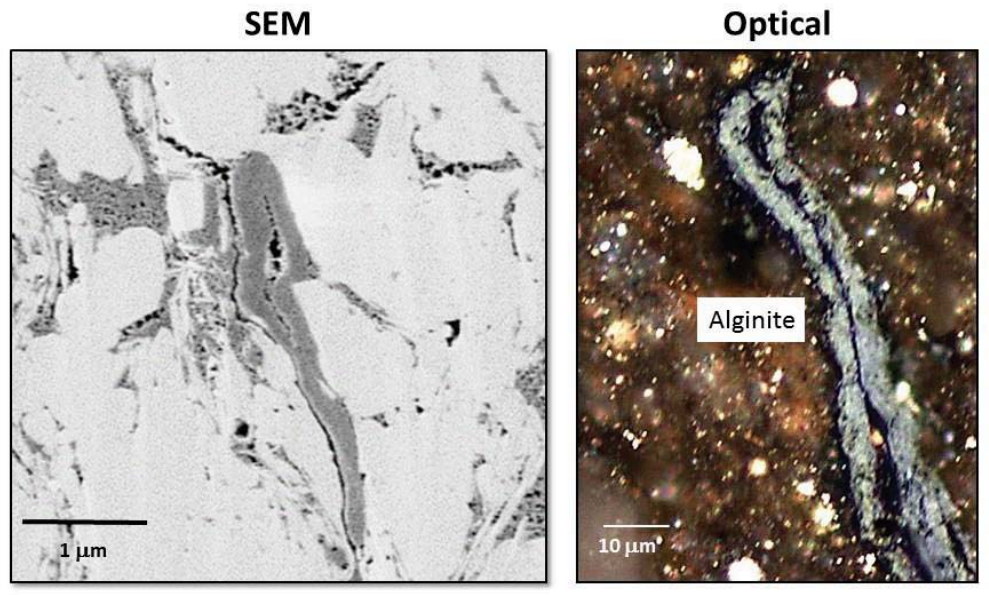

Comparative Anatomy

It may be possible to identify certain organic macerals and zooclasts in SEM based on characteristic morphology (comparative anatomy), e.g., *Tasmanities* algal cysts. Best results are produced by comparing identified organic macerals from splits of the same sample in photomicrographs reduced to match the scale of the SEM image.

Images of identified organic macerals are available online that provide a useful resource for comparative anatomy studies, e.g. the U.S. Geological Survey Atlas (http://energy.usgs.gov/Coal/OrganicPetrology/PhotomicrographAtlas.aspx), and the Indiana Geological Survey Atlas (https://igs.indiana.edu/Coal/Macerals.cfm).

Color photomicrographs may be converted to inverse grayscale images with digital image software so that bright, highly reflective organic matter in the optical image is converted to dark gray, to appear more similar to the dark gray tone of organic matter in SEM grayscale images.

Many organic maceral types are classified based on differences in the measured amount of reflected light (a measure of thermal maturity) - a property impossible to measure in SEM. For example, macerals exhibiting preserved botanical cell structures are classified in order of increasing thermal maturity as telohuminite, telovitrinite, semifusinite, or fusinite. Although it may be possible to recognize organic matter with preserved cell structures, it would be impossible to differentiate the maceral type in SEM. A more generic terminology based on physical appearance would be more useful for classifying organic macerals in SEM.

Toluene Immersion Test for Bitumen

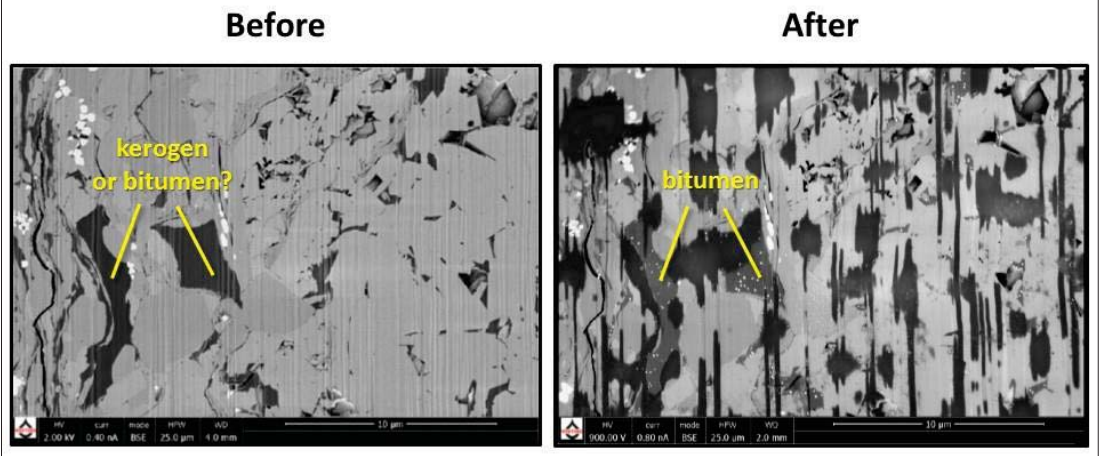

BSE, Ar-ion Milled Surface

BSE, Ar-ion Milled Surface

Canter et al., 2016: AAPG Memoir 112

Bitumen Solubility Test

Standard geochemical tests for bitumen involve immersing crushed samples in organic solvents, such as toluene, to remove soluble solid bitumen and residual liquid petroleum. The remaining proportion of insoluble organic matter is classified as kerogen.

Comparing SEM images before and after applying organic solvents to broken or polished surfaces may provide a positive test for bitumen. However, these types of test often fail to completely remove all of the bitumen or void-filling organic matter observable in SEM images that may result in ambiguous interpretations.

Geochemical and petrographic evidence for distinguishing kerogen from bitumen are often in conflict. Soluble-resistant forms of post-oil solid bitumen are known to result from advanced thermal alteration and are referred to as pyrobitumen (*sensu stricto*, kerogen!). During the thermal conversion of kerogen to oil, kerogen is first transformed to a soluble bitumen, known as pre-oil bitumen. Interpreting particulate, structured organic matter as kerogen in thermally mature samples is therefore problematic because some of this material is likely composed of pre-oil bitumen.

Acknowledgements

I thank Lyn Canter, Whiting Petroleum (Denver, Colorado) for permission to show her SEM images of the toluene test for bitumen. These results have recently been published as Canter, L., S. Zhang, M. Sonnenfeld, C. Bugge, M. Guisinger, and K. Jones, 2016, Primary and secondary organic matter habit in unconventional reservoirs, *in*, T. Olson, ed., Imaging Unconventional Reservoir Pore Systems: AAPG Memoir 112, p.9-24.

Contact Information

Wayne K. Camp
Distinguished Geological Advisor

Anadarko Petroleum Corporation
9950 Woodloch Forest Drive
The Woodlands, Texas 77380
Office: 832-636-3245